

Nonlinear dynamics of semiconductors in strong THz electric fields

Tarekegne, Abebe Tilahun; Jepsen, Peter Uhd; Iwaszczuk, Krzysztof

Publication date:
2017

Document Version
Publisher's PDF, also known as Version of record

[Link back to DTU Orbit](#)

Citation (APA):
Tarekegne, A. T., Jepsen, P. U., & Iwaszczuk, K. (2017). Nonlinear dynamics of semiconductors in strong THz electric fields. DTU Fotonik.

DTU Library

Technical Information Center of Denmark

General rights

Copyright and moral rights for the publications made accessible in the public portal are retained by the authors and/or other copyright owners and it is a condition of accessing publications that users recognise and abide by the legal requirements associated with these rights.

- Users may download and print one copy of any publication from the public portal for the purpose of private study or research.
- You may not further distribute the material or use it for any profit-making activity or commercial gain
- You may freely distribute the URL identifying the publication in the public portal

If you believe that this document breaches copyright please contact us providing details, and we will remove access to the work immediately and investigate your claim.

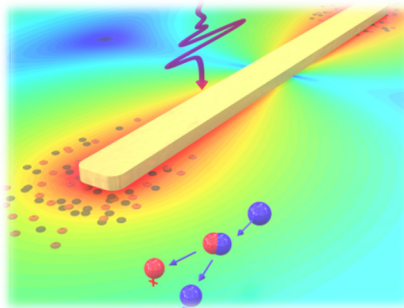
Technical University of Denmark



Nonlinear dynamics of semiconductors in strong THz electric fields

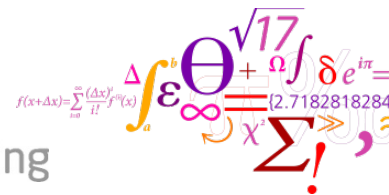
by

Abebe Tilahun Tarekegne



*A dissertation submitted in partial fulfillment of the requirements for
the degree of Doctor of Philosophy*

May 2017



Abstract

In this thesis, we investigate nonlinear interactions of an intense terahertz (THz) field with semiconductors, in particular the technologically relevant materials silicon and silicon carbide. We reveal the time-resolved dynamics of the nonlinear processes by pump-probe experiments that involve weak THz and near infrared pulses as probes.

Firstly, an intense THz pulse is used to study THz-induced impact ionization (IMI) dynamics in silicon. Local field enhancement by metallic dipole antenna arrays has been used to generate strong electric fields of several MV/cm in the hot spots near the antenna tips. For the first time, this enables investigation of field-induced IMI in silicon under very strong fields and at very low initial carrier concentrations. These regimes have previously been inaccessible in conventional transport measurements, due to avalanche breakdown. Using field enhancement technique we investigated the time-resolved dynamics of the IMI process by optical/THz pump-optical probe experiments. Our experimental results, in combination with Monte Carlo simulations, clarify that carrier multiplication dynamics depends strongly on the initial densities of carriers. In the limit of low initial carrier density ($1.5 \times 10^{10} \text{ cm}^{-3}$), a single electron is multiplied in a cascade of IMI events to generate more than 10^8 electrons within a few hundred femtoseconds. At high initial densities of carriers, the impact ionization rate reduces to values known from the literature due to Auger recombination, field screening and electron-hole scattering effects.

Silicon carbide (SiC) stands out as a promising alternative material platform for high power THz applications due to its high radiation resistance. Linear spectroscopy with broadband THz light reveals very sharp and strong resonant absorption lines due to folded zone lattice vibrations. These folded zone acoustic phonon modes can be seen as Si-C atomic planes

moving with respect to each other within the unit cell in a pattern characteristic to each polytype of SiC. Their specificity to the polytype is an ideal tag to identify polytypes uniquely.

Finally it is demonstrated for the first time that SiC can be tailored to have extremely fast THz-induced nonlinear behavior in moderate THz electric fields by addition of appropriate dopants. A *4H*-SiC sample with high concentrations of nitrogen and boron dopants shows a nonlinear THz transmission attributed to THz-induced dopant state ionization and scattering of hot electrons to a lower-mass conduction band. THz pump-THz probe experiments show that the nonlinear process has an ultrafast sub-picosecond recovery time. This demonstrates that the nonlinear response of doped SiC is among the fastest nonlinear modulation schemes for THz signals that can be applicable over wide ranges of operating temperatures.

Resumé

I denne afhandling studerer vi ikke-lineære vekselvirkninger mellem et intenst terahertz (THz) felt og de teknologisk vigtige halvledere silicium og silicium carbid. Undersøgelserne afslører den tidsopløste dynamik af ikke-lineære processer ved hjælp af pumpe-probe-eksperimenter, som involverer en kraftig THz-puls som pumpe og svage THz- og nærinfrarøde pulser som prober.

Først anvender vi en intens THz puls til at studere dynamikken i THz-induceret *impact ionization* (IMI) i silicium. Ved hjælp af metalliske dipolantenner opnår vi yderligere feltforstærkning, således at der genereres et elektrisk felt på adskillige MV/cm omkring dipolantennernes ender. Dette muliggør undersøgelse af felt-induceret IMI i silicium i et nyt feltregime og ved meget lave ladningsbærerkoncentrationer, som hidtil ikke har været tilgængelige i konventionelle jævnstrøms-transport-målinger grundet *avalanche breakdown*. Vi har med denne feltforstærkningsteknik undersøgt den tidsopløste dynamik af IMI-processer med optisk/THz pumpe – optisk probe eksperimenter, hvor udviklingen af den frie ladningsbærertæthed bliver overvåget med en forsinkelse af probepulsen. Vores eksperimenter, sammen med Monto Carlo simuleringer, viser at multiplikationsdynamikkerne for ladningsbærerne er stærkt afhængige af den initiale ladningsbærertæthed. Vi viser, at ved ekstremt lave initial ladningsbærertætheder ($1.5 \times 10^{10} \text{ cm}^{-3}$), bliver en enkelt elektron multipliceret i en kaskade af IMI-begivenheder og ender med at generere mere end 10^8 elektroner indenfor nogle få hundrede femtosekunder. Ved høj initial ladningsbærertæthed reduceres IMI raten til værdier kendt fra litteraturen, grundet Auger rekombination, afskærmning af det elektriske felt og spredningseffekter mellem elektroner og huller.

Silicium carbid (SiC) er en lovende, alternativ materialeplatform til højfelt-THz-anvendelser grundet meget høj bestrålingsmodstand. Lineær spektroskopi med en bredbåndet THz kilde viser meget skarpe og stærke, resonante absorptionslinjer grundet vibrationer af den foldede Brillouin-zone i materialets polytyper. Foton-vibrationsmønstrene i den foldede zone resulterer i at Si-C atomplanerne bevæger sig indbyrdes i enhedscellen i et mønster som er karakteristisk for hver polytype af SiC. Denne afhængighed er velegnet til entydigt at identificere polytyper.

Slutteligt bliver det for første gang demonstreret at SiC kan tilpasses til at have en ekstremt hurtig THz-induceret, ikke-lineær opførsel i et moderat THz elektrisk felt ved at tilsætte passende doteringsatomer. En 4H-SiC prøve, som indeholder høje koncentrationer af dotanterne nitrogen og bor, viser en ikke-lineær THz transmission der tilskrives en kombination af THz-induceret ionisering af dotantatomer og spredning af energetiske elektroner til et ledningsbånd med lavere effektiv masse. THz-pumpe-THz-probe eksperimenter viser at den ikke-lineære respons har ultrahurtig sub-picosekunds genoprettelsestid. Dette demonstrerer at den ikke-lineære respons af doteret SiC er blandt de hurtigste, ikke-lineære modulationsskemaer for THz signaler, som samtidig kan anvendes over et meget bredt temperaturområde.

Preface

The work presented in this thesis has been conducted during my PhD study at the Technical University of Denmark (DTU) from March 2014 to May 2017 under the supervision of Prof. Peter Uhd Jepsen and co-supervision of Assistant Prof. Krzysztof Iwaszczuk.

Most of the results presented in this thesis are obtained at DTU Fotonik – Department of Photonics Engineering. Of the three years period of the PhD study I spend the 3.5 months at Institute for Integrated Cell-Material Science (iCeMS) at Kyoto University, Kyoto, Japan. The experimental results presented in the section 4.2 of the thesis are performed in the lab of Associate Prof. Hirori.

This PhD project was financed by DTU Fotonik, Technical University of Denmark. I get a financial support from Scandinavia-Japan Sasakawa Foundation for my external research stay at Kyoto University. Otto Mønsted partially supported my travel expenses connected to international conferences. SPIE – the international society of optics and photonics financed my expenses of the SPIE Photonics west conference.



Kgs. Lyngby, May 19th 2017

Acknowledgments

It was a pleasure to know and interact with many people during my PhD adventure whom I am indebted to. First and foremost, I wish to extend my deep gratitude and utmost respect to my supervisor, Prof. Peter Uhd Jepsen, for giving me the opportunity to conduct research on such an interesting topic, for his wonderful ideas and for creating a nice and friendly working environment. It was an honor to be part of his team and it was a privilege to learn from his extraordinary experience in the THz field. I thank him for sharing his great expertise, the guidance and support which benefitted me greatly both scientifically and personally.

I am extremely grateful to my co-supervisor, Assistant Prof. Krzysztof Iwaszczuk, for his continuous support and guidance. I am privileged to learn from his excellent competences in the field. He has been there all the time in my learning of setup building, measurement techniques and data interpretations as well as theoretical modeling. I thank him very much for all the great ideas and mentoring.

I was a fortunate to collaborate with the THz group at Kyoto University and I would like to thank Prof. Tanaka for allowing and facilitating my visit of his lab during my external PhD stay. My time at Kyoto University was great and that is attributed mainly to Associate Prof. Hideki Hirori. I would like to thank him deeply for his wonderful scientific and social support. His engagement and long discussions played a big role in my scientific development and taught me the importance of perseverance and discipline. I would like to thank everyone who supported me in Japan but I have to mention the wonderful company of Kento Uchida for being there for me all the time even when we were not at work.

I will like to extend my gratitude to Weifang Lu and Associate prof. Haiyan Ou for the collaboration in the silicon carbide work and for

providing samples. I appreciate the fruitful discussions and engagement. I would like to bestow a special gratitude to Korbinian Julius Kaltenecker who also provided silicon carbide samples and ideas. I thank him the wonderful discussions and suggestions. I value the corrections you made to my thesis highly.

I am indebted to the entire group members of the THz group who are always there to extend their hand all the time. I wish express my special acknowledgement to Simon Lange who joined the group quite recently but we had fruitful discussions in the lab and in the office. Thank you for the corrections to my thesis. Similarly, I wish to thank Daena Madhi for the nice discussions and helping me in the correction of my thesis. I wish to extend my gratitude to Binbin Zhou for solving small or big problems of the laser amplifier and the help on the broadband THz setup. I also like to thank Thea Bjørk for helping me in the building of the pump-probe THz setup.

I would like to thank previous members of the THz crew DTU Fotonik for nice discussions in the lab and outside. I thank Pernille Klarskov Pedersen, Tianwu Wang, Andrew Strikwerda, and Corinna Ludovica Koch Dandolo. Andrew Strikwerda advised me on setup building techniques and CST simulations in the beginning of my PhD.

Last but most important, I wish to thank my wife and dear friend, Meaza Gebrehiwot Weldu, for handling the difficulty of being a mother while giving me full freedom to be in the lab and at work. I value her unswerving patience, strength, support and encouragement very much. I also thank my little boy, Barok, for the charm that busts my stress after a tough day in the lab.

Table of Contents

Abstract	II
Resumé	IV
Preface	VI
Acknowledgments	VII
Chapter 1 Introduction.....	1
Chapter 2 Intense terahertz generation and detection.....	9
2.1 Introduction	9
2.2 THz generation with optical rectification.....	11
2.3 THz detection with electro-optic sampling	12
2.4 THz field enhancement with antenna arrays	16
2.5 THz time-domain spectroscopy setup	19
2.6 THz pump-THz probe experimental setup	22
Chapter 3 THz-induced impact ionization in high resistivity silicon	29
3.1 Introduction	29
3.2 Results and discussion.....	32
3.3 Comparison of front and back THz illuminations.....	38
3.4 Temperature-dependent measurements	42
3.5 Conclusion.....	44
Chapter 4 Time-resolved investigation of impact ionization dynamics in silicon	47
4.1 Introduction	47
4.2 THz/optical pump-optical probe measurements.....	49
4.2.1 Experimental setup	49
4.2.2 Measurement results.....	53
4.2.3 Monte Carlo simulations	56
4.2.4 Discussion of the impact ionization dynamics	59
4.2.5 Energy loss mechanisms in high electric fields.....	62

4.2.6 Optical probing of the nearfield profile of metallic antennas.....	64
4.2.7 Conclusion.....	66
4.3 THz pump-THz probe measurements	67
4.3.1 Antenna resonance frequency shift	67
4.3.2 Modelling of the nonlinear frequency shift of the antenna	68
4.3.3 Isolating the nonlinear signal in the sample	72
4.3.4 Results of the pump-probe measurements and simulations.....	74
4.3.5 Conclusion.....	81
Chapter 5 Broadband THz spectroscopy of silicon carbide	83
5.1 Introduction to silicon carbide.....	83
5.2 Folded zone phonon modes in SiC.....	85
5.3 Experimental technique.....	88
5.4 Measurement results and discussion	91
5.5 DFT simulation of the phonon modes.....	97
5.6 FTIR measurement results.....	101
5.7 Conclusion.....	102
Chapter 6 THz-induced nonlinear transmission in silicon carbide.....	103
6.1 Introduction	103
6.2 Electronic properties of silicon carbide	104
6.3 Characterization of sample with low-power THz sources.....	107
6.3.1 Transmission measurements with a weak THz signal.....	108
6.3.2 Transmission measurements in the broadband THz Setup.....	110
6.3.4 Conductivity modeling with Drude-based models	112
6.3.5 Temperature dependence of the free carrier density	115
6.4 Nonlinear THz transmission in the 4H-SiC sample	120
6.4.1 Measurement setup.....	120
6.4.2 Results and discussion.....	121

6.4.3 Time-resolved dynamics of the THz-induced nonlinear transmission.....	128
6.5 Conclusion.....	132
Chapter 7 Conclusions and future perspectives.....	133
PhD publications	139
Peer reviewed journals	139
Conference contributions	139
References	143

Chapter 1

Introduction

It is fascinating to see light emitting diodes convert electric current to light; solar cells produce electricity from sunlight or integrated transistors in mobile chips, computer chips and other electronic systems produce all the wonderful functionalities that we use on a daily basis. Behind all these functionalities lie interactions of electrons with electric field in a microscopic level. Most physical processes that influence the carrier-field interactions happen on time scales of picosecond and femtosecond. Apart from the fundamental understanding of physical processes occurring in femtosecond and picosecond timescales, full understanding of dynamics of the charge carrier interactions with electric field is essential to advance the performances of these devices and design new functionalities. Sub-picosecond, terahertz (THz) electric field pulses enable investigations of these ultrafast interactions with sub-picosecond temporal resolutions.

THz electromagnetic wave covers frequencies of 0.1–10 THz, which corresponds to a wavelength range of 30 μm –3 mm. The corresponding photon energy range of a THz radiation is 0.4–41 meV. The low photon energies cover peculiar energy region in solid state physics such as free carrier absorption peaks, quasi-particles binding energies, energy levels of the lattice vibrations (phonons), magnons, interband transition energies in low dimensional systems and dopant state binding energies [1]–[3]. Consequently, THz provides access to a wealth of resonances in condensed matter and it has been used extensively to probe these inherent properties of materials. Not only does it probe resonance dynamics, strong THz field enables selective excitation of these low energy resonances such as molecular rotations, crystal lattice vibrations, excitation and acceleration of

electrons which helps the understanding of the dynamics of these processes in pump-probe measurements.

The dielectric properties of semiconductors are strongly dispersive in the THz spectral region. This enables characterization of conductivity properties on sub-picosecond temporal resolutions in a non-contact manner. Over the last few decades THz has developed into a mature technique in studying free carrier conductivity dynamics in semiconductors [4], [5]. It is applied to probe the microscopic electronic interactions of bulk semiconductors and nanomaterials in equilibrium as well as in photoexcited states. The possibility to measure the phase of a transmitted THz pulse in a time domain spectroscopy (TDS) allows quantization of complex conductivity.

A much smaller frequency of THz signals as compared to optical fields means very large pondermotive energy ($\mathcal{E}_p \sim E^2/\omega^2$), where E is the electric field strength and $\omega/2\pi$ is the frequency, for a given electric field. Such a strong interaction with free carriers implies that electrons can be energized beyond the ionization energy of, for example, dopant states. Interband transitions can also be induced by an intense THz field through scattering processes. Hoffmann, *et al.* demonstrated that an intense THz radiation causes carrier heating and amplification by impact ionization in indium antimonide (InSb) in electric fields of up to 100 kV/cm [6]. THz electric field has shown to be a successful mechanism to induce and probe intervalley and intravalley scattering dynamics in bulk semiconductors such as gallium arsenide (GaAs), silicon (Si), germanium (Ge) and indium gallium arsenide (InGaAs) [7]–[11].

Due to substantial advancements of ultrafast high power lasers, dramatic advances in THz generation technology in recent times have been achieved. Consequently, generation of electric field pulses exceeding 1 MV/cm on tabletop systems has been possible [12]–[16]. Extremely strong

electric fields in MV/cm and decades of MV/cm have also been achieved by using field enhancing metallic structures and metamaterials [17]–[20]. These achievements enable investigations of high field responses in semiconductors in strong electric regime such as high harmonic generations, Bloch oscillations and THz-induced field emission spanning from THz to the UV spectral range [21]–[23]. Extremely strong electric field pulses also demonstrate their capability to induce irreversible material damage [24].

Access to the THz field in MV/cm provides a new way of investigation and control of carrier dynamics in semiconductors. Extremely strong THz field demonstrates the capability to induce and investigate phase transitions in semiconductors; for example, Liu, *et al.* demonstrated insulator-to-metal transition in vanadium dioxide induced by THz pulse in MV/cm [25]. An intense THz can also drive charge carrier coherently to a very high energy such that extraordinary carrier multiplication can happen in semiconductors with bandgaps larger than 1 eV modifying their conductivity significantly [26]–[28]. Lange, *et al.* demonstrated that interband tunneling and impact ionization driven by THz field in undoped GaAs generates enormous density of electron-hole plasma which resulted in a complete switching-off of a metamaterial resonance [20]. Vicario, *et al.* recently revealed that an ultra-strong THz electric field provokes extreme cross-phase modulation and a staggering five times spectral broadening of co-propagating femtosecond laser pulse in an electro-optically active gallium phosphide (GaP) [29]. These exemplary reports demonstrate the potential of THz electric field in the control and manipulation of transient states of semiconductors happening in sub-picosecond time scales. These ultrafast nonlinearities will have implications in future ultrafast nonlinear THz devices such as saturable absorbers, optical limiters, frequency tunable antenna switches and all-optical signal processing systems.

Investigation of carrier dynamics in high electric fields regime is not only a necessity for the fundamental physical understanding and future functionalities; extremely strong electric fields can also be induced in nanodevices as feature sizes continue to miniaturize. Recently, devices with feature sizes of sub-10 nm and THz switching speeds are being introduced in working devices [30]–[32]. With such feature sizes application of standard gate voltage can induce electric fields in MV/cm. The device responses in these situations need to be understood for optimal functionality. With recent advances to generate extremely strong electric field pulses combined with its low photon energy, THz electric field can be adjustable bias ranging from sub-kV/cm to decades of MV/cm. It can be applied in a noncontact manner to investigate field-dependent carrier transport properties in semiconductors. This is particularly important for the most common semiconductor in micro- and optoelectronics, silicon.

Silicon is also an important material platform to fabricate THz devices due to its high transparency. In strong electric fields its transparency can be compromised. A THz field in MV/cm induces enormous density of carriers by impact ionization even from high resistivity silicon. While its nonlinear properties can be utilized for important switching and modulation applications, its breadth of applicability can be limited by nonlinear responses in strong electric fields. That requires a more robust material alternative that stays linear under application of strong electric fields in MV/cm. Silicon carbide (SiC) has approximately five times larger breakdown voltage. It has a large bandgap which implies that its impact ionization threshold is higher than that of silicon. SiC has also other interesting attributes such as high radiation resistance, high drift velocity, high thermal conductivity and melting point which are ideal for high power THz applications analogous to its success in high power electronics [33], [34].

While it is known that some polytypes of SiC have higher saturation velocity and mobility which is desirable for fast switching [35], [36], its dielectric and conductivity properties are not understood to the level of other common semiconductors such as Si or GaAs. With invigorated interest in SiC for optoelectronics applications, full understanding of its electronic properties is essential which can be revealed by THz spectroscopy. Even if undoped SiC has high THz transparency [37], the possibility to induce nonlinear transmission dynamically using intense THz widens its application.

In this thesis investigation of the dynamics of THz-induced nonlinearities in silicon and silicon carbide are presented. By using simple dipole antenna to extend the THz electric field into the MV/cm regime, impact ionization dynamics in silicon is investigated. Experimental techniques such as standard THz-TDS, THz pump-THz probe and optical plus THz pump-optical probes are implemented to understand the time-resolved dynamics of the impact ionization process. These experiments supported by Monte Carlo simulations clarify other physical processes that influence the impact ionization dynamics and its field dependence. Results on lattice vibration dynamics and conductivity properties of SiC, examined by broadband THz source, are also presented. A THz-induced nonlinear dynamics in a doped-SiC sample is investigated by standard THz-TDS and THz pump-THz probe measurements.

The thesis is organized in seven chapters. Chapter 2 begins by describing the THz generation and detection techniques. Special focus has been given to techniques that are used to perform the experimental results presented in this thesis. THz field enhancement by using metallic dipole antenna to reach strong electric fields of several MV/cm is described. The chapter covers description of experimental details which were used to obtain the results presented in this thesis. In chapter 3 the investigation of THz-

induced impact ionization in silicon by the standard THz-TDS is presented. Mechanism of resonance frequency shift of a metallic dipole antenna by impact ionization is described. The results of the experimental investigations of time-resolved dynamics of carrier generation are presented separately in chapter 4. Two investigation techniques that involve different probing signals are implemented. First, results of optical plus THz pump-optical probe measurements are described. In this technique the carrier density dynamics is directly monitored by measuring reflectivity change of a tightly focused 800 nm probe pulse. The time-resolved impact ionization dynamics as well as the influences of various carrier-field interaction mechanisms such as phonon scattering, Auger recombination, field screening and electron-hole scattering on the impact ionization dynamics are illustrated. The field-dependent property of impact ionization is also elaborated by altering the incident THz field strength. In the second part of the chapter results of THz pump-THz probe experiments are presented. In this technique a weak THz pulse is used to probe the carrier dynamics. The dipole antenna resonance shift is modelled by a simplified harmonic model to interpret the experimentally measured antenna resonance shift as a function of pump-probe delay time.

The next two chapters focus on the investigations of silicon carbide in which the dielectric and conductivity properties as well as THz-induced nonlinear transmission in doped SiC are presented. Chapter 5 discusses linear THz spectroscopy results of SiC obtained by broadband THz source. The dynamics of weak folded-zone phonon modes in *4H*- and *6H*-SiC samples are illustrated. Characterization of doped *4H*-SiC sample that shows a nonlinear THz transmission is presented in the first sections of chapter 6. The broadband THz source has been used to characterize conductivity parameters. Then THz-induced nonlinear transmission in the sample, where ultrafast sub-picosecond modulation of THz transmission is observed, is

described in this chapter. Finally conclusion and future perspectives are outlined in chapter 7.

Chapter 2

Intense terahertz generation and detection

2.1 Introduction

The terahertz (THz) spectral range had been relatively unexplored due to the difficulty in its generation and detection. Electronic sources for microwave signals tend to be inefficient at high frequencies. Similarly, optical sources were not efficient in generation radiation at of low frequencies. Due to its inaccessibility, the THz spectral range is used to be known as the THz gap. In the last two decades, THz generation and detection technologies have made significant strides; consequently, THz has been applied over a wide range of applications. Several articles and review papers have been published on the generation and detection of the THz radiation [38]–[40]. In this chapter, the THz generation and detection techniques used during this PhD work are described briefly. Following the description of generation and detection techniques, experimental setups that are used to perform the investigations are discussed.

The most widely available commercial THz sources are photoconductive antennas, pioneered by D.H. Auston [41]. In this technique two electrodes (or antennas) are fabricated on a semiconductor substrate close to each other. An ultrashort laser pulse excites electrons by interband transition in the semiconductor at the gap between two electrodes. An electric field bias applied to the electrodes accelerates the optically generated electrons. Such a sharp change in current generates THz radiation that has a

temporal profile proportional to the derivative of the photoconductive current. Photoconductive antennas can also be used for coherent detection of THz pulses. In this case, an applied THz electric field acts as bias and in the presence of optically generated electrons a photocurrent across the gap is induced. The measured current is directly proportional to the electric field of the THz pulse. The THz transient generated by a photoconductive antenna is typically weak. However, large area photoconductive antennas can generate few tens of kV/cm. The THz radiation from photoconductive antennas has a bandwidth that ranges between 0.05 THz and 2–6 THz [42]–[45].

A broadband THz pulse with bandwidth of several decades of THz can be generated by a two-color laser mixing in a laser-induced air plasma [46]–[48]. In this technique, a fs pulse and its second harmonic are focused to generate an air plasma. An asymmetric current in the air plasma region generates a broadband THz radiation where the bandwidth is limited by the pulse width of the driving laser pulse. This technique is unique in its broad bandwidth, but high peak power can be achieved with this technique. Kim, *et al.* demonstrated single cycle pulses with peak electric field >8 MV/cm which have been generated in air plasma with a fs laser amplifier providing 30 fs pulse width and 15 mJ pulse energy. A broadband THz detection and waveform measurement is also possible in the reverse process called air-biased coherent detection (ABCD) [49], [50]. In this case, the second harmonic of fs a probe pulse, that is proportional to the THz field, is generated in a third order nonlinear interaction between the THz electric field and the fs laser pulse. By detecting the second harmonic intensity, the THz radiation is detected.

While weak THz signal (from the T-Ray 4000 system by Picometrix) and broadband THz pulse generated by two-color air plasma are used briefly during this PhD work, most of the results presented in this thesis are produced by THz pulses generated by optical rectification. The THz pulses

are detected coherently by electro-optic sampling. Therefore these techniques are discussed in more detail in the subsequent sections.

2.2 THz generation with optical rectification

Optical rectification is a second order nonlinear process where interaction of two optical fields in a nonlinear medium will have a response of $\chi^{(2)}(0; \omega_0 - \omega_0)$, where $\chi^{(2)}$ is second order susceptibility and $\omega_0/2\pi$ is the frequency of the incident field. If the optical pulses are monochromatic and have identical frequency, a DC polarization will be generated. Ultrafast optical pulses have a finite spectral bandwidth. If only a single ultrafast optical pulse is incident on the nonlinear crystal, mixing of different frequency components of the pulse gives rise to a short THz transient.

Efficient THz generation using optical rectification requires a non-centrosymmetric material ($\chi^{(2)} \neq 0$) with a high second order nonlinear coefficient. Examples of such materials include zinc telluride (ZnTe), lithium niobate (LiNbO₃), gallium phosphide (GaP) and organic crystals DAST and DSTMS. LiNbO₃ has a high nonlinear coefficient ($r = 30.9$ pm/V) and a high damage threshold in the application of high power fs laser pulses. While organic crystals can have a high nonlinear coefficient and easier phase matching in a collinear scheme, their low damage threshold is a limiting factor in their functionality.

As is typical for optical nonlinear processes, efficient generation of THz pulses requires phase matching between the THz pulse and the optical pump. The ideal phase matching condition is fulfilled when the group velocity of the pump pulse matches the phase velocity of the THz pulse. The phase velocity of the THz waves is more than two times smaller than the group velocity of the 800 nm pump in the LiNbO₃ crystal [39]. In an optical arrangement where the output THz pulse and the optical pump are collinear, the conversion efficiency is very low as THz pulses generated in different

depths of the crystal do not interfere constructively due to the difference between the phase velocity of the THz radiation and the group velocity of the optical pump. A significant leap in tabletop high power THz generation has been achieved by implementing tilted-phase front geometry [51]. In this technique, the pump pulse front is tilted inside the LiNbO₃ crystal such that THz generated across the crystal adds up constructively.

The near infrared (NIR) laser (at 800 nm) pulse front is tilted using a combination of grating and imaging systems to achieve phase matching inside the LiNbO₃ crystal [12], [39], [51], [52]. The schematic of the setup is shown in Fig. 2.1. We used a grating with 1800 lines/cm to tilt the pulse front. The grating is imaged onto the LiNbO₃ crystal by a combination of lenses in 4*f*-lens arrangement. The lenses are cylindrical with focal length of $f_1 = 250$ and $f_2 = 150$ mm for Lens 1 and Lens 2 respectively. The imaging system enables optimum THz propagation characteristics for efficient optical-to-THz conversion. The THz radiation is emitted perpendicular to the pulse front. In this scheme the component of the pump pulse group velocity along the THz propagation direction matches the phase velocity of the THz pulse. The LiNbO₃ crystal is cut so that the pump pulse will be incident on the crystal perpendicularly and THz leaves the crystal in a direction normal to the facet. The cutting angle of the crystal near the corner where THz is generated has an angle of 62-63°.

2.3 THz detection with electro-optic sampling

Measurement of the amplitude and phase of a THz pulse is possible using the principle of a linear electro-optic (EO) effect also known as the Pockel's effect [53]. In linear electro-optic sampling a THz electric field induces a change of index of refraction along the different axes in an electro-optically active medium [54]. The modification of the index ellipsoid is translated into

a phase retardation between weak NIR fs probe pulse components propagating along the different axes of the EO crystal.

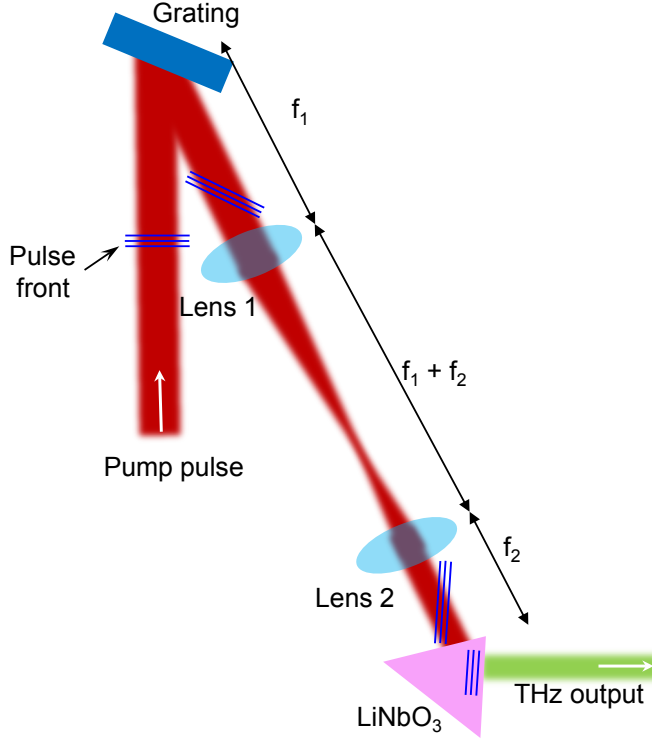


Figure 2.1. Schematic diagram of the THz pulse generation setup in a tilted-pulse front geometry. The grating has 1800 lines/cm. Cylindrical lenses with focal lengths of 250 mm (Lens 1) and 150 mm (Lens 2) are used for imaging the grating on to the LiNbO_3 crystal and adjusting the pulse front tilt angle. The blue wavy lines indicate pulse front of the NIR pump.

Zink Telluride (ZnTe) is one of the most widely used nonlinear crystals for coherent electro-optic THz transient measurements because of its high sensitivity associated with a high nonlinear coefficient and excellent match between the group velocity of probe pulse and phase velocity of the THz pulse in collinear scheme. Consequently, a co-propagating THz and a probe pulse will have a long interaction length [55], [56]. The THz spectral range

detected by ZnTe is limited in frequency by strong phonon absorption by TO phonon at 5.3 THz [55]. If THz detection over broader spectral range is required, GaP is used alternatively for high sensitivity EO detection of up to 7 THz [57].

The schematic of the detection setup by EO sampling in a balanced detection system is shown in Fig. 2.2. $\langle 110 \rangle$ ZnTe, which has an isotropic material index ellipsoid, is used for the EO detection as its detection bandwidth covers the THz radiation generated by the LiNbO₃ crystal. The probe pulse is linearly polarized before the detection crystal. In the absence of a THz pulse, ZnTe does not affect the polarization of the propagating probe pulse and the linearly polarized light is converted to a circularly polarized light in a quarter-wave plate. Application of a THz field polarized parallel to the probe polarization introduces birefringence in the crystal. Consequently, the polarization of the probe pulse is modified. The transmitted probe pulse propagates through the quarter-wave plates will be an elliptically polarized light. The Wollaston prism separates the light components propagating along the ordinary and extraordinary axes. In the case of elliptically polarized light, the balanced photodiodes measure a differential signal which is picked by a lock-in amplifier. The lock-in amplifier is phase-locked to an optical chopper that modulates the THz beam. The differential signal is proportional to the incident THz electric field in the limiting case when the differential signal of the photodiodes is much smaller than the signal from each photodiode. The exact relationship between the electric field strength and the differential signal is [58],

$$E_{THz} = \sin^{-1} \left(\frac{\Delta I}{I} \right) \frac{c}{\omega n^3 r_{41} L} \quad (2.1)$$

Where $\Delta I/I$ is the relative differential intensity between the two photodiodes, ω is the angular frequency of the probe pulse, $r_{41} = 4 \text{ pm/V}$ is

the nonlinear constant of ZnTe [57] is the component of the electro-optic tensor, L is the thickness of the EO crystal and c is the speed of light in vacuum.

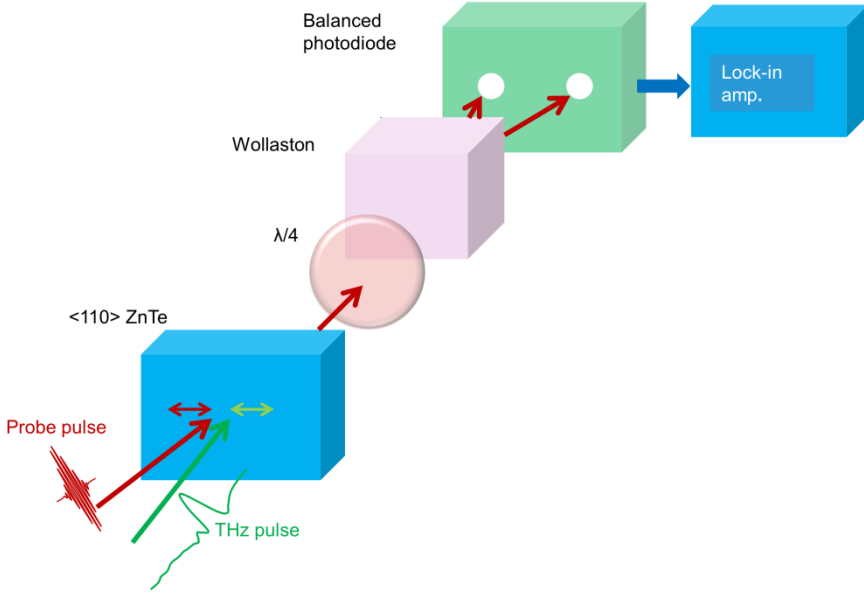


Figure 2.2. Schematic diagram of THz pulse measurement by EO sampling using a 500 μm ZnTe crystal. A combination of quarter-wave plate ($\lambda/4$), Wollaston prism and balanced photodiodes separates the probe pulse components along the ordinary and extraordinary axes and the lock-in measures the differential signal between the balanced photodiodes. Overlapping a THz pulse with a probe pulse introduces a non-zero differential signal that can be related to the THz electric field strength.

The fs probe pulse duration is smaller than the THz pulse duration. By variably delaying the probe pulse with respect to the THz pulse, a time domain THz field transient is mapped. A typical THz transient measured by electro-optic sampling is shown Fig. 2.3. The electric field strength is calculated based on Eq. 2.1. The THz pulse has peak field strength > 250 kV/cm. The inset shows the amplitude spectrum obtained by calculating the Fourier transform of the time-domain pulse. The spectrum of the measured

THz signal shows spectral availability of up to approximately 3 THz from LiNbO₃ crystal.

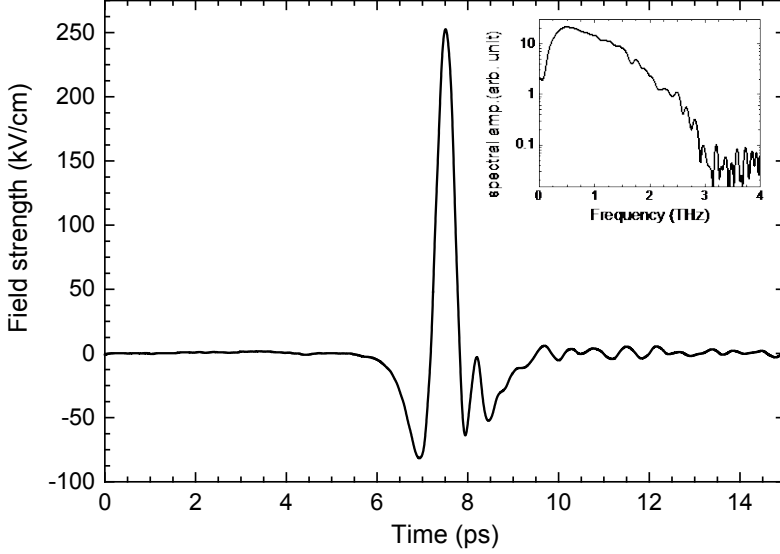


Figure 2.3. THz transient generated by optical rectification in LiNbO₃ and measured by electro-optic sampling in the ZnTe crystal. The inset shows the corresponding spectral amplitude.

2.4 THz field enhancement with antenna arrays

Antennas are widely used in the radio frequency and microwave spectral regimes mainly for communication applications such as in wireless communication and broadcasting. With fast progress in the area of THz communication [59]–[61], the extension of antenna popularity from the microwave to the THz spectral range is inevitable with the potential of THz spectral band to provide ≥ 100 times faster data communication than the present day Wi-Fi networks [62]. While the farfield properties of antennas are relevant for communication applications, its nearfield properties enable

field confinement to sub-wavelength dimensions and significant enhancement of field strength.

Metallic antennas and metamaterials fabricated on top of a dielectric substrate have shown the capability to provide significant local field enhancement [63]–[65]. They provide a cheap alternative to get extremely strong THz electric fields in MV/cm and decades of MV/cm. These strong electric fields are important for the investigation of strong field-matter interaction in condensed matter. In this work, simple dipole metallic arrays are used to enhance THz fields at the dipole antenna hot spots near its tips and achieve electric fields of several MV/cm. While using antenna arrays instead of single antenna avoids the difficulty in spatial alignment of the THz peak with a single antenna, it has an added advantage that plasmonic coupling of the lattice modes of the antenna array with the resonance of a single antenna increases the field enhancement [66].

Periodic gold antenna arrays are fabricated on high resistivity silicon (HR Si) substrates by the standard UV lithography. A scanning electron microscope image of a gold antenna array with a resonant frequency of 0.6 THz is shown in Fig. 2.4(a). A single dipole antenna has length of 80.6 μm , a width of 5 μm and a thickness of 200 nm. The periodicity of the antenna array in both directions is 143.8 μm .

The electric field profile and field enhancement are investigated by full-wave electromagnetic solver using a commercial software package (CST microwave studio). In the modeling of the antenna array the dimensions are set according to the measurements of the fabricated sample. Periodic boundary conditions are implemented in the x- and y- directions to represent the periodic antenna arrays while considering a single antenna for simulations. A lossy metal with electrical conductivity of 4.56×10^{-7} S/m is used to model the optical constants of gold. The real part of dielectric constant of silicon is set to be 11.7 as specified by the supplier (Topsil) and

in agreement with literature in the THz range [67]. The antenna system is excited by a plane wave source input with a measured temporal profile similar to the one shown in Fig. 2.3. The calculated field profile of a single antenna unit is shown in Fig. 2.4(b). The color scale is limited to only 4.32 at the peak of the response in time domain, even though a maximum field enhancement higher than 30 in time domain is obtained, to better visualize the field profile near the antenna.

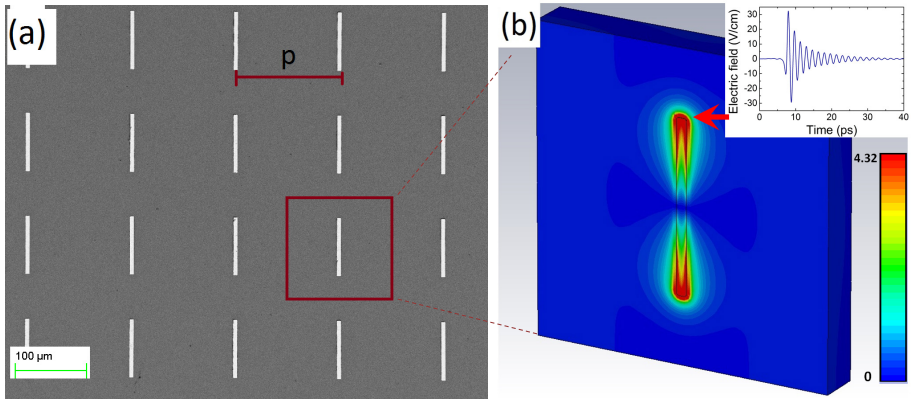


Figure 2.4. (a) Scanning electron microscope (SEM) image of a periodic gold antenna array designed for a resonance frequency at 0.6 THz. (b) Simulated time domain THz electric field profile in the vicinity of a single antenna unit. The antenna has a length of 80.6 μm, a width of 5 μm and thickness of 200 nm. The periodicity of the antenna array in both directions is 143.8 μm. The inset shows the magnitude of electric field at the tip of an antenna for an incident plane wave with peak electric field of 1 V/m showing field enhancement higher than 30 at a depth of 10 nm below the silicon surface.

2.5 THz time-domain spectroscopy setup

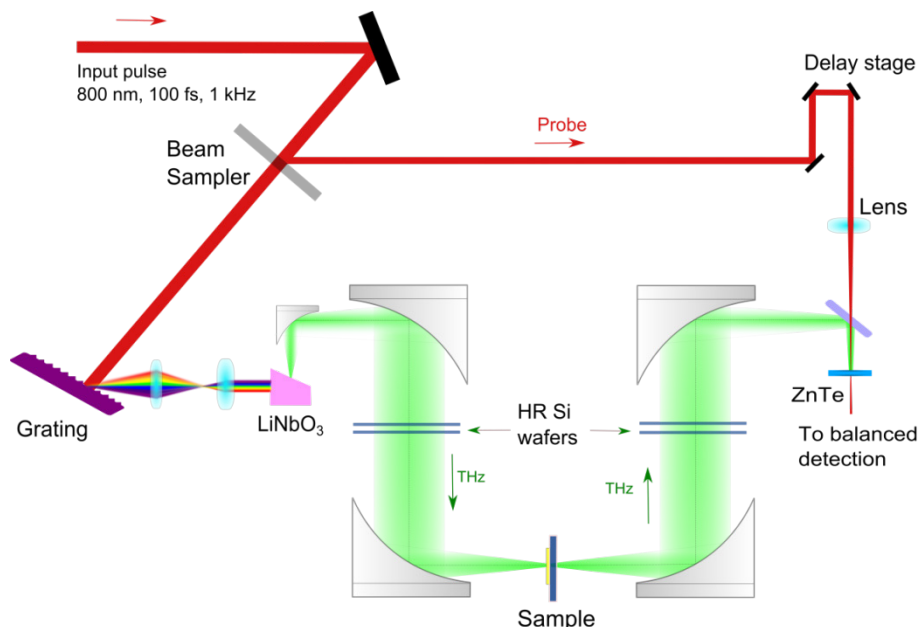


Figure 2.5. Schematic diagram of the experimental setup in a THz-TDS. A 800 nm laser pulse from a regenerative Ti:sapphire amplifier generates THz radiation in a LiNbO₃ crystal. The THz pulse is collimated and focused at the sample location using a set of off-axis parabolic mirrors. The transmitted THz signal is imaged onto a ZnTe crystal where it overlaps with the probe pulse for THz detection.

A standard THz time-domain spectroscopy (THz-TDS) setup in transmission mode is shown in Fig. 2.5. A nearly single cycle THz field is generated by optical rectification in a LiNbO₃ crystal in a tilted-wave front geometry by 800 nm pulse from a Ti:sapphire regenerative amplifier (Spitfire Ace). The laser pulses from the amplifier have energy of up to 6 mJ, a pulse width of 100 fs and a repetition rate of 1 kHz. The near infrared (NIR) beam is separated into two parts using an optical sampler. The major portion of the beam, which passes through the optical sampler, is used for THz generation and a small fraction of the beam reflected from the sampler is used as a

probe beam for the THz electric field measurement by electro-optic sampling.

To obtain an intense THz electric field, focusing the THz beam tightly at the sample position is crucial. A set of five 90° off-axis parabolic mirrors are used in the setup for the tight focusing at the sample location and imaging on detection crystal. A photograph of part of the optical setup that contains the off-axis parabolic mirrors is shown in Fig. 2.6 (a). The green line indicates the THz beam path. THz radiation from the LiNbO₃ crystal is collimated and focused onto the sample using a set of 3 off-axis parabolic mirrors with focal lengths of 1", 6" and 2" arranged in that order starting from the THz source. Pulses transmitted through the sample are again collimated and imaged onto a 0.5 mm thick <110> ZnTe crystal by a pair of off-axis parabolic mirrors (2" and 6") for detection. To overlap the THz beam and the detection NIR beam, the THz beam is reflected by an ITO mirror at 45° which is transparent to the NIR beam.

Careful alignment of the off-axis parabolic mirrors is done with the support of a commercial THz camera (NEC IRV-T0831)). The THz camera images at locations of approximately 5 cm away from the LiNbO₃ crystal, at the sample and at the detection crystal are shown in Fig. 2.6(b-d). It is shown that the THz beam is effectively focused at the sample position which is essential to achieve an intense electric field needed for nonlinear spectroscopy in semiconductors. The horizontal beam profile at the sample focus is shown as an inset in Fig. 2.6 (c). The full-wave half maximum along the horizontal dashed line is 270 μm. For comparison, the diffraction limited spot size at 1 THz is, $\lambda/2NA = 188 \mu\text{m}$ where a roughly estimated numerical aperture, $NA = 0.8$, is used.

(a)

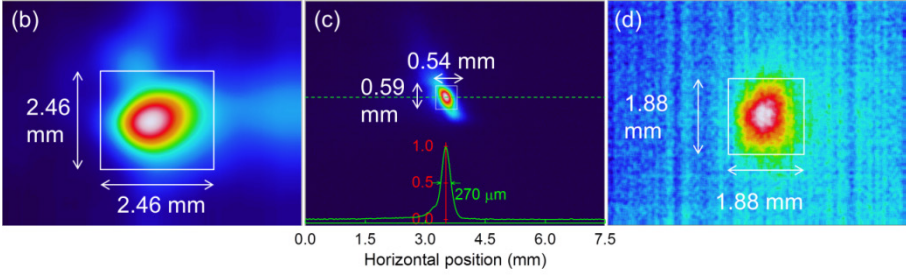
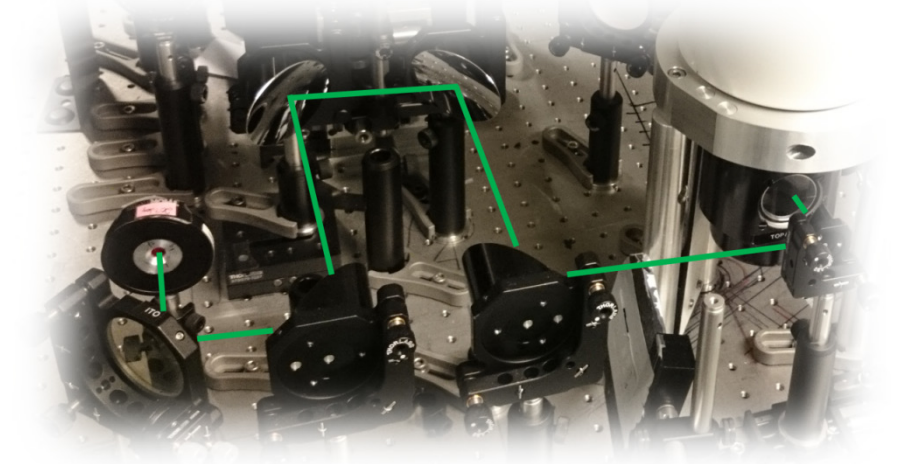


Figure 2.6. (a) A Photograph of part of the optical setup that contains the off-axis parabolic mirrors. The green line indicates the THz beam path. THz beam profile imaged by a commercial THz camera (NEC IRV-T0831) (b) approximately 5 cm away from LN crystal, (c) at the sample position, and (d) at the detection crystal location. Dimensions of rectangular regions around the THz images are included to show relative beam spot size.

The THz signal detection is done by free space electro-optic sampling. To avoid over rotation and any nonlinearities [68], [69] in the electro-optic detection, we decrease the intensity of THz wave on the ZnTe crystal by inserting a set HR Si in the path of the collimated THz beam. A single wafer reduces the electric field by factor of Fresnel transmission equivalent to $4n/(nt + 1)^2 \approx 0.7$, where $n = 3.417$ is the refractive index of silicon at

THz frequencies. Placing a set of nine silicon wafers results in reduction of electric field by a factor of $(0.7)^{-9} = 24.8$. The silicon wafers are also used to vary the THz field strength at the sample location by relocating the silicon wafers in the THz beam path before and after the sample. The total number of HR Si in the beam path is kept constant to maintain a constant THz field strength at the detector.

2.6 THz pump-THz probe experimental setup

To investigate the time-resolved nonlinear dynamics induced by an intense THz pulses in silicon (Si) and silicon carbide (SiC), a THz pump-THz probe setup is implemented. The schematic diagram of the optical setup is shown in Fig. 2.7. Two collinear THz beams are generated by optical rectification in a single LiNbO₃ crystal in tilted-wavefront geometry. The NIR laser pulse from the Ti:sapphire regenerative amplifier is used for generation of the THz pulses. The NIR pulse is split in 1:10 ratio using a beam splitter. 90% is used to generate the THz pump and the 10% is variably delayed and used to generate the THz probe pulse. The two NIR beams are recombined at very close incident angles on a holographic diffraction grating with 1800 lines/mm at the same spot and co-propagate almost together afterwards. The THz generation, imaging and detection are the same with the standard THz-TDS setup described in section 2.5.

For selective measurement of the two THz pulses optical choppers are placed in the beam paths of NIR beams that generate the THz pulses. By locking the frequency of the lock-in amplifier with either the modulation of the probe pulse or the pump pulse, selective measurement is possible in the presence of the other. Calibration of the detected THz profile using the well-known electro-optic coefficient [57] of the detection crystal shows that the THz pump pulse has a peak electric field higher than 300 kV/cm and probe pulse has a peak of approximately 20 kV/cm. Representative pump and

probe pulses with a pump-probe delay of -3 ps are depicted in Fig. 2.8. In most of the pump-probe measurements, the THz beam path is purged with dry nitrogen to reduce THz absorption by water vapor.

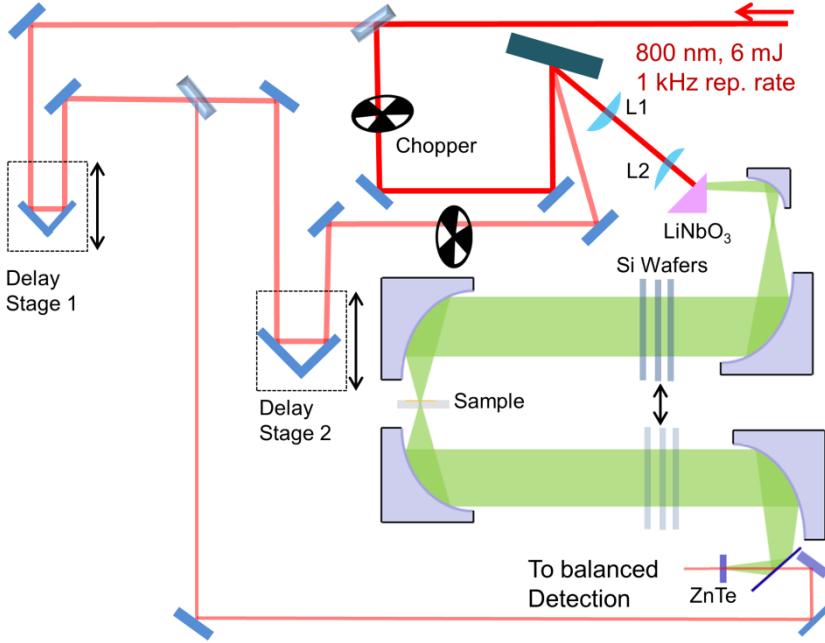


Figure 2.7. Schematic of THz pump-THz probe experimental setup where the THz is generated in a single LN crystal. The high power 800 nm pulse is split into three branches. 90 % of the intensity is used to generate THz pump and a variably delayed 10% is used for THz probe generation in the same LN crystal. A small fraction the THz probe generating beam is used for the EO sampling. The two THz pulses propagate collinearly. Notice that the difference in incident angle on the grating between the two NIR beams is exaggerated.

Since both the pump and probe THz pulses are generated and detected by the same generation and detection crystals, a nonlinear interaction near the temporal overlap of the THz pump and THz probe pulses is expected. This is clearly demonstrated in probe peak scan without sample as a function of pump-probe delay time shown in Fig. 2.9 (a). In the probe peak scan the

optical probe measures the peak of the probe pulse while the pump-probe delay time is varied. Near the temporal overlap of the two THz pulses, the probe peak undergoes extraordinary transformation due to nonlinear effects in both the generating and detection crystals.

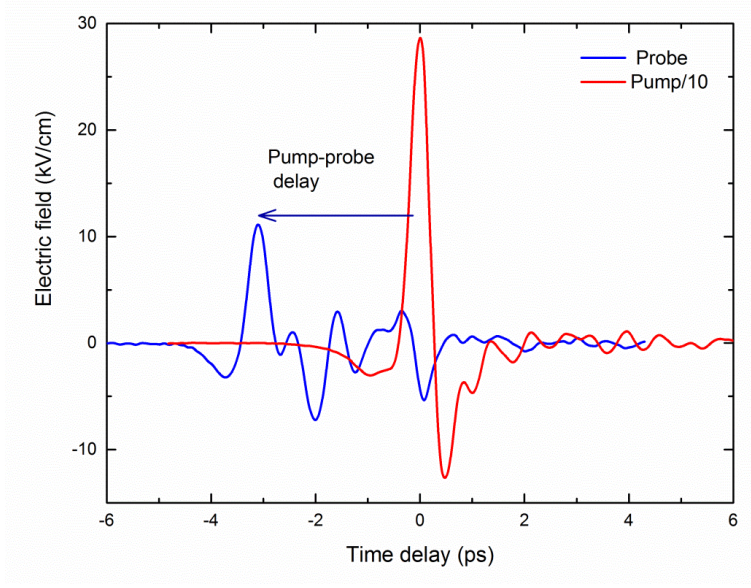


Figure 2.8. Representative pump and probe pulses at the pump-probe delay time of -3 ps. The pump is scale down by a factor of 10 for a better visual account.

In the time window of the scan presented in Fig. 2.9(a) we observe distortions of the peak scan near time delay of 0 ps and 12.5 ps. The distortion near pump-probe delay time of 12.5 ps in the peak scan is due to the nonlinear effect in the detection crystal alone. At this pump-probe delay, there is no temporal overlap of the NIR pumps in the generation crystal. This time delay corresponds to the overlap between the THz probe pulse and the Fabry-Perot reflection pulses from the attenuating silicon wafers of the THz pump pulse. It is to be noted that the first Fabry-Perot reflected THz pulse from six attenuating wafers used in this scan is larger than the transmitted THz pulse. So we expect less nonlinear

effect induced in the detection crystal near time delay of 0 ps than that of nonlinear effect at 12.5 ps. The significant distortion near time delay of 0 ps is from nonlinear effects at both LN crystal and detection crystal (ZnTe). In the generating crystal, the presence of a strong NIR pump affects the THz generation by the weak NIR beam nonlinearly. Comparing the maximum deviations of probe peak near pump-probe delays of 0 and 12.5 ps, one can argue that the nonlinear effect near pump-probe delay times of 0 ps emanate mainly from LiNbO₃ crystal.

To minimize the influence of the nonlinear effect in the generation and detection crystals, a measurement scheme is implemented where the THz power on the sample changes while maintaining the same condition on the generation and detection crystals. In this scheme probe pulse transmission in full power THz pump and probe pulse in attenuated pump illumination is compared to analyze the time-resolved nonlinear dynamics induced by the strong THz pump. THz pump attenuation is achieved by placing a set of silicon wafers on the collimated section of the THz beam path. In the case of full pump pulse illumination, the silicon wafers are relocated to the beam path after the sample. In this way the nonlinear interactions at the generation and detection crystals are maintained the same while varying the incident field on the sample. This enables us to pick the nonlinear interaction induced only in the sample. This has been confirmed by making a pump-probe measurement in air without the sample. The difference in probe pulse with a full THz pump illumination and an attenuated THz illumination in air scan shows no nonlinear signal apart from noise at the overlap as shown in Fig. 2.9(b).

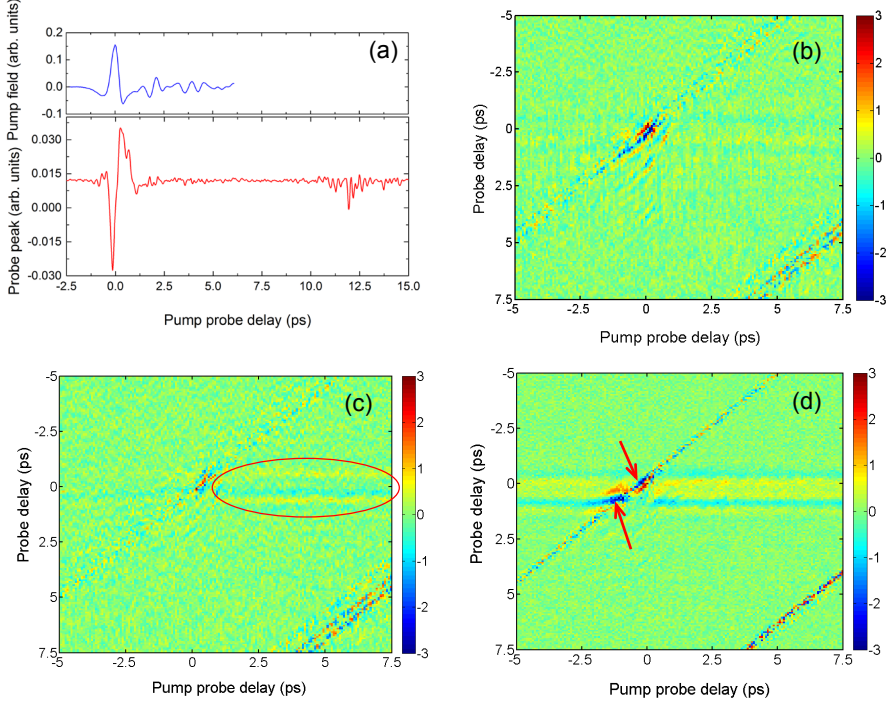


Figure 2.9. (a) Probe peak scan as a function of pump-probe delay time. The THz pump profile is shown in the top frame for reference. Time domain difference between probe pulse in full THz pump illumination and attenuated illumination as function of pump-probe time delay, (b) air reference, (c) high resistivity silicon sample, and (d) lightly doped silicon sample.

Time domain nonlinear signals, which are the differences between transmitted probe pulses with full pump illumination and attenuated illumination $(E_{\text{probe}}^{\text{nonlinear}}(t - \tau_{\text{pp}}) = E_{\text{probe}}^{\text{HP}}(t - \tau_{\text{pp}}) - E_{\text{probe}}^{\text{LP}}(t - \tau_{\text{pp}}))$ in a high resistivity silicon sample and a lightly doped silicon sample are shown in Fig. 2.9(c, d). τ_{pp} is the pump-probe delay time. In the case of HR Si sample, the nonlinear signal induced by a THz pump is almost nonexistent. There is only a very weak nonlinear signal near the peak of the probe pulse which stays even after the several ps's after the THz pump peak (see the red circle in (c)). This weak signal is

attributed to higher absorption by free carriers generated by THz-induced impact ionization. The details are covered in subsequent chapters. An example of a THz-induced nonlinear signal is observed in n-type lightly doped silicon sample. It can be observed that near pump probe delay time of zero, there is strong red and blue regions (see the red arrows (d)) which do not appear in high resistivity silicon. This nonlinear signal is attributed to hot-carrier effects and intervalley scattering which are reported by other authors [7], [70], [71]. As electrons are accelerated by the THz field beyond the energy differences of different valleys, they scatter into the side-valleys which have different electrons mobility due to the different effective masses. In silicon, electrons scattered into the side-valley have more effective mass and consequently lower mobility or higher transmission. This process happens in time spans in the order of a picosecond. This is in agreement with our observation in the pump-probe scan where the nonlinear signal has time span comparable to the THz pulse (see Fig. 2.9(d)).

In conclusion, generation mechanisms of an intense THz pulse, primarily by optical rectification in LiNbO_3 crystal, are discussed briefly. A Coherent detection method, where amplitude and phase of a THz pulse are measured by electro-optic effect in ZnTe , is also discussed. Field confinement by metallic dipole antenna arrays has been shown computationally shown to generate extremely strong electric fields of several MV/cm in the hot spots near the antenna tips. Finally optical setups that employ intense electric fields to investigate nonlinear effects in semiconductors and a way to isolate a nonlinear signal have been described. Results obtained with these setups are presented in the subsequent chapters.

Chapter 3

THz-induced impact ionization in high resistivity silicon

The observation of ultrafast impact ionization (IMI) and carrier generation induced by extreme sub-picosecond THz electric field pulses in high resistivity silicon (HR Si) is discussed in this chapter. Investigations are conducted by transmission THz-TDS which is discussed in section 2.5. Local terahertz electric fields of several MV/cm are obtained by field enhancement in the near field of a resonant metallic antenna array. The carrier multiplication is probed by the frequency shift of the resonance of the antenna array due to a change of the local refractive index of the substrate.

3.1 Introduction

Impact ionization is a carrier multiplication mechanism where energized conduction band electrons or holes in the valence band scatter with bound electrons to generate new electron-hole pairs [72]. In this process the free carriers need to be energized beyond the bandgap energy of the semiconductor so that they can transfer sufficient energy to lift the bound electrons to the conduction band. A possible impact ionization path way on band structure of silicon is depicted in Fig. 3.1. An external electric field, such as an intense THz pulse, energizes conduction band electron (process 1). During impact ionization scattering of the energetic electron with bound electron, the energetic electron losses it energy (process 2) and the conduction band electron is lifted to the conduction band (process 3) leaving behind a free hole. This schematic is a very simplified representation. Other physical processes are also involved that influence the field interaction. For

example, free carriers can scatter with lattice vibrations and dissipate energy before reaching impact ionization energy. The balance between acceleration of carriers and dissipation of energy plays an important role in the impact ionization dynamics.

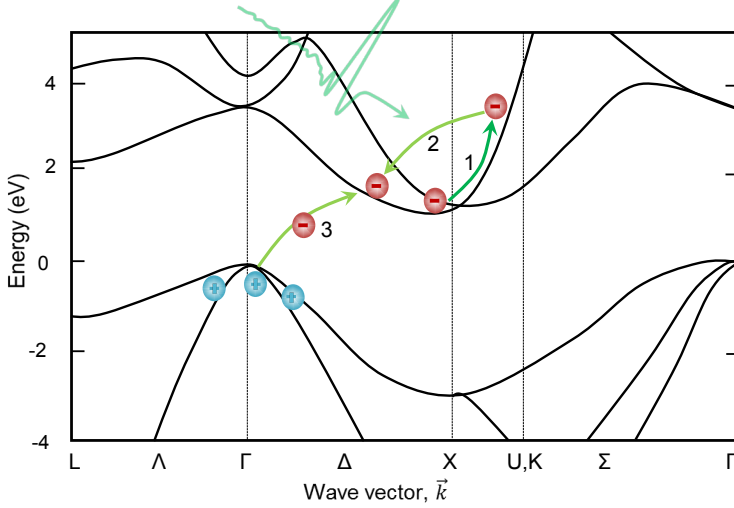


Figure 3.1. Possible impact ionization pathway on band structure of silicon. External electric field, such as THz pulse, accelerates conduction band electrons (1). Collision between energetic electron with bound electron in the valence band transfers energy from the energetic electron to valence band electron (2). This can create new electron-hole pair (3). The band structure is adapted from [75].

The impact ionization process continues in a cascaded manner in the presence of an external field such that a significant density of carriers can be generated. In the presence of a strong electric field the instantaneous potential energy in a semiconductor can also drop significantly over atomic distances, facilitating field-induced interband Zener tunneling [20], [73], [74]. This process can also generate a large density of carriers on ultrashort time scales. The two carrier generation mechanisms occur on a femtosecond time scale, and in many cases, it is difficult to identify the dominant carrier generation mechanism in a definitive manner.

Impact ionization in silicon has been investigated extensively [76]–[81]. So far experimental investigations of IMI are based on transport measurements with static electric field bias in doped p-n junction devices. These investigations are limited in electric field to sub-MV/cm due to heating and avalanche breakdown. Using ultrashort electric field pulses instead of static fields reduces the heating effect significantly and allows investigations of IMI in extreme electric fields in the MV/cm regime. Recently, intense THz pulses enabled investigations of impact ionization by purely optical methods in GaAs, InSb and InAs [26], [82]–[85]. It has been shown that extraordinary carrier multiplication through IMI has been possible with THz pulses where the photon energy is much smaller than the bandgaps of the semiconductors. In the case of silicon, THz photon energy is approximately 1/270 times smaller than the bandgap.

The possibility of applying a THz bias in a non-contact manner reduces complexity that arises from contributions from other components of the fabricated device and enables investigation of impact ionization in bulk semiconductors. In the conventional transport measurements of impact ionization from direct current (DC) transport the impact ionization region needs to be highly doped to obtain a functional device. Using intense THz pulses enables investigation of the dynamics of impact ionization process at low initial carrier concentrations, conditions that are not accessible in conventional transport measurements.

The THz electric field required for IMI in silicon is so high that our THz source alone is not capable of inducing measurable carrier multiplication. For that reason the local electric field is further enhanced by utilizing nearfield enhancement of the field provided by a metallic antenna array. This enables us to investigate IMI in silicon in a new field regime well into the multi-MV/cm. This is important not only for fundamental physical understanding of carrier transport in new field regime, but it is also an

important demonstration that the effect of IMI should be accounted for various THz devices fabricated on silicon at high THz field strengths [24], [86], [87].

Resonant behavior of the metallic antenna arrays plays another crucial role in this study in addition to local field enhancement in the vicinity of the dipole antenna. Its resonance frequency shift is used to probe the impact ionization process. Antenna theory predicts that the approximate value of a resonant frequency f_{res} of a metallic dipole antenna to be,

$$f_{res} = \frac{c}{2n_{eff}L}, \quad (3.1)$$

where L is length of the antenna; c is the speed of light and n_{eff} is the effective refractive index of the substrate [63]. If free carriers are generated by THz-induced impact ionization, the refractive index of substrate in the vicinity of the dipole antenna changes. The change in the effective refractive index of substrate shifts the resonance frequency of the dipole antenna which can be measured in a transmission THz-TDS. The change in resonance frequency is, thus, used to probe the dynamics and extent of free carrier generation.

3.2 Results and discussion

The sample is placed at the focus of an intense THz field from lithium niobate as shown in Fig. 3.2(a) in a setup described in section 2.5. The transmission of the intense THz pulse through the sample is measured for several incident THz field strengths. The electric field strength is varied by inserting attenuating silicon wafer on the collimated section of the THz beam path. The sample consists of antenna arrays made of gold fabricated on high resistivity silicon substrate. The HR Si substrate has an intrinsic carrier density of approximately $1.5 \times 10^{10} \text{ cm}^{-3}$ as specified by the supplier (Topsil). Antenna dimensions are: length = 80.6 μm , width = 5 μm , and thickness =

200 nm. The antenna array has a period of $143.8 \pm 6 \mu\text{m}$ which is optimized to maximize field enhancement at resonance frequency of 0.6 THz.

To obtain the transmission spectrum of the antenna array, the Fourier transform of the transmitted THz transient through the sample is divided by that of a bare HR Si reference. It is noted here that no measurable change of transmission through bare HR Si is observed even at highest available field strengths. Transmission spectrum through the antenna array exhibits a strong resonance centered at 0.6 THz at low THz incidence as shown in fig. 3.2 (b). The measured resonances are broad and their width is limited by the width of the time window of our measurement, which in turn is limited by arrival of the Fabry-Perot reflections from the sample, detection crystal and attenuating silicon wafers. The resonance frequency of the antenna red-shifts and slightly broadens with increasing THz field strength.

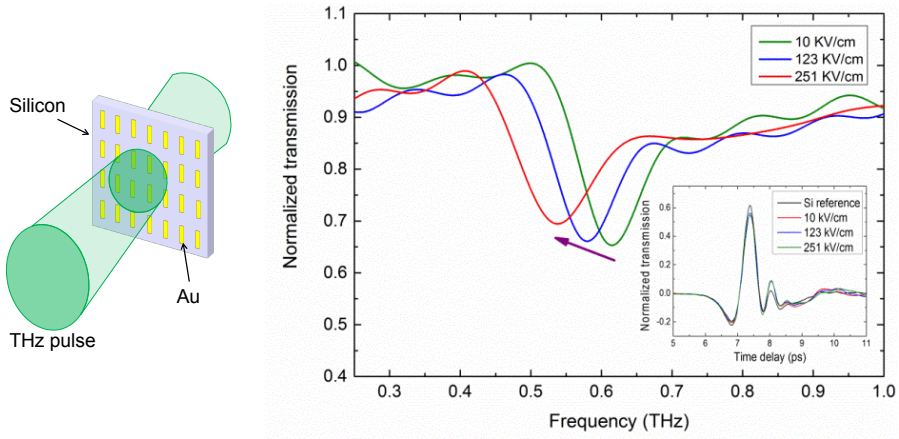


Figure 3.2. (a) Schematic of THz transmission through sample. Antenna array is fabricated on the HR silicon surface. (b) Measured spectral THz transmission of a gold antenna on a high resistivity silicon substrate for different incident THz peak field strengths. The arrow indicates direction of increasing THz field strength. Transmission is normalized to transmission through a bare HR Si wafer. The inset shows the transmitted THz transient for several incident THz field levels.

The change of the resonance frequency is attributed to change of optical properties of the substrate induced by the strong THz field. According to Eq. 3.1 an increase of the effective refractive index of the substrate will result in the redshift of the resonant frequency. An accurate evaluation of the refractive index change of the substrate in our case is not straight forward since its local value depends on the local THz electric field in a nonlinear manner.

To exclude the possibility that the resonant frequency shift is caused by changes to the metal antenna itself, we performed the same experiment for an antenna array fabricated on insulating fused silica glass. As expected, no significant shift of the resonant frequency has been observed in that case, even at highest achievable field strengths. As it can be expected in from the Drude model, free carrier generation in the HR Si substrate results in change of refractive index. At the tips of the antenna, the field strength is sufficient for THz-induced field emission of electrons in to the surrounding atmosphere as recently reported [23]. To make sure that the free carriers in the substrate are not mainly from metal through field-induced tunneling of electrons from the gold to substrate or other ways, a thin layer of silica isolator (100 nm) is deposited on high resistivity silicon before antenna array is fabrication on its surface (see Fig. 3.3(a)). The low field resonance frequency of the antenna without the silica isolator is 0.84 THz. It is also observed that the resonance frequencies of the antenna with silica isolator shift to higher frequencies as depicted in Fig. 3.3(b) (blue curves). This is because the effective refractive index that the antenna sees is lower due to low refractive index of silica in comparison to silicon. However, the magnitudes of the resonance frequency shifts measured with and without antenna isolator are comparable which supports that there tunneling of free carriers from the metal antenna to the substrate is not the main source of free carriers in the substrate.

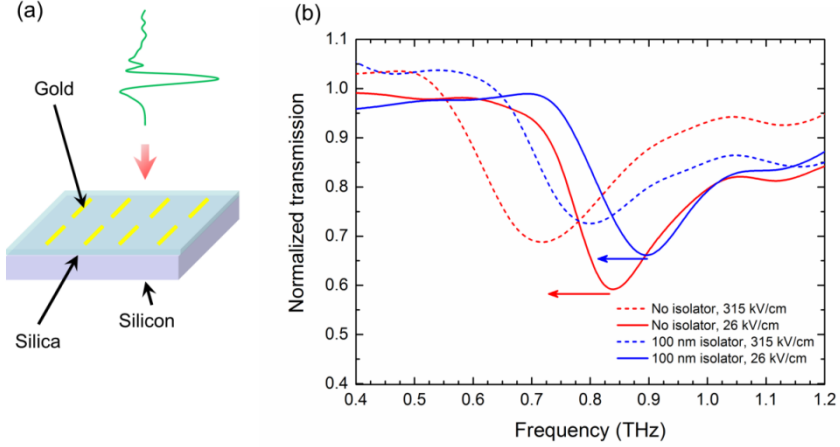


Figure 3.3. (a) Silica isolator to block possible tunneling of free carriers from gold to the HR silicon substrate. (b) Normalized spectral transmission of antenna array fabricated on high resistivity silicon with and without 100 nm silicon isolator. Arrows indicate direction of resonance field at high electric field strength.

The change in resonance frequency by generation of free carriers is reproduced with full-wave simulations with commercial software (CST microwave studio) by modifying the refractive index of HR Si locally in the vicinity of the antenna tips. The change of refractive index is limited to a volume of the region where the peak THz field strength is larger than a certain threshold value E_{th} . To maintain consistency with the measurements, a measured THz transient is used as an input in the simulation and the solver duration is also kept at the same length as the measurement time window (15 ps). In order to keep the simulation tractable it is assumed that the refractive index change is constant if the field strength is greater than the threshold value E_{th} and negligible in the substrate regions with THz electric field smaller than the threshold. A Drude model is used to analyze the dielectric properties of the substrate near antenna tips as a function of carrier density with parameters adopted from Willis *et al.* [88]. Even though it is difficult to determine the local refractive index change, it is still possible to determine

the average refractive index change of the substrate near the antenna tips. Figure 3.4 shows transmission spectra simulated with various refractive index changes that correspond to same shift as measurements from Fig. 3.3. Our simulations show that the average refractive index in the vicinity of the antenna needs to increase by 4 to match the resonant frequency shift measured in the experiments for an input field of 251 kV/cm. The imaginary part of the refractive index also changes in the vicinity of the antenna tips. However, our simulations show that change of the imaginary part of the refractive index only does not result in a shift of the antenna resonance frequency and it is therefore not discussed in detail.

The observed refractive index change of the substrate can be explained by field-induced generation of free carriers. The refractive index of silicon as a function of carrier concentration is calculated using the Drude model with parameters reported by Willis *et al.* [88]. At a frequency of 0.6 THz (the resonance frequency of the antenna), the local carrier concentration is estimated to be more than 10^{17} cm^{-3} in order to reproduce the refractive index change at an incident THz field of 251 kV/cm. This is seven orders of magnitude larger than the intrinsic carrier concentration of the undoped high resistivity silicon substrate ($1.5 \times 10^{10} \text{ cm}^{-3}$ as specified by the supplier). These shows that THz pulses enable switching of the conductivity of silicon on an ultrafast time scales (sub-picosecond).

Comparing Fig. 3.2 and 3.4 we clearly see that the transmission spectra of the antenna array are well reproduced by the simulations. Our measurements show that at high electric field the transmission resonance is slightly broader and the resonance is not as strong as low electric field resonance. This behavior is not observed in the simulations. This is expected in the simulations since a uniform plane wave source is used and an infinite number of antennas experiencing the same field strength. In actual measurements the THz beam extends only over a limited number of antennas

(~9 antennas) which will experience various field strengths depending on their location with respect to the profile of the THz beam. That means the observed shape and strength of the transmission resonance is a cumulative effect of several antennas with different resonance shifts which results in a resonance broadening.

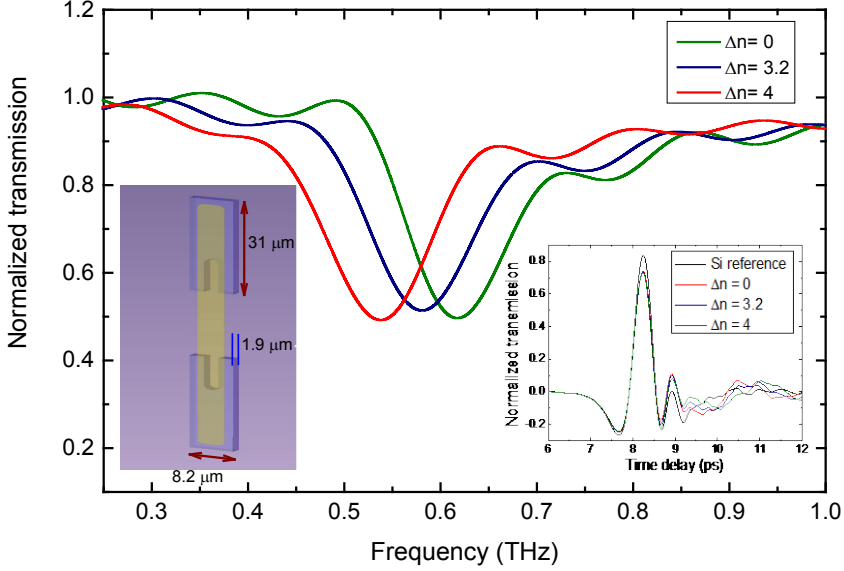


Figure 3.4. Simulated transmission of an antenna array on HR silicon as function of frequency. Δn is the change in refractive index of the substrate region where the peak field strength is higher than the threshold value E_{th} . The inset on the left shows the local substrate region where refractive index is changed by 4.0. The inset on the right shows the corresponding transmitted THz transient calculated inside the silicon substrate.

From the transmission measurements of the antenna arrays, it is found that that the minimal peak electric field of the incident THz wave required to observe measurable frequency shift of the resonance is approximately 19 kV/cm for the front illumination (see Fig. 6). The numerical simulation results show that the antenna with resonant frequency of 0.6 THz enhances the THz field locally by more than 30 times (time domain enhancement)

relative to the input reference field. Thus, the actual local threshold peak electric field strength, E_{th} for resonance frequency shift is estimated to be 570 kV/cm. This threshold is significantly higher than the 200 kV/cm required for impact ionization in silicon with a static field [80]. It is expected that that impact ionization in silicon can still happen in the presence of a THz source with field strength less than 570 kV/cm. However, the number of carriers can be insufficient and limited only to a small region near the antenna tips to cause an appreciable shift in the resonance frequency of the antenna.

3.3 Comparison of front and back THz illuminations

The resonant frequency shift of the antenna array with respect to low THz field strength transmission as a function of incident THz field strength is plotted in Fig. 3.5, both for THz transients illuminating the sample from the antenna side (front illumination) and from the substrate side (back illumination). It is apparent that the resonance frequency shift is larger for back illumination than for front illumination for a given incident field strength. The ratio of the field strengths between front illumination and back illumination that result in the same resonance shift is shown in the right panel of Fig. 3.5. The measured ratio is consistent with our theoretical prediction presented below.

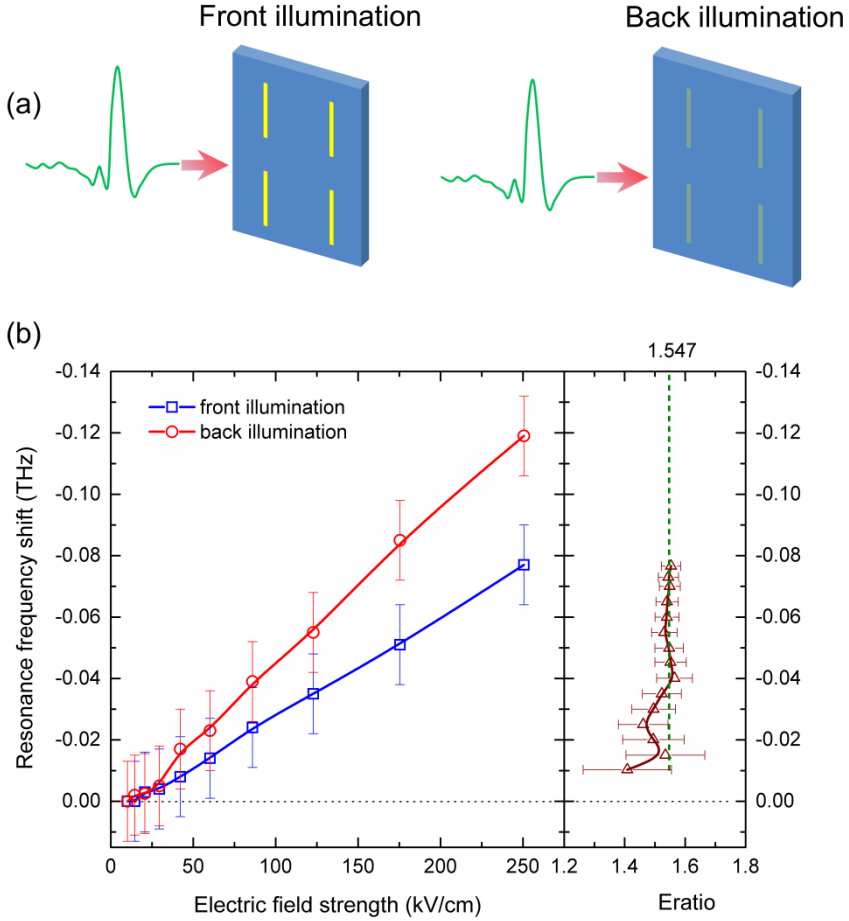


Figure 3.5. (a) THz illumination from antenna side (front illumination) and from the substrate side (back illumination). (b) Measured resonance frequency shift of an antenna array as a function of incident THz field strength for front and back illumination. The ratios of field strength that give same resonance shift are shown as triangles on the right. The curves are included for visual aid. The green dashed line indicates the theoretically expected value for HR Si substrate.

It is clear from Fig. 3.5 that the resonance frequency of the antenna array depends on the direction of illumination of the sample. The increase of the local electric field when illuminated from the substrate side as compared to a direct illumination from the antenna side is somehow counterintuitive.

One could at first glance expect that the Fresnel reflection loss on the air-substrate interface $2/(n_{sub} + 1)$, where n_{sub} is the refractive index of the substrate, would reduce the field enhancement in the case of back illumination. But as it is shown below other factors provide extra enhancement on the substrate-antenna interface which result in an increase of the local electric field. The observed increase is neither a result of etalon interference effects in a substrate with finite thickness (consecutive reflections in the substrate are well separated in time) nor the effect of focusing THz beam into smaller spot inside material with high refractive index (substrate is too thin). In a simple air-dielectric-air configuration electric field on the air side in a close proximity to the surface can be expressed as $E_{air}^{front} = E_i + E_r = E_i + E_i(1 - n_{sub})/(1 + n_{sub})$ (front illumination) and $E_{air}^{back} = E_t = E_i \cdot 4n_{sub}/(1 + n_{sub})^2$ (back illumination) where E_i is the incident electric field, E_r is the reflected electric field, and E_t is the transmitted electric field. On the dielectric side of the interface, $E_{sub}^{front} = E_t = E_i \cdot 2/(1 + n_{sub})$, $E_{sub}^{back} = E_t + E_r = E_i[1 - (1 - n_{sub})/(1 + n_{sub})] \cdot 2/(1 + n_{sub})$ for front and back illuminations respectively. Both equations hold as long as the distance to the surface is much shorter than the wavelength inside considered material. In both cases electric field is higher for back illumination with a field ratio of,

$$\frac{E_{air}^{back}}{E_{air}^{front}} = \frac{E_{sub}^{back}}{E_{sub}^{front}} = \frac{2n_{sub}}{n_{sub} + 1} > 1 \quad (3.2)$$

The presence of metal structures on the substrate complicates the situation somewhat. But consideration of the induced current by the antenna shows that the current in the antenna with back illumination is also enhanced by a factor of $2/(n_{sub} + 1)$ in comparison to the front illumination as described below. The effective surface current \vec{J} on a dielectric-metal interface can be

expressed by $\vec{j} = \vec{n} \times \vec{H}_{||}$ [89]. The current is directly proportional to the magnetic component of the electromagnetic wave parallel to the surface $\vec{H}_{||}$ (the perpendicular component at the metal surface is 0). In the case of a perfect electric conductor, $\vec{H}_{||} = 2H_i$ where H_i is the incident magnetic field. In the dielectric material, $H_i = k_0 \cdot n \cdot E_i$. When the Fresnel reflection loss $2/(1 + n_{sub})$ at the back substrate is included, we directly see that,

$$\frac{J^{back}}{J^{front}} = \frac{2n_{sub}}{1 + n_{sub}}. \quad (3.3)$$

To verify those analytical predictions a numerical frequency domain simulation of the electric field enhancement in the vicinity of the resonant metal antenna tip is performed for various refractive indices of the substrate for the front and back illumination, see Fig. 3.6. It is clear that the simulation result is identical to the theoretical prediction.

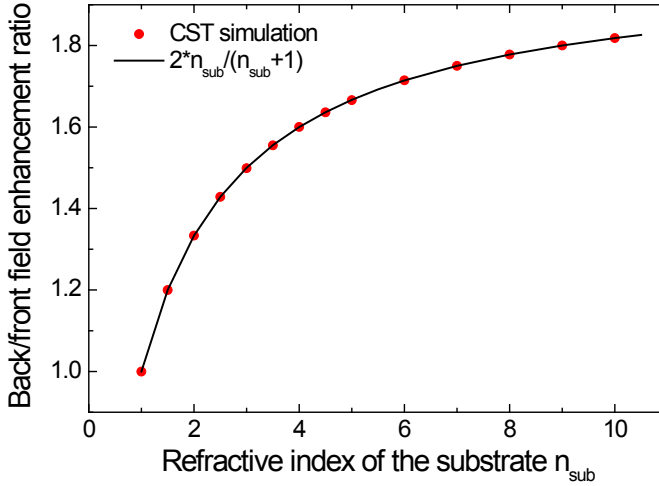


Figure 3.6. Ratio of the field enhancement at a distance of 1 μm from the tip of the antenna for the back and front illumination.

3.4 Temperature-dependent measurements

To find the main physical mechanism for the significant carrier generation, we have measured the temperature-dependent resonance shift for an antenna array of resonance frequency 0.9 THz. First we vary the incident THz field strength on the sample at temperatures of 10 K and 300 K. The result shows that resonance shift is larger for low temperature at all incident field values as shown in fig. 3.7(a). We also measured the resonance shift as a function of temperature in a range from 10 K to 300 K as shown in fig. 3.7(b). The measurement shows that the resonance shift, which indicates the level of generated carriers, decreases slightly with increasing temperature. Thus, the carrier generation rate reduces at higher temperature.

Two physical processes are known to generate high carrier density in semiconductors, namely Zener tunneling and impact ionization. Zener tunneling is a pronounced phenomenon in direct bandgap semiconductors [27], [90]. Since it is a momentum-conserving process, tunneling occurs between equal wave vector points. As silicon is an indirect bandgap material, Zener tunneling is strongly quenched and it must involve scattering processes such as phonon scattering that compensates the Γ and X wave vector-mismatch. In the absence of compensating phonon the barrier potential needs to be lowered significantly as the direct bandgap of silicon is high (> 3.2 eV) which requires extremely high electric field. A phonon-assisted band-to-band tunneling can occur at field strengths much higher than impact ionization threshold [91]. Since the phonon density increases with increasing temperature, the carrier generation rate should be increased at high temperature had Zener tunneling been the dominant mechanism of carrier generation. Moreover, the bandgap of silicon is reduced at high temperature [92] which should additionally increase the tunneling rate. These trends contradict our temperature dependent measurements.

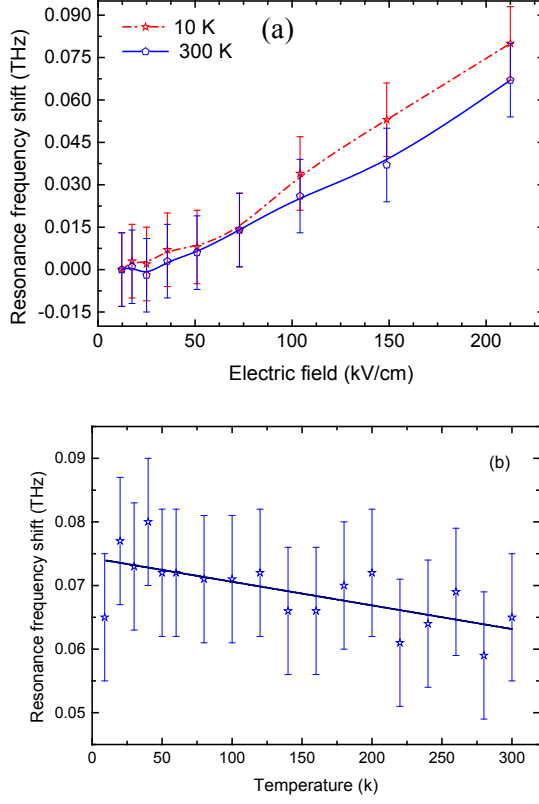


Figure 3.7. (a) Measured resonance frequency shift of an antenna array as a function of incident THz field strength at temperatures of 10 K and 300 K. The blue and the red curves are included for visual aid. (b) The resonance frequency shift of an antenna array as a function of temperature for an incident THz field of 213 kV/cm. The dark blue line is a linear fit.

On the other hand, the decrement of THz-induced carrier generation with increasing temperature is in agreement with earlier reports of the temperature dependence of impact ionization rates in silicon [80], [93]. With rise of temperature, electron-phonon scattering is enhanced and the population of electrons that can reach the impact ionization threshold energy before electron-phonon scattering is reduced. To roughly approximate the carrier generation rates by impact ionization and phonon-assisted Zener tunneling, carrier generation rates at a representative static electric field of

0.6 MV/cm reported earlier are compared. The carrier generation rate is in order of $10^{13} \text{ cm}^{-3}\text{s}^{-1}$ [91] for Zener tunneling and $10^{21} \text{ cm}^{-3}\text{s}^{-1}$ for impact ionization. The carrier generation rate for impact ionization is estimated from impact ionization rate reported by Grant [80] and a drift velocity reported by Ershov *et al.* [93]. Thus, we can identify impact ionization as the main cause of the significant carrier generation that we observe.

Since silicon is an indirect semiconductor, unlike GaAs, impact ionization involves a large momentum change. The need to conserve momentum reduces the probability of impact ionization, which therefore requires a strong electric field. More than 23 impact ionization events are needed to increase the carrier density by seven orders of magnitude as we estimated. A simplified numerical simulation of electron ballistic acceleration in the presence of THz electric field is performed. Our simulation shows that a single electron can acquire sufficient kinetic energy (1.8 eV) [76], [78] to induce impact ionization much faster than electron scattering time (110 fs) [88] and that the duration of THz pulse is more than sufficient to reach 23 impact ionization events.

3.5 Conclusion

In summary, a combination of an intense THz field and an additional field enhancement provided by a metal resonant antenna allows investigation of impact ionization in high resistivity silicon in a multi-MV/cm field strength range. In the presence of an intense THz field, the resonance frequency of the metal antenna array redshifts, which is attributed to a change in the refractive index of the substrate due to the substantial generation of free carriers. Experimental results and simulations show that this extremely nonlinear THz-matter interaction increases carrier density in silicon by over seven orders of magnitude in the presence of an intense THz field near antenna tips.

The resonance shift of the antenna array is measured for several field strengths for THz illuminations from the substrate side and from the antenna side of the sample. The enhancement of the nonlinear process for back illumination in comparison to front illumination is demonstrated which confirms our theoretical prediction. This explanation of a simple observation shows that the orientation of the sample can be highly beneficial for wide ranges of nonlinear phenomena at interfaces between dielectrics. While the antenna resonance shift is shown to be an effective tool to probe impact ionization in silicon, the possibility to modulate the resonance frequency dynamically on ps time scales will have important implications for future ultrafast THz communication systems.

Chapter 4

Time-resolved investigation of impact ionization dynamics in silicon

4.1 Introduction

Carrier multiplication through impact ionization (IMI) plays an important role in efficient photovoltaic nano-materials [94], [95], electroluminescent emitters [96], and highly sensitive photon detectors [97]. IMI in extremely high electric fields is also essential to understand the physics of laser ablation [98]–[100] and high harmonic generation [21], [101], [102]. With semiconductor devices shrinking to nanoscale dimensions, devices with a gate voltage of 1 V experience high electric fields beyond 1 MV/cm. Simultaneously cutoff frequencies of modern electronic devices are being pushed to the terahertz (THz) range [32], [103], [104]. Under such conditions, carrier-initiated impact ionization in conjunction with Zener tunneling and intervalley scattering become critical factors affecting nonequilibrium charge transport beyond the Boltzmann transport equation. Thus, carrier multiplication effects on nonlinear transport need to be fully understood on the femtosecond timescale.

The investigation of carrier multiplication effects in high electric field is particularly important in silicon which is the most important semiconductor in microelectronics and optoelectronics. Previous experimental studies of impact ionization in silicon, which are based on transport measurements with static electric field bias [80], [81], [105], have been performed in highly doped p-n junction devices. High doping is required to allow current measurement in a working p-n junction device.

This limits the possibility to vary the initial carrier density, a parameter that influences impact ionization dynamics significantly.

It is discussed in chapter 3 that extremely strong electric fields can be applied in a noncontact manner by applying THz electric fields. This enables investigation of impact ionization without the need to fabricate a working p-n junction device. By applying an optical pulse along with the THz electric field, it is possible to vary the initial carrier density, allowing the investigation of impact ionization over a wide range of initial densities of carriers.

In this chapter the time-resolved impact ionization dynamics in silicon induced by strong fields in MV/cm is discussed. The impact ionization dynamics is investigated over a wide range of initial densities of carriers by controlled generation of free carriers with an optical pump before arrival of the THz field. Two complementary techniques are used for the investigation of the time-resolved dynamics in a pump-probe scheme. The first experimental investigation involves impact ionization induced by the strong THz field (THz pump) and the initial density of carriers is varied by a pre-arriving optical pump. In this experiment the local carrier generation dynamics is monitored by measuring the reflectivity change of a tightly focused near-infrared (NIR) beam. This technique allows a direct access to the carrier density evolution by simply measuring the NIR reflectivity. The second investigation technique is the THz pump-THz probe experiment where a dynamically delayed weak THz probe is transmitted with the strong THz pump to examine the carrier generation dynamics. This technique is based on monitoring of dielectric property of silicon in the THz spectral range due the generation of free carriers. The change of dielectric constants at THz frequencies is much larger than the corresponding change at NIR frequencies at a given carrier density. This means THz probing is more sensitive than the NIR probing allowing a measurement of lower changes in

the carrier densities. However, the dielectric property change in THz probe is indirectly measured from antenna resonance frequency shift which make the analysis.

The experimental results of the two techniques are presented in two parts. First, the THz/optical pump-optical probe measurement results are described. The experiment is done at Prof. Tanaka's lab at Kyoto University, Japan. A simplified Monte Carlo (MC) simulation is implemented to elaborate the measurement results. The MC simulation clarifies IMI dynamics and the physical processes that influence the dynamics. In the second part the result of THz pump-THz probe measurements are explained. A harmonic oscillator model that accounts the resonance frequency shift is formulated to interpret the carrier generation dynamics from the pump-probe scans.

4.2 THz/optical pump-optical probe measurements

4.2.1 Experimental setup

The schematic of THz/optical pump-optical probe experimental setup is shown in Fig. 4.1(a). An amplified Ti:sapphire laser output (repetition rate 1 kHz, central wavelength 800 nm, pulse duration 100 fs, and pulse energy 4 mJ/pulse) is used as the light source for the intense THz generation by optical rectification in a LiNbO₃ crystal by a tilted-pump-pulse-front scheme [12]. The THz pulse is tightly focused on the sample by using an off-axis parabolic mirror with a 50 mm focal length. However, the maximum THz field in most of the measurements is limited below 500 kV/cm to avoid sample damage. The incident field strength is varied by changing the angle between two crossed wire-grid polarizers.

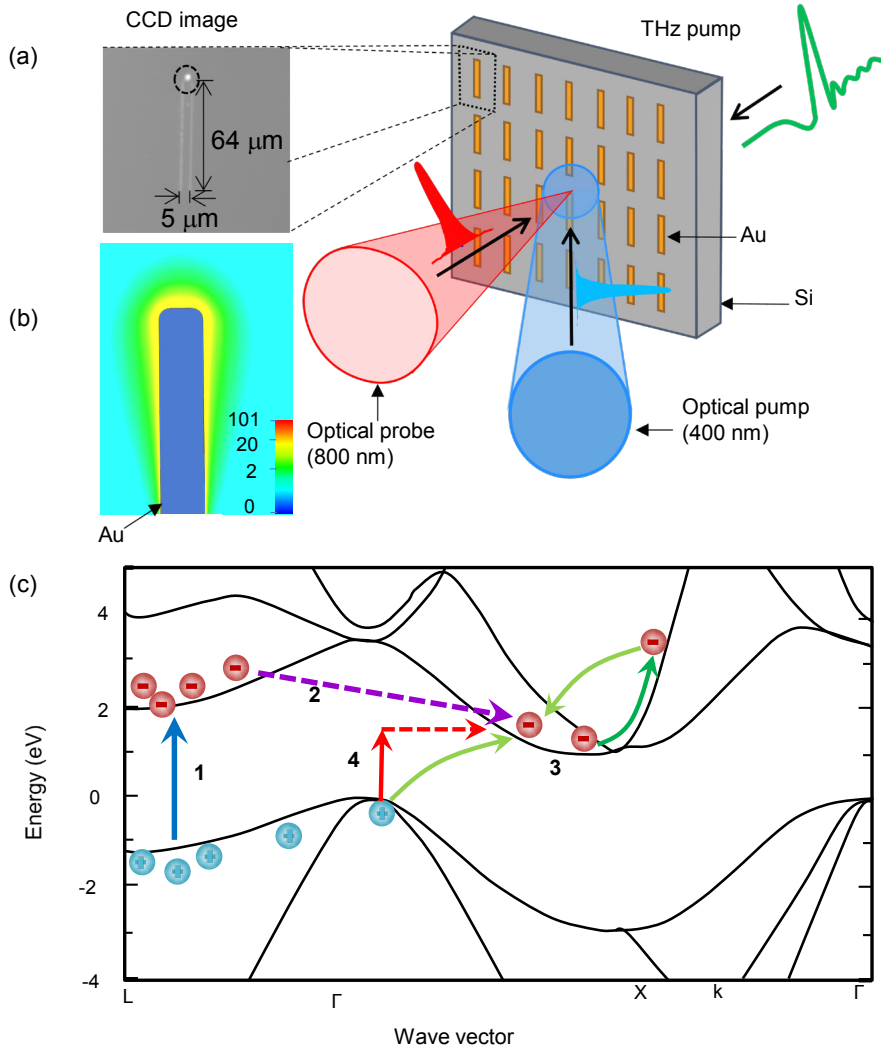


Figure 4.1. (a) A schematic of the pump-probe setup used to investigate the THz-induced impact ionization dynamics in silicon. CCD image of a unit cell of the antenna array with bright probe spot is shown in the inset (dashed circle). (b) Calculated local electric field enhancement profile near the antenna tip. (c) Carrier transitions on Si band structure: (1) interband transitions by optical pump, (2) L-to-X intervalley scattering and (3) carrier multiplication through impact ionization.

The sample is a high resistivity silicon (intrinsic carrier density of $1.5 \times 10^{10} \text{ cm}^{-3}$) where metallic dipole antenna arrays are fabricated on its

surface by the conventional photolithography. The dimensions of the antenna are: length = 64 μm , width = 5 μm , thickness = 0.2 μm and period = 115.3 μm . The resonance frequency of the antenna is 0.75 THz. CCD image of a single antenna is indicated in Fig. 4.1(a). Full-wave electromagnetic wave simulations show that metallic dipole antennas in an array configuration [66] enhances the peak electric field in the vicinity of antenna tips, leading to a maximum peak electric field of 3.6 MV/cm inside silicon at a distance of 1 μm from the metal tip. The simulated local electric field enhancement profile is shown in Fig. 1(b).

The intense THz field is incident from the substrate side of the high resistivity silicon (100) where the antenna arrays are on the opposite surface. THz illumination from the substrate side allows the probe beam to be applied at a normal incidence. Additionally, illumination from the substrate side results in a higher electric field inside silicon as compared to the front illumination as discussed in chapter 3. To monitor the carrier generation dynamics with a controlled initial density of carriers, a near ultraviolet (NUV) pump pulse (400 nm) is used to generate free carriers before the arrival of the THz pulse. The NUV pulse is generated by frequency doubling in a nonlinear beta barium borate (BBO) crystal and is focused on the sample to a diameter of approximately 45 μm at an incident angle of 45°. The large cross-sectional area compared to the probe spot size minimizes the effect of carrier ambipolar diffusion parallel to the sample surface on the probe signal. The temporal evolution of the carrier density is probed quantitatively by the transient reflectivity change of a weak near-infrared (NIR) pulse. The NIR probe is tightly focused on the sample to a diameter of approximately 2 μm using an objective lens. The spatial location of the probe pulse in the vicinity of the metallic antenna is monitored by a CCD camera (See inset of Fig. 4.1(a)). The reflected NIR probe is detected by a photodetector and data averaging is done using a boxcar integrator.

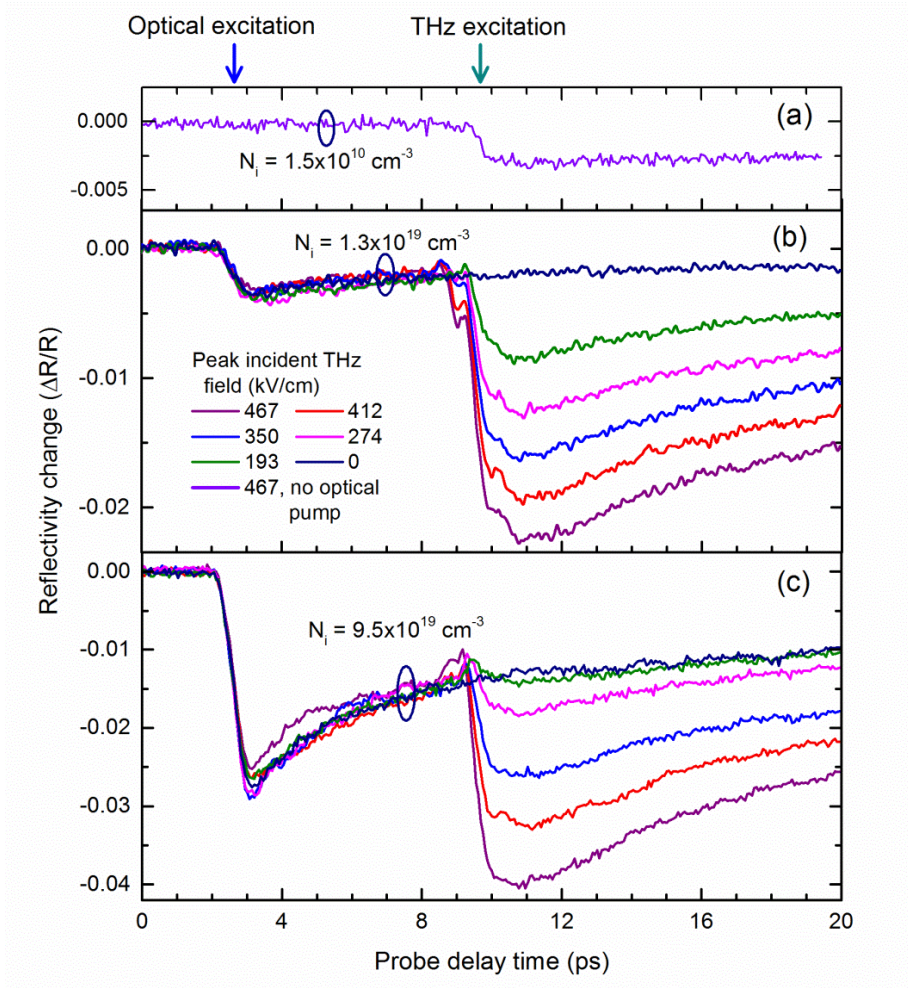


Figure 4.2. NIR reflectivity change with an NUV and THz excitations at various incident field strengths for initial density of carriers of, (a) 1.5×10^{10} , (b) 1.3×10^{19} , and (c) $9.5 \times 10^{19} \text{ cm}^{-3}$. Color-coding of the incident THz field strength is the same in all panels.

Possible transitions of carriers on the band diagram of silicon in the presence of NUV and THz excitations in the respective temporal order are depicted in Fig. 4.1(c). The photon energy of the NUV pump pulse (3.1 eV) is close to the bandgap near the L symmetry point (the smallest direct band gap), so interband transitions (process 1) result in electrons in the L-valley.

Then electrons undergo L-X intervalley scattering (process 2) with a time constant of 180 fs [106]. The electron distribution is thermally equilibrated with the lattice via phonon scattering within less than 2 ps [106]–[108]. The THz electric field is parallel to the [110] direction and accelerates conduction band electrons. Collision of energized electrons with valence band electrons results in new electron-hole pairs (process 3) – impact ionization. Possible phonon-assisted interband transition by the probe pulse is shown as process 4.

4.2.2 Measurement results

The relative NIR reflectivity changes ($\Delta R / R$) for several incident electric fields are shown in Fig. 4.2 for initial carrier densities (N_i) of 1.5×10^{10} , 1.3×10^{19} , and $9.5 \times 10^{19} \text{ cm}^{-3}$. In Fig. 4.2(a) the NUV pump is blocked and the initial carrier density is equal to the intrinsic carrier density of the silicon substrate. In this case, the THz-induced reduction of the NIR refractive index is $\Delta n = 9 \times 10^{-3}$. Nonlinear effects such as free carrier generation, state filling and linear thermal effects can cause a change of the refractive index of silicon. Our estimation based on lattice heating model sets an upper limit on temperature rise by THz-induced heating of 10 K, which would correspond to an increase of reflectivity of 10^{-3} [109]–[111] contrary to the decrease in reflectivity that is observed in the measurements. Thus, the observed reduction in NIR reflectivity is attributed to free carrier generation.

The first decrease in reflectivity near $t = 2.5$ ps in Fig. 2(b) and (c) is due to carrier generation by the NUV pre-pump. The reflectivity drop reduces with probe delay time especially for highest initial carrier density due to carrier diffusion and Auger recombination. The penetration depth of the NUV pump is only about 80 nm in silicon and diffusion of carrier away from the surface reduces carrier density near the surface, subsequently reducing the NIR reflectivity change. The second drop in reflectivity near $t =$

9.5 ps overlaps with the THz pulse and is caused by free carrier generation by the THz pulse.

Considering that free carrier generation is the source of the change of NIR reflectivity, the corresponding change in density of carrier can be calculated by applying the Drude model. The exact relationship between change of reflectivity and carrier density is derived below. The reflectivity and refractive index are related as,

$$R = \left(\frac{n-1}{n+1} \right)^2 \quad (4.1)$$

$$\frac{\partial R}{\partial n} = 4 \frac{n-1}{(n+1)^3} \quad (4.2)$$

Where R is reflectivity and n is real index of refraction. For small changes of index of refraction Δn , the relative change of reflectivity can be written as,

$$\frac{\Delta R}{R} = \frac{\partial R}{\partial n} \frac{\Delta n}{R} = \frac{4\Delta n}{n^2 - 1} \quad (4.3)$$

In the Drude model the dielectric permittivity is given by,

$$\hat{\epsilon}(\omega) = \epsilon_{\infty} - \frac{Ne^2}{m^* \epsilon_o \omega \left(\omega + \frac{i}{\tau} \right)} \quad (4.4)$$

$$\hat{\epsilon}(\omega) = n(\omega)^2 = \left(n_o + \Delta n + i(k_o + \Delta k) \right)^2 \quad (4.5)$$

$$\frac{\partial(n(\omega)^2)}{\partial N} = 2n(\omega) \left(\frac{\partial \Delta n}{\partial N} + i \frac{\partial \Delta k}{\partial N} \right) \quad (4.6)$$

$$\frac{\partial \hat{\epsilon}}{\partial N} = - \frac{e^2}{m^* \epsilon_o \omega \left(\omega + \frac{i}{\tau} \right)} \quad (4.7)$$

$$\Delta n = \frac{\partial n}{\partial N} N = - \frac{Ne^2}{2n m^* \epsilon_o \omega \left(\omega + \frac{i}{\tau} \right)} \quad (4.8)$$

At the NIR probe frequency, it can be assumed that $\omega \gg 1/\tau$ and $\Delta k \ll \Delta n \ll n$ and Eq. 4.8, can be simplified as,

$$\frac{\Delta R}{R} = - \frac{2Ne^2}{n_o m^* \epsilon_o \omega^2} \frac{1}{n_o^2 - 1} \quad (4.9)$$

where N is the charge carrier density, e is the electronic charge, m^* is the effective mass of free charge carriers, ω is the angular frequency, ϵ_∞ is background dielectric constant, ϵ_o is the dielectric permittivity of vacuum, n_o is the refractive index of substrate without excitation or at its intrinsic carrier density. The evolution of the carrier density is evaluated from the reflectivity change using effective optical mass, $m^* = 0.156m_e$ (m_e is the electronic mass), and a refractive index at intrinsic carrier concentration $n_o = 3.68$ [108], [109], [112]. To minimize any coherent nonlinear effects occurring at the overlap between the THz pump pulse and probe pulse, we perform all the carrier density calculations at least 1.5 ps after the THz peak. At this time, the electrons will be thermalized with the lattice and the effect of electron temperature on reflectivity is minimized. In the case of intrinsic initial carrier concentration (Fig. 4.2(a)), a salient drop of reflectivity occurs due to the THz pulse excitation without photo excitation. An Estimation from the change of refractivity shows that carrier density increases by more than eight orders of magnitude.

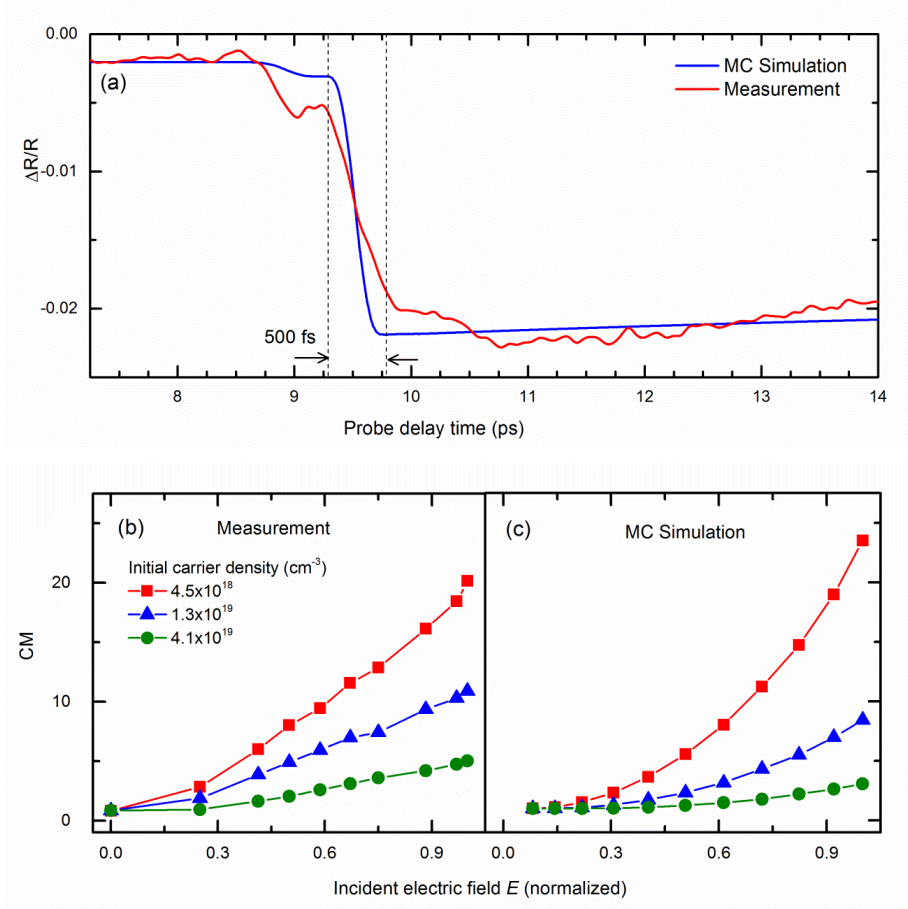


Figure 4.3. (a) Comparison of the dynamics of the reflectivity change between the MC simulation and measurement for $N_i = 1.3 \times 10^{19} \text{ cm}^{-3}$. Carrier multiplication factor as a function of the incident electric field E for several initial densities of carriers, (b) measurement, (c) Monte Carlo simulation. Carrier multiplication factor means the ratio of densities of carriers after and before the THz pulse.

4.2.3 Monte Carlo simulations

To elaborate physical process of the carrier generation mechanism a Monte Carlo (MC) simulation is performed. In the simulation an electron is propagated in a linearly polarized THz field. Since it is not possible to measure the local electric field near the antenna tips, the local THz field strength is used as the only fitting parameter in the simulation. The electric

field strength is adjusted in the simulation such that the ratios between carrier density after and before THz (carrier multiplication factor, CM) in the measurement and simulation fit best. An electron is accelerated in the THz field and the temporal evolution of its energy $\varepsilon_e(t)$ is calculated in steps of 0.1 fs. At every step, the scattering rates of different scattering mechanisms are calculated taking into account the density of free carriers and the electron energy. The scattering rates as a function of electron energy and carrier density are taken from literature. The total scattering rate is given by $\gamma_{tot}(\varepsilon_e, N) = \gamma_{ph}(\varepsilon_e) + \gamma_{eh}(N) + \gamma_{imi}(\varepsilon_e)$, where $\gamma_{ph}(\varepsilon_e)$ is the energy dependent phonon scattering rate [113], $\gamma_{eh}(N)$ is the carrier density-dependent electron-hole scattering rate [111], and $\gamma_{imi}(\varepsilon_e)$ is the electron energy-dependent impact ionization rate [78].

The scattering rates for each mechanism are used to determine the scattering probabilities which in turn determine the scattering event that the electron undergoes. If the electron scatters with a hole, the electron loses its energy and it will have only a thermal energy. The direction of the electron is set to be random after scattering with the hole. Scattering of an electron with a phonon makes the electron move in a random direction. Phonon energy is typically low and it does not reduce the electron energy significantly. So in the simulation electron energy is maintained after scattering with a phonon. If impact ionization happens to be the scattering event, the number of electrons doubles as the process generates new electron and hole.

The density of carriers is dynamically upgraded during the simulation by considering the contributions of Zener tunneling, Auger recombination and impact ionization according to the following equation,

$$N(t) = N(t-dt)\xi(\varepsilon_e, \gamma_{tot}) + (\gamma_{Auger}(N) + \gamma_{Zener}(E_{in}))dt \quad (4.10)$$

where ξ is a stochastic parameter that depends on whether impact ionization happens or not. It has a value of 2 if impact ionization happens and 1 otherwise. γ_{Zener} is the sum of direct and indirect band-to-band tunneling rates [91] and the Auger recombination rate is given by $\gamma_{Auger}(N) = -(C_e + C_h)N^3$ where C_e, C_h are Auger coefficients for $e-e-h$ and $e-h-h$ processes, respectively [114]. In the MC simulation 2128 electrons are simulated and the average of simulated parameter outputs from the simulated electrons is taken as the final value. The number of electrons is good enough to get reproducible output (acceptable convergence is achieved) while not being computationally time consuming.

With the buildup of free carriers generated by impact ionization, electric field screening reduces the local electric field inside the silicon substrate. The macroscopic effect of field screening translates to the modification of dielectric permittivity of the silicon. Thus, the screening effect is considered by dynamically calculating the refractive index and estimating the transmitted electric field into the silicon substrate with the Fresnel law.

The reflectivity dynamics in the MC simulation and the measurement for $N_i = 1.3 \times 10^{19} \text{ cm}^{-3}$ and full THz illumination is shown in Fig. 4.3(a) where it can be seen that carrier generation happens within the sub-picosecond duration of the THz pulse. The dependence of the CM factor on incident field in MC simulations and the measurements for several initial carrier concentrations are depicted in Fig. 4.3(b) and (c). Even though the simulation is simplified that it does not take into account the full band structure of silicon, the field and initial carrier density dependence of CM are reproduced.

4.2.4 Discussion of the impact ionization dynamics

To elaborate the impact ionization dynamics in the conventional platform, the widely used impact ionization coefficient, α which is defined as the number of IMI events per unit length, is calculated. The IMI coefficient is determined as a function of the electric field strength from the CM factor as $\alpha = \ln(\text{CM}) / (v_n \Delta t)$ [80] where v_n is the drift velocity of an electron, and Δt is the duration of the THz induced reflectivity drop. The measured $\log(\alpha)$ vs $1/E_{in}$ is shown in Fig. 4.4(a) along with commonly cited experimental data, obtained by measurement of direct current (DC) amplification in p-n junction devices [80], [81]. Even though the measurement methods and type of excitation are different, the field dependence of IMI in optically doped measurements agrees very well with previous measurements, especially for the highest initial carrier density. The impact ionization region in the p-n junction diodes were highly doped with comparable initial carrier density set by our optical excitations.

The $\log(\alpha)$ vs $1/E_{in}$ is well represented by a linear fit which shows that the exponential model of impact ionization field dependence by Chynoweth [105] is valid for ultrashort electric field pulses in the MV/cm regime. In the model the impact ionization coefficient is expressed as,

$$\alpha = \alpha_{\infty} \exp(-b / E_{in}), \quad (4.11)$$

where α_{∞} and b are constants.

As the initial carrier density decreases, the IMI coefficient increases for a given electric field. In the case of intrinsic initial carrier density, the IMI coefficient of up to $3 \times 10^6 \text{ cm}^{-1}$ is obtained experimentally (purple open circles in Fig. 4.4(a)) that approaches the fundamental Okuto limit imposed only by energy conservation (blue dotted curve Fig. 4.4(a)) [115]. Such a

high IMI coefficient at low initial carrier density is more than one order of magnitude larger than simple extrapolation of previously reported values [80], [81]. At the intrinsic initial carrier density, only a single electron is on average found in the region of the high field of the antenna tip in a volume of $7 \times 3 \times 2 \text{ } \mu\text{m}^3$. Thus, based on the observed reflectivity change (Fig. 4.2(a)), a population of 9.3×10^8 free electrons is generated within a few hundred fs at the highest field of our experiments, corresponding to an ultrafast cascade of 29 IMI events.

Figure 4.4(b) shows the IMI coefficient dependence on the initial carrier density at a fixed THz field (full THz illumination). To understand the physical mechanism of the initial carrier dependence a MC simulation is performed by selectively switching different physical processes that influence the IMI. In a simplistic case where only electron-phonon scattering is included (without Auger recombination, electron-hole scattering and field screening), the IMI coefficient is nearly independent of initial carrier density (orange curve in Fig. 4.4(b)). Inclusion of Auger recombination reduces the ionization coefficient (green curve) by more than an order of magnitude at the highest initial carrier density considered here. In these conditions (the final density of carriers is on order of 10^{20} cm^{-3}) Auger recombination competes with impact ionization by depleting carriers effectively [116]. Further reduction of the IMI coefficient is seen by including the electron-hole scattering (purple curve in Fig. 4.4(b)) which reduces the energy gain of the electrons in the conduction band. Contribution of electron-hole scattering to impact ionization is more important at high initial carrier density where the e-h scattering rate is higher [111]. In the case of low initial carrier densities, *e-h* scattering limits the impact ionization process only after a high carrier densities have been generated, and consequently, its contribution is smaller. Finally, the inclusion of field screening by free carriers (local reduction of the incident electric field due to an increase in the dielectric

constant at THz frequencies) in the MC simulation (blue curve in Fig. 4.4(b)) reproduces the measured impact ionization coefficient across more than 9 decades of initial densities of carriers.

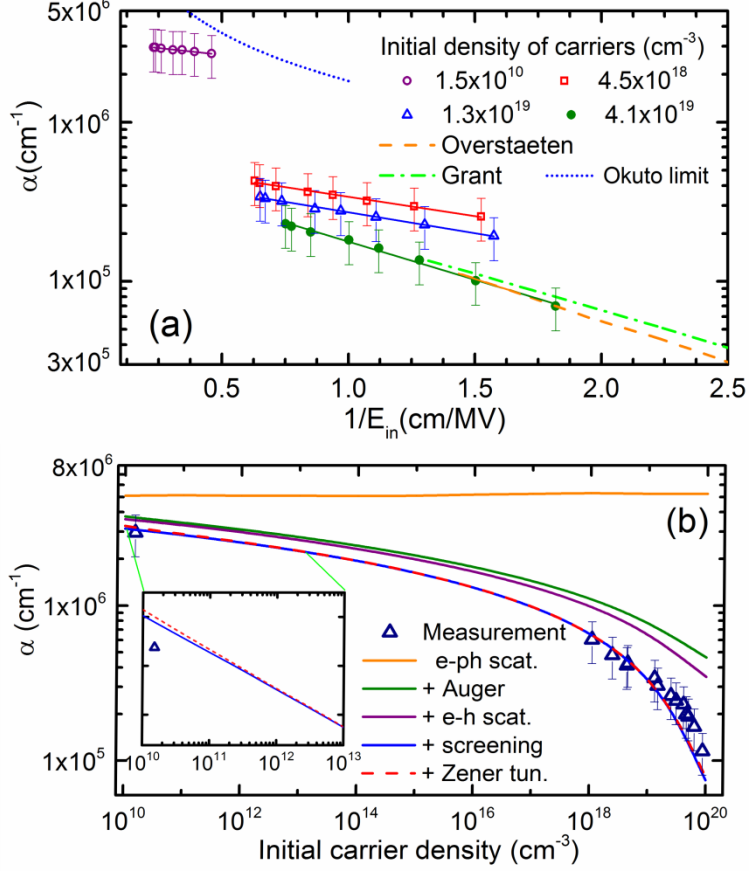


Figure 4.4. (a) Impact ionization coefficient as a function of inverse of electric field E_{in} with linear fits (measurement); experimental results from literature [80], [81] are included as dotted, dashed, and dash-dot lines. (b) Impact ionization coefficient as a function of initial carrier density from measurements (triangle symbols) and MC simulations (lines).

Comparison of impact ionization coefficients with and without Zener tunneling included in the modelling shows that in most cases the

contribution of Zener tunneling is too small to affect the IMI coefficient. The large direct band gap of silicon (~ 3.4 eV at Γ point) requires significantly strong electric field to lower the potential energy sufficiently for the valence band electrons to tunnel into the conduction band [74] and the tunneling rate is much smaller than the impact ionization rate. Only in the case of low initial carrier densities where field screening is less efficient, we found a slight difference in the IMI coefficient (inset of Fig. 4.4(b)).

4.2.5 Energy loss mechanisms in high electric fields

The application of short electric field pulses enables investigation of impact ionization at very high electric fields in MV/cm which cannot be achieved with a static electric field of due to an avalanche breakdown and permanent sample damage. To further illustrate the effect of the high electric fields on the sample, the distribution of the deposited energy from the electric field to a heat transferred to the lattice and an energy going to impact ionization is calculated based on the MC simulations. In the simulations the input electric field is a square pulse of 500 fs width which is a simplified representation of the THz pulse. To estimate the maximum heat transferred to the lattice and subsequent rise in temperature, the number of phonon scattering events are counted and multiplied with the highest phonon energy of silicon ~ 60 meV [117]). On the other hand the energy lost to impact ionization is estimated from the number of new electrons generated and the bandgap energy of silicon.

The fractions of the total energy lost to impact ionization and lattice heating as a function of electric field strength are depicted in Fig. 4.5(a). At low electric fields the energy gained by free electrons and holes is dissipated to the lattice and the quantity of carriers that reach the impact ionization energy is less. As the electric field increases, the energy of carriers is also lost to the impact ionization process that increases the number of free

carriers. This, in turn, increases THz absorption and heat transfer to the lattice. As the field increases, the fraction of energy flow to impact ionization increases and becomes the dominant energy loss path. The increase in temperature as a function of electric field for silicon with intrinsic initial carrier density is shown in Fig. 4.5(b). For THz pulse excitation with peak electric field of several MV/cm a sub-10 K increase in temperature is estimated which does not have any damaging effect on the silicon sample. On the other hand, if the pulse width is increased by a factor of 1000 (to 0.5 ns), the temperature will increase above the silicon melting point (1685 K). This clearly shows that investigation of impact ionization by static or low-frequency electric fields in the MV/cm range is not possible, simply due to permanent material damage.

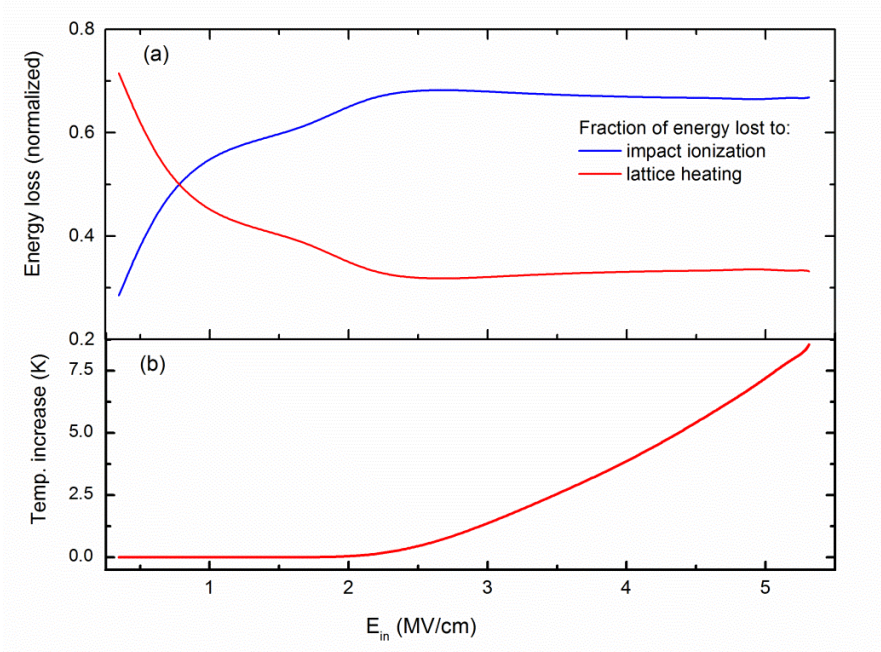


Figure 4.5. (a) Fraction of energy transferred to lattice and energy lost by impact ionization. (b) The change of temperature as a function of electric field E_{in} with intrinsic initial carrier density.

4.2.6 Optical probing of the nearfield profile of metallic antennas

Metallic dipole antennas fabricated on silicon surface are used to enhance the THz electric field in the measurements discussed so far. Antennas and metamaterials are applied over a broad range of applications such as single molecule spectroscopy, nonlinear optics, near field microscopy due to their resonant field localization and enhancement capabilities. It has been challenging to directly measure the nearfield profile of these structures. Mostly the understanding of the nearfield is based on the simulations with experimental verifications only in the far field. The far-field measurements do not often carry the full near-field information such as influence of evanescent waves and spatial distribution of surface charges [118]. An experimental measurement technique is essential to validate the theoretical investigations.

Experimental techniques for direct nearfield profiling of THz radiations has been demonstrated by fabricating antennas on electro-optic active substrates [64], [118]. However, the field enhancement and nearfield profile depends on substrate material and antenna properties may not be translated to antennas made on electro-optically inactive substrates. Thus, measuring the field profile directly on commonly used material for THz devices (silicon) and other electro-optically inactive materials enables a noninvasive testing platform for THz devices. In this section the potential of the THz/optical pump-optical probe experimental technique to probe the field profile is demonstrated. The tightly focused NIR probe allows quantitative evaluation of the dynamics of the free carrier density that can be translated into the local field profile of THz antennas and metamaterials. In other words, the free carrier dynamics carries the nearfield profile information of these structures.

To demonstrate nearfield probing capability of the optical/THz pump-

optical probe scheme, a tightly focused NIR probe is scanned spatially near the tip of the metallic dipole antenna and the change of reflectivity is measured. The tight focusing of the NIR beam allows local field profiling in a spatial resolution much smaller than the wavelength of the THz pulse. To obtain a significant change of reflectivity, the region of the sample near the antenna tip is illuminated with the optical pump before the arrival of the THz pulse. Thus, the initial carrier density is set to be approximately $1 \times 10^{19} \text{ cm}^{-3}$.

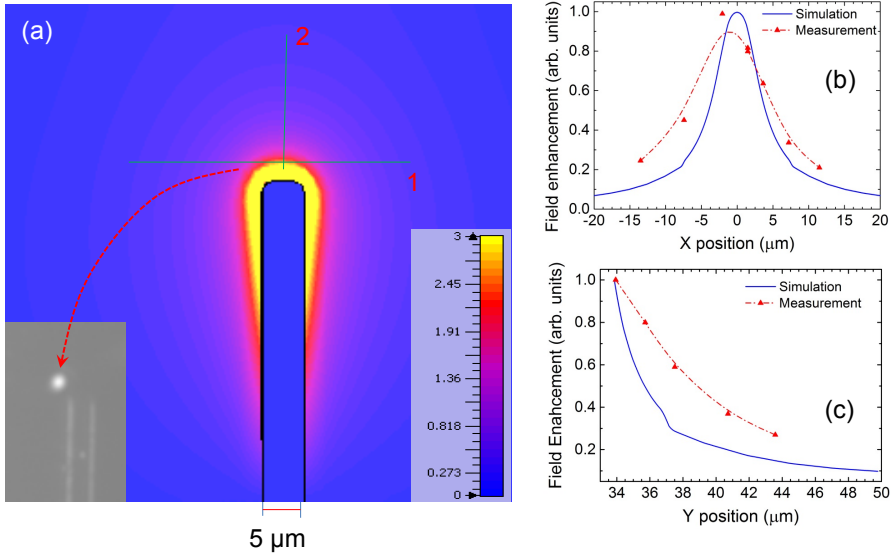


Figure 4.6 (a) The near-field enhancement by the dipole antenna calculated by full-wave electromagnetic wave simulation. The inset shows CCD image of the antenna tip with a probe beam (bright spot). (b) Normalized field enhancement from measurement and simulation along a horizontal line (line 1 in (a)), and (c) along a vertical line (line 2 in (b)) in the vicinity of the metallic antenna.

In Fig. 4.6 the normalized field enhancement obtained by the optical/pump-optical probe experiment is compared with that of the simulations. The measurements are done along the horizontal and vertical lines (1 and 2 respectively) overlaid on the simulated map of the field profile in Fig. 4.6(a). The horizontal line is 2.3 μm away from the antenna tip. As

shown in Fig. 4.6(b, c) the simulation and measurement results agree reasonably even though we do not consider the spatial and temporal dynamic changes in the dielectric property as carrier density changes by IMI in the simulation. The differences could be attributed to the finite size of the probe beam (approximately 2 μm) which can be improved by reducing the probe beam size with better imaging. It is to be noted that the field enhancement changes significantly the region close to the antenna tips and probe beam dimension is critical in the precise determination of field profile. In addition minor differences of shape and features of the antennas between modelled antennas and real antennas are expected to affect the nearfield significantly.

4.2.7 Conclusion

In conclusion, we have shown that the optical/THz pump-optical probe optical setup is a powerful technique to investigate IMI dynamics in silicon over a wide range of initial carrier densities and in a multi-MV/cm field regime. It is demonstrated that the Chynoweth impact ionization model is valid in an applied electric field pulses in MV/cm. It is shown experimentally and by Monte Carlo simulations that the carrier multiplication process depends strongly on the initial carrier density. In the limit of low initial carrier densities ($1.5 \times 10^{10} \text{ cm}^{-3}$) the impact ionization coefficient is an order of magnitude larger than previous reports, and approaches the fundamental Okuto limit imposed by energy conservation. In this limit, with only a single electron initially present within the experimental volume, multiplication to more than 10^8 electrons within a few hundred fs is demonstrated. Consequently, by controlling the presence of that single electron the complete carrier multiplication process can be switched on and off. Those results will have a potential for single electron nano-electronics and macro-scale electronics operating at ultrahigh speeds. Finally, the optical/THz pump-optical probe setting demonstrates

quantitative evaluation of the local field profile of an antenna which can be optimized to be a non-destructive testing tool to characterize antennas and metamaterials fabricated on silicon and other semiconductors.

4.3 THz pump-THz probe measurements

4.3.1 Antenna resonance frequency shift

In chapter 3 it has been discussed that the generation of enormous density of free carriers in silicon near the tip of a metallic dipole antenna results in a dynamic shift of its resonance frequency. As shown in Fig. 4.7(a) the local electric field is enhanced near the metal antenna tip. The generation of free carriers near the tips alters the dielectric constant of the substrate in the vicinity of the antenna tip, consequently changing the resonance frequency of the dipole antenna. Figure 4.7(b) shows a resonance shift of metallic dipole antenna measured with a standard THz-TDS. The antenna has a resonance frequency of 0.75 THz at low power THz illuminations. An incident field of approximately 270 kV/cm reduces the resonance frequency by 130 GHz. To measure the timeline at which the resonance frequency shift happens, a THz pump-THz probe measurement is conducted. The experimental details of the setup are described in detail in chapter 2. The dynamics of the shift of the resonance frequency grants access to the time-resolved dynamics of free carrier density.

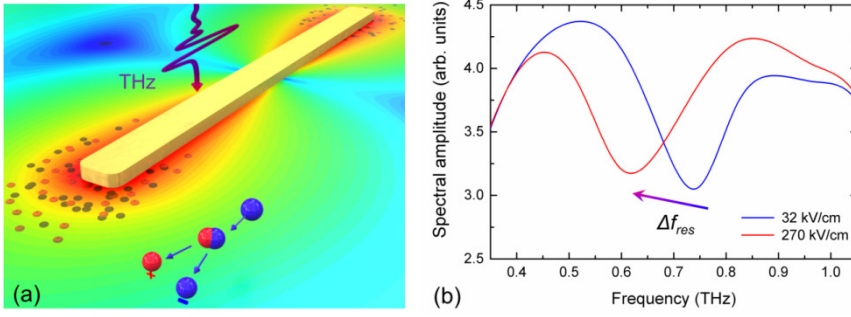


Figure 4.7. (a) Schematic diagram of the impact ionization process: an enhanced local field is induced near the antenna tips under a strong THz field illumination. Impact ionization generates enormous density of free carriers in the high field regions. (b) A resonance frequency of a dipole antenna under the high power and attenuated THz illuminations. In the low power illumination the resonance frequency of the antenna is 0.75 THz.

4.3.2 Modelling of the nonlinear frequency shift of the antenna

In a THz pump-THz probe experiment, the weak probe pulse which is dynamically delayed, is transmitted with the pump pulse. By measuring the resonance frequency shift of the probe pulse as a function of the pump-probe delay, the evolution of resonance frequency shift and free carriers can be obtained. The impact ionization process is faster than THz pulse duration which complicates the analysis of the pump-probe measurements. Thus, a model is required to interpret the pump-probe transmission measurements and extract the evolution of the carrier density. Consequently, the metallic dipole antenna is modelled in a simplified manner by a harmonic oscillator with a time-dependent resonance frequency which depends on carrier density of the substrate. The harmonic oscillator with a time-dependent resonance frequency is written as,

$$\frac{\partial^2 P(t)}{\partial t^2} + \gamma \frac{\partial P(t)}{\partial t} + \omega(t)^2 P(t) = \alpha^2 E(t), \quad (4.12)$$

where $P(t)$ is the polarization field that mimics the local electric field profile near the antenna tip, $E(t)$ is the incident electric field which drives the oscillation, $\omega(t)$ is the resonance frequency of the harmonic oscillator, α^2 is a coupling parameter to the electric field that influences the magnitude of the induced polarization field and γ is the decaying rate of the induced polarization field.

For a given carrier concentration, the dielectric permittivity of a conductive medium in the Drude model is given by,

$$\tilde{\epsilon}(\omega) = \epsilon_\infty - \frac{\omega_p^2}{\omega^2 + i\omega / \tau_s}, \quad (4.13)$$

where $\omega_p = Ne^2/\epsilon_0 m^*$ is the plasma frequency, τ_s is the momentum relaxation time, and N is density of free electrons. The complex refractive index is the square root of the permittivity. Thus, the carrier concentration in the substrate determines its index of refraction. As shown in Fig. 4.8 the functional dependence of the refractive index is strongly influenced by the specific frequency. This means that in a situation where the carrier density changes rapidly in time, the response of the resonance can vary drastically. In the example above, the carrier concentration dependence of the refractive index at the original resonance frequency of 0.62 THz is rather weaker than that of frequency of 0.2 THz. At a lower frequency (0.2 THz) the dependence of carrier concentration on the refractive index is much stronger and refractive index increases monotonously with increase in carrier concentration. This frequency dependence of the refractive index change due to impact ionization is thus important to incorporate in the modelling of the dynamics of the ultrafast resonance shift.

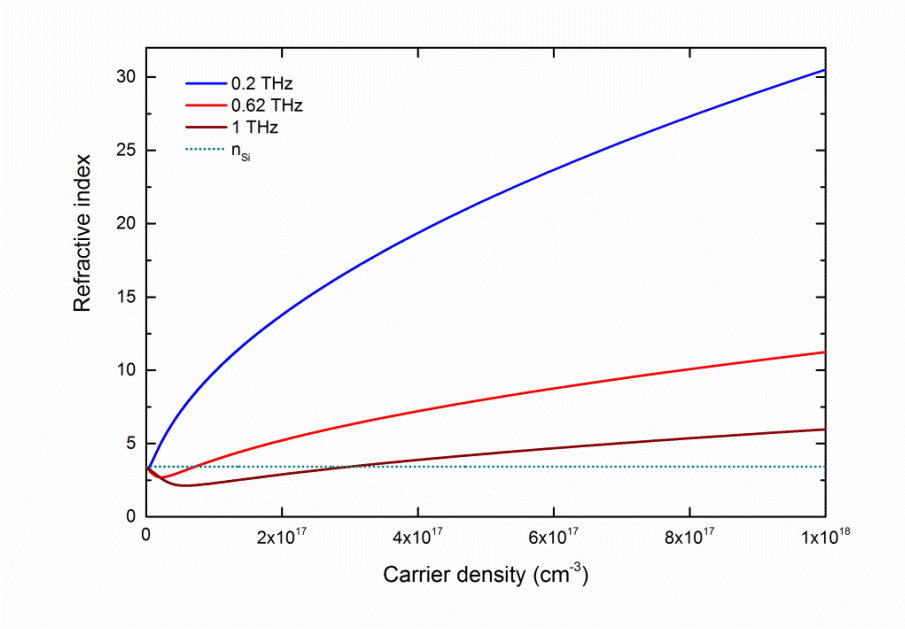


Figure 4.8. Index of refraction at selected frequencies as function of carrier concentration calculated based on Drude model with a carrier scattering time of 200 fs and effective mass of free electrons of $0.2m_e$.

The free electron generation rate can be written by a rate equation,

$$\frac{dN}{dt} = \dot{N} = -\frac{N}{\tau_{rec}} + R_{ii}N, \quad (4.14)$$

where R_{ii} is the field-dependent carrier generation rate per unit time (impact ionization rate), and τ_{rec} is free carrier depletion rate due to either band-to-band carrier recombination or carrier trapping. The impact ionization rate is related to the impact ionization coefficient (α_N) defined in Eq. 4.11 by, $R_{ii} = \alpha_N v_N$, where v_N is the drift velocity of an electron. It is shown experimentally that Chynoweth formula of impact ionization (Eq. 11) describes the field dependence of impact ionization by a THz field in a

strong field regime. For the estimation of the carrier generation rate by IMI, the instantaneous local electric field inside the silicon substrate is estimated from the contributions of the incident THz field and the polarization field such that $E_{loc}(t) = E_{THz}(t) - P(t) / \epsilon_0$. As the carrier density increases in time, field screening by the generated free carriers reduces the electric field strength inside the silicon, consequently, influencing impact ionization rate. To account the field screening effect the index of refraction of the silicon substrate is dynamically calculated and the local electric field is adjusted based on Fresnel reflection from the surface of the silicon substrate.

The resonance frequency, ω , of the antenna depends on the index of refraction, n , and thus the permittivity, ϵ . The permittivity is a nontrivial function of carrier concentration, N , and frequency, ω , and therefore we need to establish the exact functional relation between these parameters. Applying chain rule, the partial derivative of the frequency can be written as

$$\begin{aligned} \frac{\partial \omega}{\partial t} &= \frac{\partial \omega}{\partial n} \cdot \frac{\partial n}{\partial t} = \frac{\partial \omega}{\partial n} \cdot \frac{\partial n}{\partial \epsilon} \cdot \frac{\partial \epsilon}{\partial t} \\ &= \frac{\partial \omega}{\partial n} \cdot \frac{\partial n}{\partial \epsilon} \left(\frac{\partial \epsilon}{\partial N} \cdot \frac{\partial N}{\partial t} + \frac{\partial \epsilon}{\partial \omega} \cdot \frac{\partial \omega}{\partial t} \right). \end{aligned} \quad (4.15)$$

$$\begin{aligned} \frac{\partial \omega}{\partial t} &= \frac{\partial N}{\partial t} \cdot F(N, \omega) \\ \text{where } F(N, \omega) &= \left(\frac{\frac{\partial \omega}{\partial n} \cdot \frac{\partial n}{\partial \epsilon} \cdot \frac{\partial \epsilon}{\partial N}}{1 - \frac{\partial \omega}{\partial n} \cdot \frac{\partial n}{\partial \epsilon} \cdot \frac{\partial \epsilon}{\partial \omega}} \right). \end{aligned} \quad (4.16)$$

The partial derivatives of $F(N, \omega)$ are defined from the Drude model. $\frac{\partial \omega}{\partial n}$ is defined from the resonance property of the dipole antenna. The intrinsic resonance frequency of the dipole antenna in the radio and microwave frequencies can be estimated from $\omega = \pi c / (n_{eff} L)$ where c is the speed of

light in vacuum, L is the physical length of the antenna and n_{eff} is the effective refractive index of the surrounding medium [119] and this relationship also holds in the THz spectral frequency [63], [64]. The effective refractive index can be written in terms of n (the refractive index of the substrate where impact ionization happens) $n_{eff} = n_{eff,o}(1 + k_N(n - n_o)/n_o)$ where k_N is a geometrical factor that accommodates the fact that refractive index changes only near the antenna tips, $n_{eff,o}$ is effective index of refraction before the THz pump, and n_o is the refractive index of silicon before THz pump.

The various partial derivatives are summarized as,

$$\begin{aligned}
\frac{\partial \omega}{\partial n} &= \frac{-k_N \omega}{n_o (1 + k_N (n[\varepsilon[N, \omega]] - n_o) / n_o)}, \\
\frac{\partial n}{\partial \varepsilon} &= \frac{1}{2} \varepsilon[N, \omega]^{-1/2}, \\
\frac{\partial \varepsilon}{\partial N} &= -\frac{e^2}{\varepsilon_0 m} \frac{1}{\omega^2 + i\omega\gamma} = \frac{\varepsilon[N, \omega] - \varepsilon_\infty}{N}, \\
\frac{\partial \varepsilon}{\partial \omega} &= \frac{Ne^2}{\varepsilon_0 m} \frac{2\omega + i\gamma}{(\omega^2 + i\omega\gamma)^2} = -(\varepsilon[N, \omega] - \varepsilon_\infty) \frac{2\omega + i\gamma}{\omega^2 + i\omega\gamma}.
\end{aligned} \tag{4.17}$$

The harmonic oscillator model is solved using the partial derivatives with input electric field consisting of the pump and probe THz pulses in time delay arrangements that mimic the experimental conditions.

4.3.3 Isolating the nonlinear signal in the sample

In the THz pump-THz probe experiment a strong THz pulse, $E_{pump}(t)$ is used to induce the nonlinear carrier multiplication in the silicon substrate and a variably delayed probe pulse, $E_{probe}(t - \tau_{pp})$ co-propagates with the pump to probe the time-resolved evolution of carrier density. τ_{pp} is the time delay between the pump and probe pulses. To examine the nonlinear transmission induced by the THz pump, probe pulse transmission in the presence of the THz pump at full strength ($E_{probe}^{HP}(t - \tau_{pp})$) is compared

with the THz probe transmission in the presence of an attenuated pump pulse ($E_{probe}^{LP}(t - \tau_{pp})$). The measurement of probe pulse in both cases is conducted at various pump-probe delay times. Six 525 μm – thick high resistivity silicon wafers (each having field transmission of, $t_{Si} = 4n_{Si} / (n_{Si} + 1)^2 = 0.7$), where n_{Si} is the refractive index of silicon at THz frequencies, are placed in the collimated section of the THz beam path before the sample (see Fig. 4.9 (a)) to attenuate the THz pump. The wafers are relocated to the THz beam path after the sample for the high power pump illumination. While the silicon wafers attenuate the pump, they do so to the probe pulse as well. However, no difference in transmission is measured between full probe pulse and attenuated probe pulse if the pump is blocked which indicates that the probe doesn't induce measurable nonlinear transmission.

To resolve the evolution of the resonance frequency shift and carrier density from the measurements, a combination of pump and probe functions that resemble the corresponding measured pump and probe pulses are used as an input to solve the differential equations. Schematic diagram of the implementation of the modulation scheme to reproduce the experimental settings is shown in Fig. 4.9(b). In the case of the high power THz pump, strong pump pulse with and without the probe is fed to the differential equation. The difference between the responses to the pump with probe and without probe gives the probe response. In the presence of the strong THz pump, free carriers are generated and antenna resonance frequency changes accordingly. These changes affect the probe pulse transmission, *i.e.* the probe pulse carries information about nonlinear signal induced by the pump. Similarly combination of pump and probe pulses attenuated to the same extent as in the measurements is feed to the system of differential equations, and the probe response in low pump is evaluated. Finally for comparison of probe responses in high power and low power pumps, the corresponding

probe responses in the high power pump are attenuated by the same factor. The simulation is conducted for various pump-probe delay times as in experiments to obtain a 2D pump-probe scan.

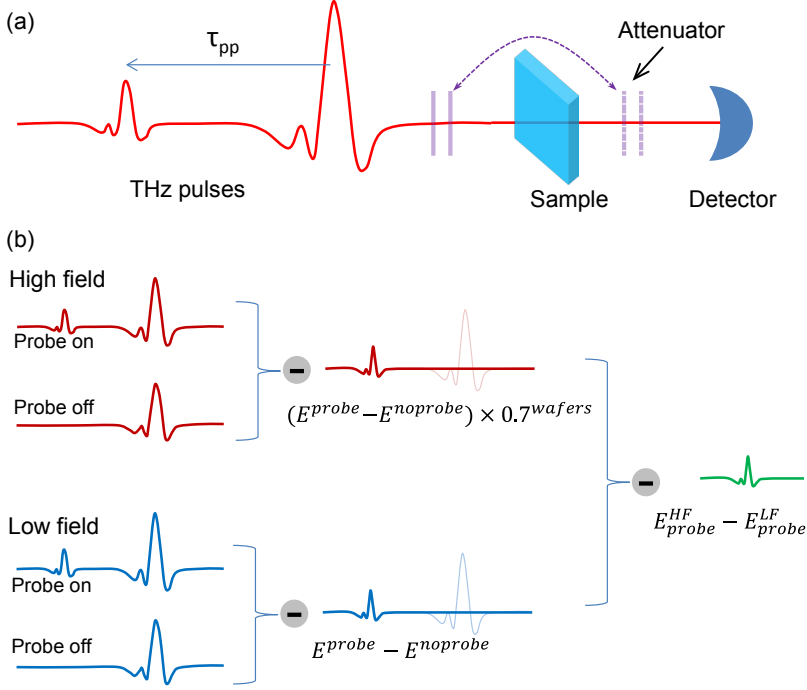


Figure 4.9. (a) Simplified THz pump-THz probe schematic for an experimental investigation of the time-resolved THz-induced nonlinear transmission. Attenuators are relocated before and after the sample for low and high power pump respectively. (b) Numerical modulation scheme for the reproduction of experimental conditions of pump-probe transmission measurements.

4.3.4 Results of the pump-probe measurements and simulations

Figure 4.10 shows the measured and simulated differences between transmitted probe pulses with the high power pump and the low power pump ($E_{probe}^{nonlinear}(t - \tau_{pp}) = E_{probe}^{HP}(t - \tau_{pp}) - E_{probe}^{LP}(t - \tau_{pp})$). The

sample is high resistivity silicon on which dipole antenna array with a low field resonance frequency of 0.62 THz. To confirm that the nonlinear signal is induced in the sample by the THz pump, the experiment is also repeated without sample (air reference). The resulting scan is shown in the inset of Fig. 4.10(a). In this case, we do not observe a nonlinear transmission that resembles the measurements of the sample. Only noise near the temporal overlap between the pump and probe is observed that is caused by nonlinear interactions at the THz generation and detection crystals. More details are described in chapter 2.

The strong red and blue color regions in the 2D map (see fig. 4.10) which does not appear in the air reference scan (see inset) manifest the nonlinear signal ($E_{probe}^{nonlinear}(t - \tau_{pp})$) induced in the sample. Qualitative comparisons of the nonlinear signals of the measurements and simulation clearly show that the simulation reproduced measurement results. This indicates that our model describes the impact ionization dynamics very well. The nonlinear signal is a result of modification of local substrate property near the antenna tip which is a very small section of THz beam spot size. The change is also limited in depth to only few μm 's. As a result probe-peak transmission is not affected significantly by the pump pulse. Consequently, we do not see a nonlinear signal at probe peak (probe delay = 0 ps) even though the pump pulse precedes it. However, the resonance frequency of the metallic antenna is modified by the strong pump pulse. In this case the trailing parts of the probe pulse in high power THz pump experiences phase modifications with respect to the probe pulse in an attenuated pump pulse as a result of the resonance frequency shift which translates into nonzero amplitude difference of the trailing parts of the transmitted probe pulse. This is manifested in the horizontal nonzero difference signals on the pump-probe scan in the positive pump-probe delay times.

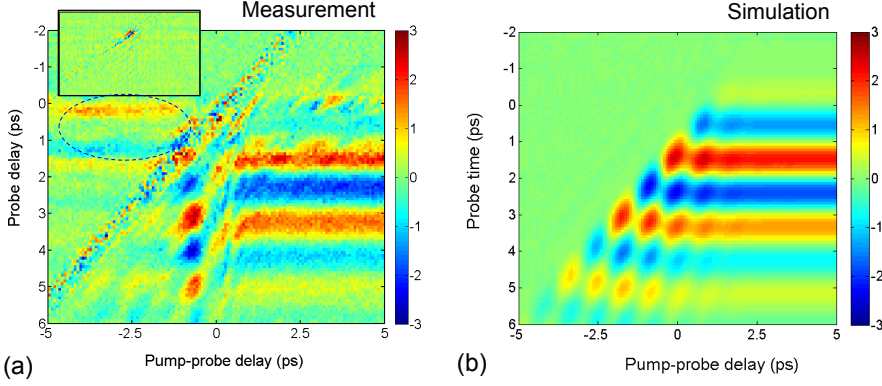


Figure 4.10. Nonlinear signal – difference between the transmitted probe pulse in a high power pump pulse and an attenuated pump pulse ($E_{probe}^{nonlinear}(t - \tau_{pp}) = E_{probe}^{HP}(t - \tau_{pp}) - E_{probe}^{LP}(t - \tau_{pp})$), (a) measurement and (b) simulation. For low power pump, attenuation is achieved by placing 6 silicon wafers in the THz beam path. The inset in (a) shows pump-probe scans with air reference.

The strong nonlinear signal near the pump-probe delay time of -0.65 ps in the measurement is associated with the nonlinear coupling between the pump and the probe in the THz generation crystal. This nonlinear signal is located at the temporal overlap of the peak of the probe pulse and the first negative peak of the pump pulse. In this case we observe a significant enhancement of the individual probe pulses both in low and high power pump conditions. This results in a stronger difference signal. When the probe-pump delay time is close to zero, the probe pulse is observed to have a phase change. For example, the probe peak changes from negative value before zero to a positive value after zero. The nonlinear interaction between the pump and the probe in the crystal is very strong at the temporal overlap between the pump and the probe. It is observed in this case that the nonlinear signal induced in the sample is obscured in the measurement. The signal in the region encircled by the blue dashed line in 4.10 (a) is due the fluctuations in the THz generation over an extended time. It is to be noted that a single pump-probe scan

takes several hours which means that the measurement starting time of the low power and high power scans are separated by several hours (12 hours in this measurement).

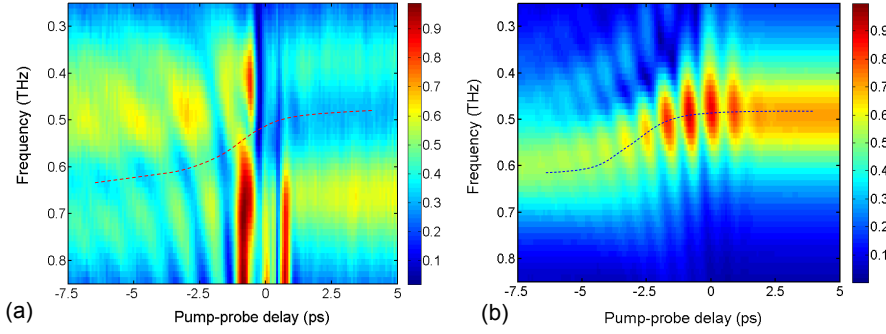


Figure 4.11. Spectral amplitude of the probe pulse as a function of pump-probe delay time in the presence of a high power THz pump as a function of pump-probe delay, (a) measurement, (b) simulation. Dipole antenna response has a dip in transmission at resonance frequency. The harmonic oscillator model has peak response at the resonance frequency and the evolution of the red region in the plots show evolution of resonance frequency. The dashed lines are free hand sketches to showing the evolution of the resonance frequency shift.

To analyze the time-resolved resonance frequency shift, the Fourier transforms of the transmitted probe pulses in the high power and the low THz pumps are calculated. Fig. 4.11(a) shows the Fourier transforms of probe pulses in the high power condition as a function of pump-probe delay time. The nonlinear interaction between the pump and probe affect the phase of the probe pulse and, thus, the Fourier transform is distorted as compared to the Fourier transform of a probe pulse without pump. However, the evolution of the antenna resonance is manifested as can be seen from the evolution of the blue region shown by the freehand sketch (red dashed curve in (a)). Unlike the dip response of the antenna at resonance frequency, the harmonic oscillator model has a peak response, *i.e.* transmission peaks at the

resonance frequency. Figure 4.11 (b) shows the corresponding evolution of the resonance frequency in the simulation (see the blue dashed curve). The frequency domain analysis indicates that the model reproduces the evolution of the resonance frequency of antenna of the measurements.

The harmonics oscillator parameters: decay time (γ) and coupling constant (α^2) are optimized in the simulation. Decay time is adjusted so that the probe response fits best the measured probe pulse. Similarly, coupling constant is adjusted to obtain the measured resonance frequency shift 5 ps after the pump peak. Impact ionization parameters are taken from fits of impact ionization coefficient-vs-field data discussed in section 4.2.4.

The evolution of the density of free carriers that resulted in the simulated maps is shown in Fig. 4.12(b). To indicate the timeline of the evolution of carrier density, the polarization field induced by the incident THz electric field is depicted in (a). It is shown that carrier generation by impact ionization happens so fast that the carrier density increases by more than seven orders of magnitude in a sub-picosecond time. The carrier generation rate calculated simply by taking the time derivative of the carrier density indicates that more than 5×10^{18} electrons are generated in one second, transforming silicon from an insulator to a semi-metal.

The carrier generation rate obtained here is much higher than previous impact ionization rates [77], [80], [81], [120], [121] obtained by experimental measurements induced by DC electric fields in the range of 200 kV/cm - 500 kV/cm. The range of the field is limited by the high current induced breakdown of the diode used for the impact ionization investigation. As discussed in section 4.5, the low initial density of carriers (intrinsic carrier concentration) in this experiment in

comparison to the highly doped impact ionization regions in the previous transport measurements allows high impact ionization rates.

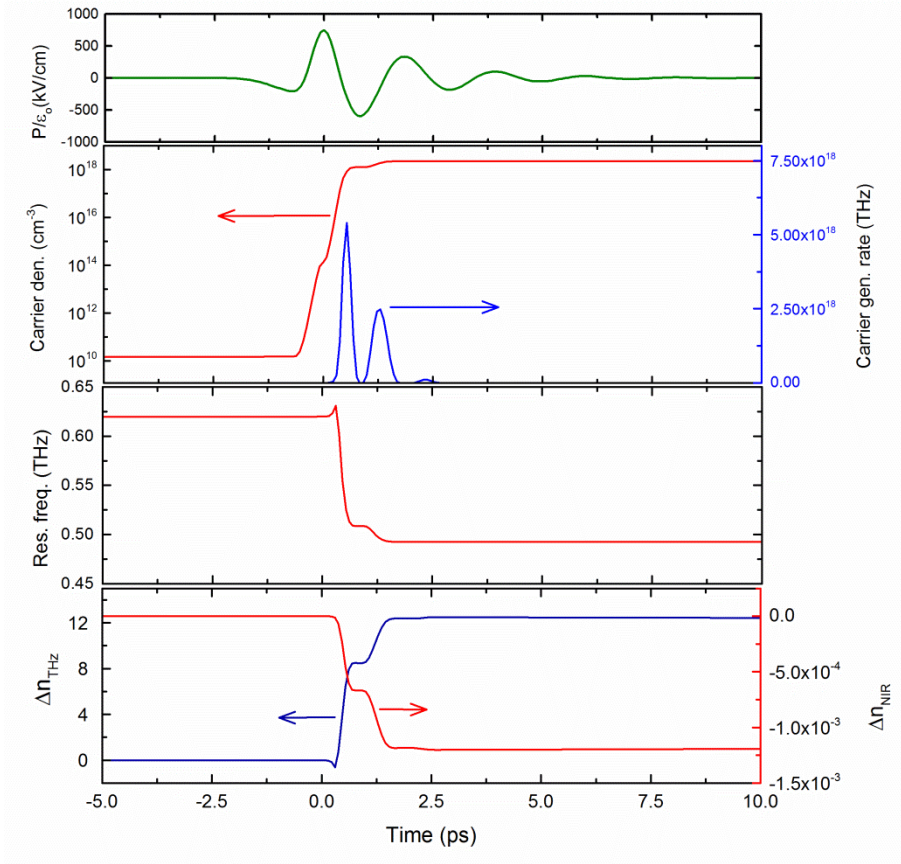


Figure 4.12. (a) The polarization field transient inside silicon in the simulation. (b) The temporal evolution of the carrier density and carrier generation rate. The carrier density reaches more than $2 \times 10^{18} \text{ cm}^{-3}$ from initial intrinsic value of $1.5 \times 10^{10} \text{ cm}^{-3}$. (c) The evolution of the instantaneous resonance frequency of a metallic dipole antenna array as a function of time. (d) The instantaneous refractive index changes at THz and NIR frequencies.

The evolution of the resonance frequency of the metal antenna due to the carrier multiplication is shown in Fig. 4.12(c). The resonance frequency

increases initially slightly before it reduces significantly. The initial kink is a Drude response where the refractive index increases in the intermediate carrier densities. At the peak of the THz pump where there is significant free carrier generation, resonance frequency drops significantly ultimately resulting in a resonance shift of 20% in a time of just few picoseconds. It is too be noted that the change in resonance frequency is significant once high density of carriers is achieved. In this condition, the plasma frequency is high enough (comparable to THz frequency, ω) that dialectic permittivity is affected significantly. The change of refractive indices at THz frequencies and 800 nm are shown in Fig. 4.12(d). It shows that the THz refractive index increases significantly. The change of index of refraction at THz frequencies amounts to 6000 times higher than the corresponding change of the refractive index at NIR frequencies.

In a separate measurement, the dynamics of the carrier generation is also demonstrated by directly measuring the local reflectivity change of a tightly focused 800 nm pulse (measurement done at Kyoto University). The details of the experiment are described in section 4.2.1. The refractive index change at 800 nm obtained from NIR reflectivity measurements are shown in Fig. 4.13 for incident THz fields of up to 700 kV/cm. The measurement shows that the refractive index of silicon can be reduced by 6×10^{-3} at 800 nm and confirm the generation of enormous density of carriers in a time scale of 1 ps.

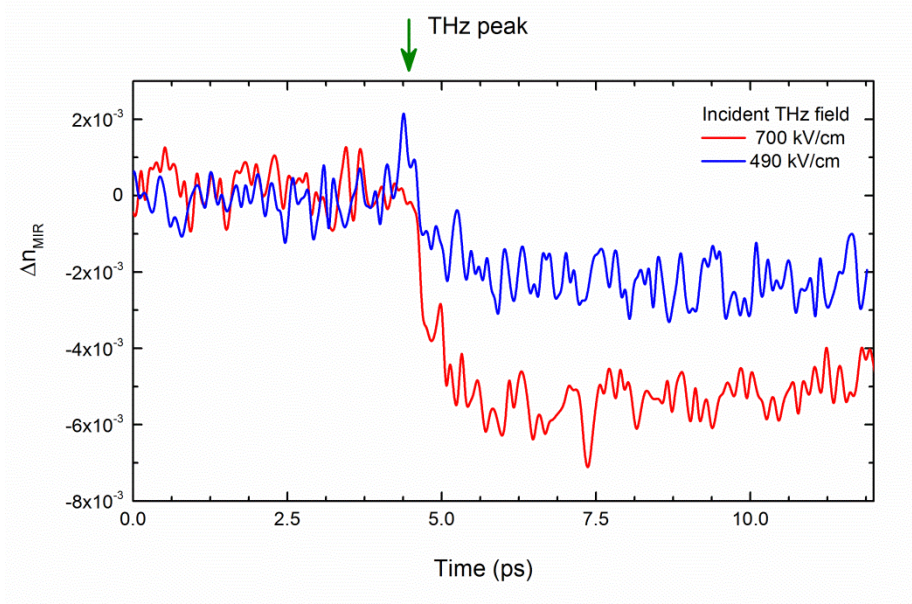


Figure 4.13. Refractive index change of silicon at 800 nm near the tip of a metallic dipole antenna as a function of the pump-probe delay time for incident THz fields of 700 and 490 kV/cm. The approximate location of the pump peak is indicated by green arrow.

4.3.5 Conclusion

It is shown in section 4.3 that THz pump-THz probe measurements enable time-resolved measurements of the antenna resonance shift and carrier density evolution. The resonant frequency of a dipole antenna is uniquely defined by its physical length and the effective refractive index of its surrounding media. While it is impossible to change the antenna length fast, we show that its resonance frequency can be modified dynamically in sub-picosecond time scale. The resonance frequency of the metallic dipole antenna is modulated by a 20% within a picosecond induced by THz initiated carrier multiplication. The refractive index of silicon near antenna tips changes significantly in the THz spectral range reaching more than 12

due to the generation of enormous density of free carriers. This substantial modulation of the resonance frequency can be made reversible on the picosecond time scale by using a substrate with ultrashort carrier lifetime or fabricating PIN diode next to impact ionization region or by ion-implantation [122], [123], thus paving the way for an ultrafast all-optical nonlinear signal processing at sub-THz frequencies and possibly high bitrate THz wireless communications. On the other hand the THz-induced resonance frequency shift demonstrates to be a useful tool to probe the carrier dynamics in semiconductors in high electric fields.

Chapter 5

Broadband THz spectroscopy of silicon carbide

5.1 Introduction to silicon carbide

Silicon carbide (SiC) has been known for more than a century. In fact, the first photoluminescence was observed in SiC and it was used to make the first light emitting diodes (LED) [124], [125]. Even though its application in the area of LED's is limited by the development of more efficient Ga-based LEDs and the difficulty in producing high quality wafers, it maintains an application niche where it is used for high power electronic applications and electronic applications in severe environmental conditions such as in high voltage systems and high temperature situations [126], [127].

The building blocks of silicon carbide crystals are double layers of silicon and carbon atoms which are constructed in various stacking orders. In each layer the silicon (carbon) atoms have a hexagonal arrangement with three distinct sites (labelled *A*, *B*, *C*) in arranging the SiC double-atomic layers. Differences in the stacking sequence of the atomic layers and their number per unit cell results in more than 200 polytypes [128]. The polytypes are identified by a natural number equal to the number of Si-C bilayers per unit cell in the direction perpendicular to the basal plane (*c*-axis) and an alphabetic symbol representing syngony of the Bravais lattice: *C* for cubic, *H* for hexagonal, and *R* for rhombohedral [129]. The stacking sequences of the most popular polytypes, 3*C*, 4*H* and 6*H* are shown in Fig 5.1(a-c). The stacking sequence for the smallest polytype (3*C*-SiC) is ABCABC... and "3" refers to the number of Si-C double layers in one repeating unit. The

corresponding stacking sequences of the $4H$ - and $6H$ -SiC polytypes are ABCBABC..., and ABCACBABCACB.... respectively (see Fig. 5.1). A single Si (or C) atomic layer can have a local cubic (k) or hexagonal (h) environment with respect to the immediate neighbors forming crystallographic nonequivalent sites in the lattice. For example, one k - and one h - crystallographic sites exist for $4H$ -SiC carbide where as $3C$ -SiC has only k -type lattice sites [130].

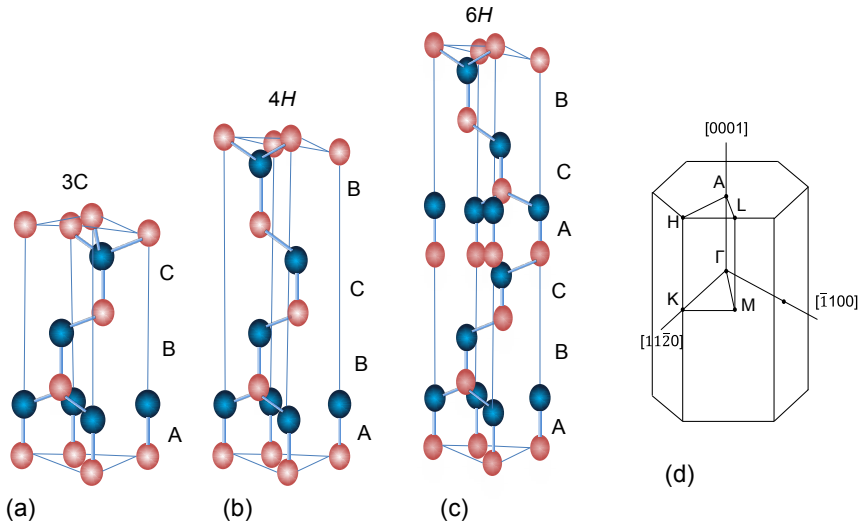


Figure 5.1. Stacking sequences of the carbon-silicon bilayers in (a) $3C$, (b) $4H$, and (c) $6H$ -SiC unit cells. Dark red spheres represent silicon and dark blue spheres represent carbon atoms. (d) Brillouin zone of a hexagonal lattice. Dots indicate the labels of the high symmetry points in hexagonal structures. The c -axis is parallel to the $[0001]$ direction.

Silicon carbide has unique features that make it a promising material for high power optoelectronic applications. For example, $4H$ -SiC has three times larger band gap, five times higher breakdown voltage, twice higher saturation velocity and three times higher thermal conductivity as compared to silicon [33], [34]. These features make it a superior alternative to silicon

for fast switching devices that can operate in high electric fields and at high temperatures. Although the different polytypes of SiC have the same element composition, they manifest differences in their electrical and optical characteristics. SiC is a wide bandgap material with gap energy higher than 2.2 eV which varies depending on the polytype.

Nowadays SiC is considered a potential material for the fabrication of LEDs because its bandgap can be engineered to emit over the entire visible spectrum. Even though the indirect bandgap property of SiC makes it less efficient photoluminescent emitter, addition of appropriate dopants results in high quantum efficiency of up to 95% that covers the entire visible spectral range [131], [132]. This allows fabrication of white light LED sources with unparalleled color quality. Similar advances in technologies to better utilize the material and crystal growth technologies, which enable high quality and large area epitaxial layer productions, reinvigorates interest in SiC.

Rapid advances in the generation of high power THz signal with electric field in the MV/cm require a robust material platform for fabrication of devices. Due to its high bandgap and breakdown voltage the response of SiC stays linear over an extended range of strong electric fields compared to silicon. It is shown that silicon exhibits a nonlinear transmission in a strong THz pulse due to carrier generation by impact ionization [133]. The impact ionization field in SiC is expected to be much higher than silicon which means that SiC can be a suitable material platform for device fabrication for the future high power THz devices. In addition to its high mechanical strength, large breakdown voltage and functionality at high temperatures, undoped SiC has high transmission in the main THz band.

5.2 Folded zone phonon modes in SiC

An effective utilization of the material requires a complete understanding of its optoelectronic properties. Crystal lattice vibrations

(phonons) influence the electronic properties, and consequently, impact SiC based device performances. Phonon dynamics of the silicon carbide polytypes that are the most commonly used in devices are examined in this chapter. Among the popular polytypes, the growth of large area *4H*- and *6H*-SiC wafers has been possible and are available commercially. These polytypes are the most commonly used polytypes for electronic applications because they have high free carrier mobility. *4H*-SiC is the most stable polytype and has higher free carrier mobility than *6H*-SiC [35], [134]. Thus, the lattice vibration properties and dispersion characteristics in the THz spectral range of *4H*- and *6H*-SiC are investigated by using a broadband THz source. *Ab-initio* DFT simulations are implemented to elaborate the details of phonon dynamics.

THz spectral range covers important phonon energies in solid state materials including SiC. The strong longitudinal (TO) and transverse optic phonons (LO) located at approximately between 24 and 29 THz respectively are well known and their characteristics are nearly independent of the polytype. These two polar phonons form a powerful Reststrahlen band; a feature that makes SiC a promising candidate for implementing surface phonon polaritons to expand the success of plasmonics in sub-diffraction manipulation of light at the UV and visible towards the IR and THz spectral regime [135]. Recently, the phonon resonances properties of SiC has been utilized to enhance near field signal significantly [136]. This shows that lattice vibrations in SiC can be applicable in nanoscale optical sensing for high temperature and high power applications. While the strong polar phonon modes have been investigated in depth [137], weak folded zone phonon modes which appear in large size polytypes are not completely understood.

The unit cell length of larger polytypes with *n*-SiC bilayers along the *c*-axis is *n*-times larger than that of the smallest polytype, *3C*-SiC. Thus, the

Brillouin zone in the Γ -L direction (see Fig. 1(d)) is reduced to $1/n$ compared to the large Brillouin zone of the 3C-SiC. The dispersion curves of the phonon modes propagating along the c-axis in the large polytypes are determined by the folded dispersion curves resulting in several new phonon modes. The new phonon modes are known as folded zone modes. Examples of zone folding is shown by the dispersion curves of 3C, 4H and 6H polytypes of SiC, calculated by *ab initio* DFT simulations with a commercial CASTEP simulator (see Fig. 5.2). The dispersion curves in the axial direction of 4H and 6H-SiC polytypes can be derived from the large Brillouin zone dispersion curves. Several folded zone phonon modes are expected both in 4H and 6H polytypes. However, some of them are not infrared active that means that it is not possible to detect them with the THz electric fields. Some of them are axial modes and are not accessible (are weakly accessible) directly with THz probe at normal incidence for crystals that are c-cut. The samples investigated here are c-cut.

The folded zone phonon modes are characteristic to the specific polytype. Their specificity makes them a fitting tag to uniquely identify polytypes in a noncontact manner. This is particularly important as the interest in SiC is growing and fast characterization of larger area wafers in a nondestructive way is crucial to advance their optoelectronic functionality. THz sources offer such characterization capabilities in a straight forward transmission measurement, providing a wealth of information about the phonon modes such as lattice vibration strength, resonance frequency and optical dispersion characteristics in THz spectral range.

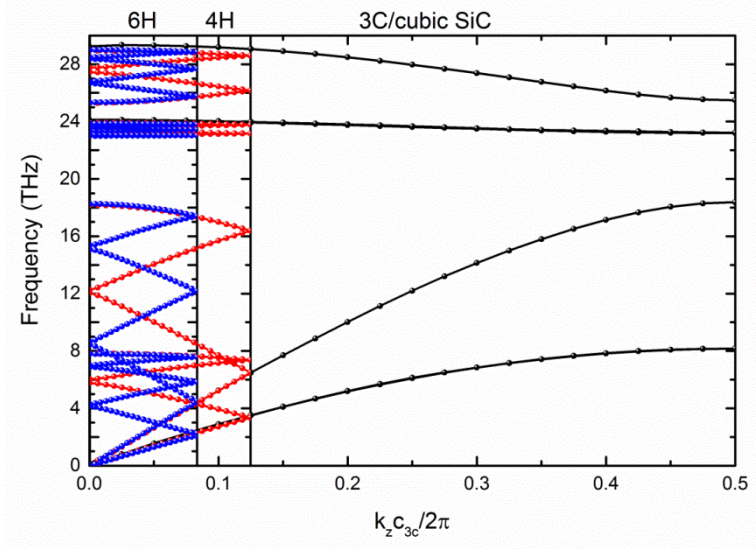


Figure 5.2. Phonon dispersion curves of 3C (black), 4H (red) and 6H (blue) polytypes of SiC. The dispersion curves are obtained by *ab initio* DFT simulation using a commercial CASTEP simulator. The dispersion curves of the 4H and 6H polytypes can be obtained by zone folding of dispersion curves of 3C polytype.

5.3 Experimental technique

Previously phonon modes in silicon carbide have been investigated using Infrared and Raman spectroscopy that do not provide phase information [138]–[143]. THz-TDS system is used in this study to investigate phonon dynamics which gives strength of lattice vibration and phase information. The phase information reveals phonon decay time and optical dispersion properties at THz frequencies. A spectrally broad THz pulse is generated in a laser induced air plasma [46]–[48]. A simplified schematic diagram of the optical setup is shown in Fig. 5.2(a). A 800 nm pulse from a Ti:sapphire regenerative amplifier with a pulse energy of 3.5 mJ and a pulse duration of 35 fs is used for the THz generation. Femtosecond pulses at 800 nm and its second harmonic (400 nm) generated in a BBO crystal are focused in air to generate air plasma. An asymmetric current induced by a symmetry-broken

laser field composed of the fundamental and second harmonic laser pulses during field ionization of air generates the broadband THz pulses [144]. The fact that the THz pulse is generated in air, where phonon absorption is not limiting the THz bandwidth like in the THz generation in nonlinear crystals, THz pulse with extremely broad spectral range can be generated. The THz is imaged onto the sample using a pair of off-axis parabolic mirrors. After passing through the sample, the THz beam is collimated again and tightly focused for THz detection.

An air based coherent detection (ABCD) which is the inverse of the generation process is used for mapping out the THz waveform [49], [50]. ABCD involves a third order nonlinear process that generates a second harmonic of the 800 nm probe pulse which is proportional to the THz field; $E_{2\omega} \propto E_{THz}E_{\omega}E_{\omega}$, where E stand for the electric field amplitude and ω is angular frequency. The THz electric field is determined by measuring the intensity of the second harmonic of the probe pulse using an avalanche photodiode or a photomultiplier. The probe beam is routed over a variable delay to measure the THz transient. It is noted that the temporal width of the pulse is so short that the delay stage with very small step size is required to properly measure the THz Transient. In these measurements step size of 1 μm which corresponds to a time step of 6.7 fs is used. Coherent detection is achieved by applying a strong bias voltage (HVM in Fig. 5.3(a)).

The spectral amplitude of the THz radiation generated by the air plasma setup in the absence of the sample is shown in Fig. 5.3(b). Clearly the generated THz radiation has a spectral range spanning approximately 40 THz. The dip near the frequency of 18.4 THz is due to a well know phonon absorption in silicon wafer placed on the collimated section of the THz beam path to block any optical signal reaching the sample.

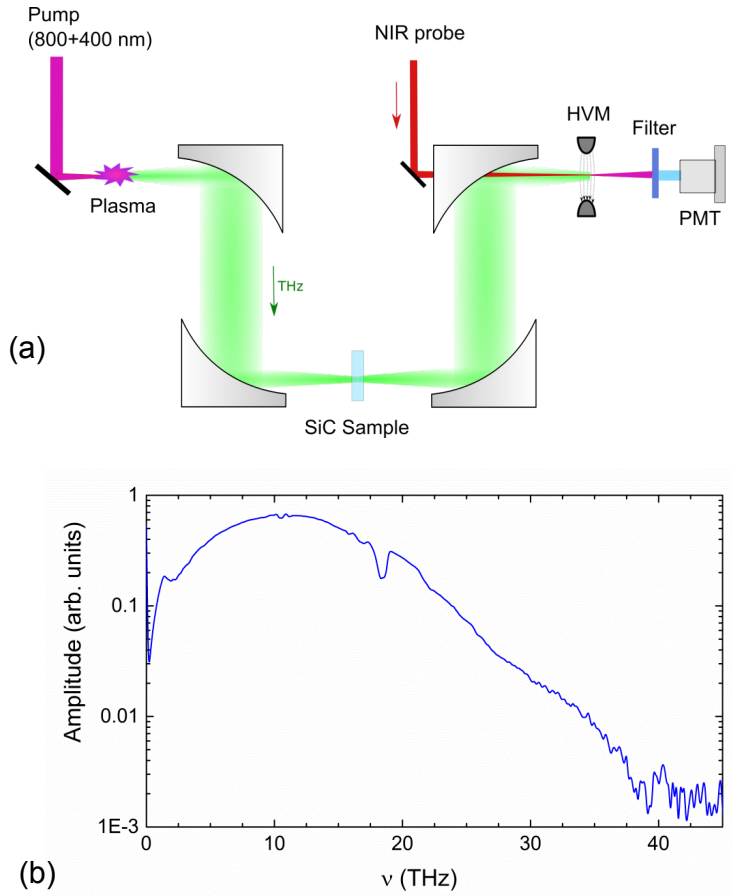


Figure 5.3. (a) A simplified schematic diagram of the broadband THz generation and detection setup. THz pulse is generated in two-color air plasma and ABCD detection is used to measure the THz transient. (b) Measured spectral amplitude versus frequency without the sample. The dip near 18.4 THz is due to phonon absorption by the silicon wafer placed on the THz beam path to block the optical pulses reaching the sample.

Comparison between the detected signals in the presence of the sample and reference measurements in a standard transmission THz time domain spectroscopic (TDS) setup is used to investigate the phonon dynamics and dispersion properties of the sample. Even though the setup also works in the reflection mode, a transmission mode is used in the investigations presented

in this chapter due to its higher sensitivity. The samples used in this investigation are lightly doped $4H$ -SiC and a compensated $6H$ -SiC. In the compensated sample the free carriers from undesired dopants are depleted by adding a complementary dopant. The sample thickness of the $4H$ -SiC sample is measured to be $349\text{ }\mu\text{m}$ and $500\text{ }\mu\text{m}$ for $6H$ -SiC sample. The electric field transient of the transmitted THz pulse through the $4H$ -SiC sample and a reference measurement in a nitrogen atmosphere are shown in Fig. 5.4(a). The reference THz pulse is nearly a single cycle pulse with a FWHF width of 27 fs. The ringing in the reference signal after the main THz signal is a result of phonon absorption in silicon placed in the THz beam path. In both $4H$ and $6H$ samples a very strong ringing which decays over several picoseconds is observed and it does completely vanish until the Fabry-Perot reflection signal arrives. The ringing is a result of the resonant lattice vibrations in the samples.

5.4 Measurement results and discussion

The measured spectral transmission of the lightly doped $4H$ sample is shown in Fig. 5.4 (b) (solid red curve). The spectral transmission is calculated as the ratio of the magnitude of the Fourier transforms of the THz transients transmitted through the sample and in air reference. Important features in the spectral transmission include a very sharp resonant absorption dips at frequencies of 7.97 and 18.43 THz (phonon modes) and spectral transmission limited only up to 20 THz. These features manifest the strong interaction of THz field with the crystal lattice. The phonon modes at 7.97 and 18.43 THz are located below the strong polar phonons and are the weak folded zone phonon modes. The locations of these phonon lines have been measured previously by Raman Scattering measurements and their values of 266 and 610 cm^{-1} [137] agree exactly with our measurements. The phonon mode at 7.97 THz is a planar acoustic phonon mode which means that the

lattice vibration is along the plane perpendicular to the c-axis whereas the phonon resonance at 18.43 THz is an axial acoustic phonon. In our measurement setting the THz is polarized in the planar direction and the strong interaction of the THz field with planar phonon is expected. The spectral transmission is limited only to approximately 20 THz is mainly due to the strong absorption by the polar phonons at resonance frequencies of 23.9 THz (TO) and 29.1 THz (LO).

The capability to measure the phase of the transmitted THz gives further insight into the phonon modes which can be described by analyzing the dielectric properties in the THz spectral range. The complex transmission function can be related to the complex refractive index (\tilde{n}) as,

$$T(\nu) = \frac{E_{Sample}(\nu)}{E_{Ref}(\nu)} = \frac{4\tilde{n}}{(\tilde{n} + 1)^2} e^{i(\tilde{n}-1)\frac{2\pi\nu}{c}d} \quad (5.1)$$

where $E_{Sample}(\nu)$ is the electric field transmitted through the sample, $E_{Ref}(\nu)$ is the reference signal, d is the sample thickness and c is the speed of light. Equation 5.1 can be split into magnitude and phase relations as,

$$|T(\nu)| = \frac{4\sqrt{n^2 + k^2}}{(n + 1)^2 + k^2} e^{-k\frac{2\pi\nu d}{c}} \quad (5.2)$$

$$\begin{aligned} \Phi(\nu) = & -(n - 1)\frac{2\pi\nu d}{c} \\ & + \text{atan}\left(\frac{k(n^2 + k^2 - 1)}{n(n + 1)^2 + k^2(n + 2)}\right) + 2\pi N \end{aligned} \quad (5.3)$$

where n and k are the real and imaginary components of the refractive index and N is an integer. The equations are simplified if the material is not absorbing, *i.e.* if $k = 0$. The complex refractive index and the dielectric permittivity of the sample are calculated from the transmission by using Eq. (5.2) and (5.3).

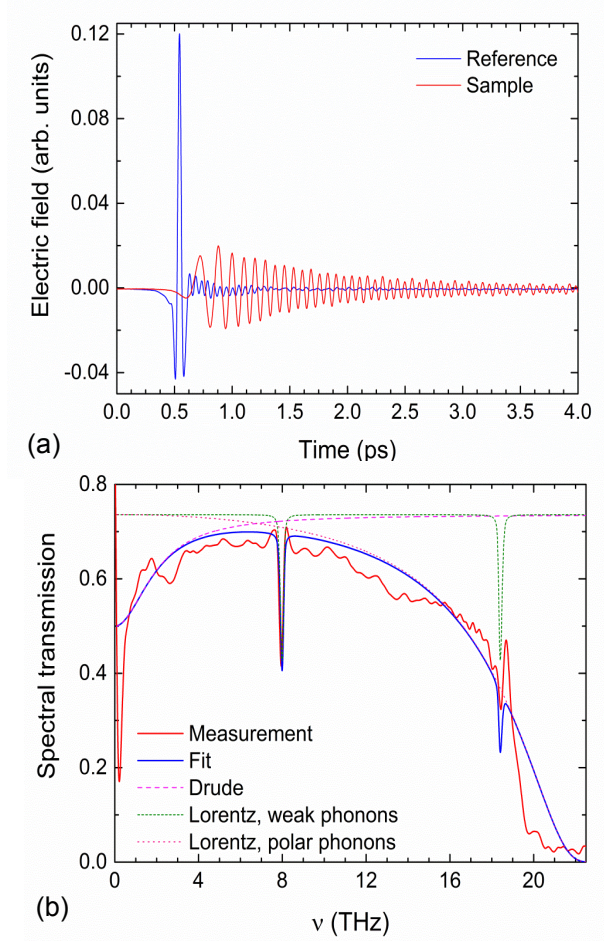


Figure 5.4. (a) Transmitted THz waveform in an air reference (blue curve) and a lightly doped, 349 μm thick 4H-SiC sample (red curve). The inset shows reference signal zoomed in a shorter time window. (b) Spectral transmission of the sample obtained by the ratio of the Fourier transforms of the sample and air reference. Fits to the transmission with different dispersion models are included. The blue fit considers free carrier and phonon contributions (Drude + Lorentz).

To clarify these spectral dispersion features a model that includes a Lorentz oscillator for the strong polar phonons, a Lorentz oscillator for the folded zone phonon modes and the Drude model that accounts for the free electrons is applied. The dielectric permittivity is given by [137],

$$\epsilon(\omega) = \epsilon_{\infty} + \frac{\epsilon_{\infty}(\omega_{LO}^2 - \omega_{TO}^2)}{(\omega_{TO}^2 - \omega^2 - i\omega\Gamma)} - \frac{\omega_p^2}{\omega^2 + i\omega\gamma_D} + \sum_i \frac{4\pi\rho_i\omega_{Li}^2}{(\omega_{Li}^2 - \omega^2 - i\omega\gamma_{Li})} \quad (5.4)$$

where ϵ_{∞} is the residual dielectric permittivity ω_{LO} , ω_{TO} are longitudinal and transverse optical phonon frequencies respectively, Γ is the phonon damping constant, ω_p is the plasma frequency, γ_D is the momentum relaxation rate of free carriers, ω_L , γ_L are resonance frequencies of folded phonon modes and the corresponding damping rate respectively. The second term in Eq. 5.4 represents the strong polar phonon absorption. The third term is the Drude response that accounts for the free carrier contributions and the last term accounts the folded zone phonon modes.

Figure 5.4(b) shows that the measured transmission (red curve) in the 4H sample fits very well with the model fit considers the contributions of the phonon modes and the free carriers (blue curve). The fitting parameters are summarized in table 5.1. To elaborate the contribution of free electrons and phonons in the dispersion relationship, the permittivity is fitted by selective inclusion of each contribution. If we consider only the folded zone phonon modes (green dotted line), the transmission is expected to be flat along the measurement spectrum except dips at the resonant frequencies.

Consideration of the only the Drude model, reproduces reduction in transmission on the lower side of the spectrum (pink dash lines). The Drude fit shows that the sample has a carrier density of approximately $3.1 \times 10^{15} \text{ cm}^{-3}$ which is due to light nitrogen doping that is typically introduced during crystal growth from the growth atmosphere. The common practice to neutralize the nitrogen impact is depleting free carriers by adding a compensating material, commonly vanadium. In a compensated 6H-SiC, we do not observe a decrease in transmission at lower frequencies observed in

the 4H sample. The sample provider also confirmed that the sample is compensated and is nearly free of carriers at the room temperature.

Parameter	4H-SiC	6H-SiC
ϵ_{∞}	6.52	6.6
ν_{TO}	23.89 THz [137]	23.89 THz
ν_{LO}	29.11 THz [137]	29.14 THz
Γ	1.68 THz	2.1 THz
γ_D	11.3 THz	--
ρ_1	1.2×10^{-4}	3.9×10^{-5}
ρ_2	2.2×10^{-5}	3.9×10^{-5}
ν_{l1}	7.97 THz	7.2 THz
ν_{l2}	18.43 THz	7.05 THz
γ_{L1}	0.25 THz	0.2 THz
γ_{L2}	0.25 THz	0.4 THz

Table 5.1. Parameters used in the modeling of the spectral dispersion relationship of 4H- and 6H-SiC samples. Parameters that are taken from literature are cited and all the rest of the parameters are fitting values.

The consideration of the TO and LO phonons result in a significant decrease in transmission on the high frequency side of the spectrum and transmission almost vanishes beyond 20 THz. It is noted here that fitted residual dielectric permittivity differs depending on whether the polar phonon contributions are considered or not. Consideration of the strong polar phonon contribution, results in residual dielectric permittivity, $\epsilon_{\infty} = 9.7$ which is larger by a factor of $1 + (\omega_{LO}^2 - \omega_{TO}^2)/\omega_{TO}^2$. This can be obtained by calculating the ration of the dielectric permittivity at $\omega = 0$ in the presence of polar phonon contribution and without. This explains the discrepancy in literature regarding the residual dielectric permittivity between these values.

The real and imaginary parts of the refractive index for the *4H* and *6H*-SiC samples are calculated from the fitted dispersion relation and shown in Fig. 5.5. The refractive indices measured in the transmission TDS are very well reproduced. It is observed that the refractive indices of the two materials are very similar apart from different absorption lines due to the folded zone phonon modes. The optical dispersion in the THz spectral range is mainly influenced by the strong large zone phonon modes which are independent of the polytype and thus the refractive indices of the two polytypes considered here are comparable.

Analysis of the measurements of the *6H*-SiC sample reveals phonon modes at frequencies of 7.08 and 7.23 THz which form a doublet as shown in Fig. 5.5(b). These phonon modes are planar acoustic phonon modes. The doublet features are attributed to the energy discontinuity in the phonon dispersion of the large Brillouin zone [140]. The inset in Fig. 5.5(b) shows the measured transmission and theoretical fit. It is shown that the transmission does not decrease at the low frequencies like in the *4H* sample. That confirms the absence of Drude contribution as the free carriers are depleted by compensation in the *6H* sample.

These measurements reveal weak folded zone phonon modes that are less accessible experimentally in the FTIR. They are located close to the limit of the spectral capability of FTIR systems which signifies the importance of the broadband THz radiation in the analysis of the weak phonon modes of SiC polytypes. It is essential to note that there are several weak folded zone phonon modes in the THz bandwidth available in this measurement which are either too weak to be measured or they are not accessible in the polarization direction of the THz pulse [137], [145], [146].

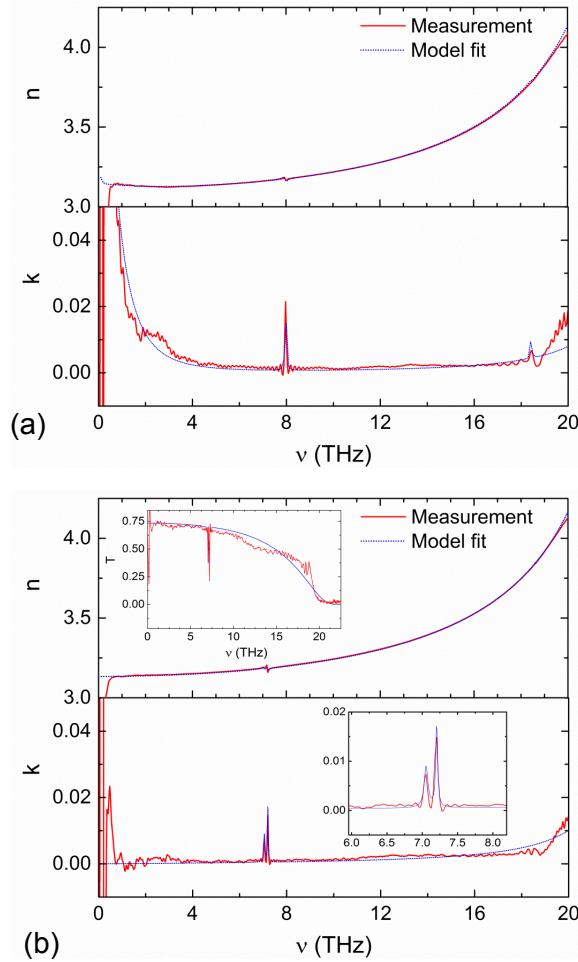


Figure 5.5. (a) Real and imaginary indices of the 4H-SiC (b) and the 6H-SiC. The red lines are measurements using time domain spectroscopy and the blue lines are fits that account free carrier and phonon contributions using Drude model and Lorentz oscillator models respectively. The inset in a frame of (b) shows zoom of the doublet resonance feature near 7 THz. The inset at the upper frame of (b) shows the spectral transmission of the 6H sample with a fit.

5.5 DFT simulation of the phonon modes

To examine the dynamics of the vibrational resonances that are observed in the broadband measurements, *ab-initio* density functional theory (DFT)

studies of 4H-SiC and 6H-SiC are performed. Commercially available DFT simulation software, CASTEP (Cambridge Serial Total Energy Package) is used to perform the simulations. The weak folded phonon modes which are specific to the polytype and strong polar modes are identified with the corresponding frequencies and intensities. The DFT with the PBE exchange-correlation functional optimized for solids [147] reproduces the weak folded phonon frequencies very well and importantly, allows identification of the nature of these weak modes. As the partial charges on Si (+1.25e) and C (-1.25e) nearly compensate each other, the total dipole moment and hence infrared activity is approximately 4 orders of magnitude weaker than the polar TO mode at 23.9 THz, as confirmed both by DFT simulation and by the relative strengths of the Lorentz oscillators used to fit the experimental data.

In addition to predicting the resonance frequencies of the lattice vibrations and intensities, DFT simulations elaborate the motion of the atomic layers that give rise to the measured resonances of the lattice vibrations. Figure 5.6 shows the directions of vibrations of atoms for phonon modes of resonance frequencies at 7.82 THz and 18.14 THz. The simulations indicate that these phonon modes are very weak as compared to the TO phonon mode expected at a frequency of 23.9 THz. The intensity of the phonon mode at 7.82 THz is 6.6×10^5 times weaker; however, it was clearly measurable with the THz spectroscopy. The directions of motion of atoms at this vibrational frequency are shown by arrows in Fig. 5.6 (b) and the vibrations are in a plane perpendicular to the *c*-axis of the crystal. The directions of vibrations are in the direction of polarization of the THz field which makes them more easily accessible. The direction of motion of the atoms for the 18.2 THz resonance is depicted in Fig. 5.6 (c). The carbon atoms are stationary and silicon atoms vibrate as indicated by the arrows. The phonon resonance at 18.2 THz is 29 times stronger than the phonon

mode at 7.82 THz. However, it is weakly detected by THz measurement. This is clarified in the DFT simulation that the atomic vibrations are orthogonal to polarization of the THz field (axial phonon modes) and thus, THz does not couple effectively with the lattice vibration at this frequency.

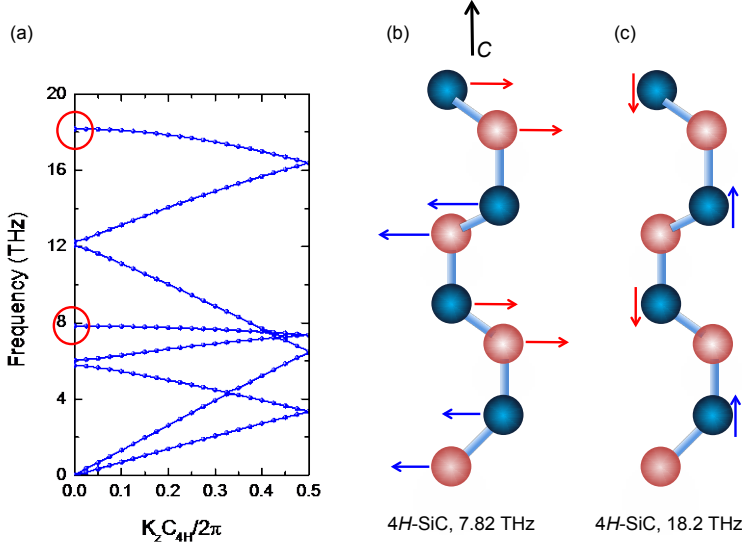


Figure 5.6. (a) Phonon dispersion curves of 4H-SiC crystal lattice obtained by DFT simulations. The motion of silicon and carbon atoms of phonons resonance frequencies of (b) 7.82 THz, and (c) 18.2 THz. The first is planar phonon mode and second is axial phonon mode. The corresponding measured resonance frequencies are 7.97 THz and 18.43 THz. The red circles in (a) show the location of the measured resonance frequencies on the phonon dispersion curve.

Similarly the mechanical dynamics of the phonon modes in the 6H-SiC sample are predicted in the DFT simulation with excellent agreement with the measurements. Infrared active phonon doublet measured by THz transmission is shown in Fig. 5.7. DFT simulations predict resonance frequencies of 6.87 and 7.01 THz and the motion of atoms that results in these resonance frequencies are indicated in Fig. 5.7 (b) and (c) respectively. The DFT simulation also predicts additional resonance frequencies near 15

THz and 23 THz. Similar to the 18.2 THz resonance frequency of the 4*H*-SiC, the resonance frequency near 15 THz is a longitudinal mode which is not accessible with the polarization of incident THz field. These modes have been accessible by tilting the sample so that THz polarization will have a component along the vibration direction of this phonon mode. The phonon modes predicted in simulation at frequencies of 23.03 and 23.3 THz are close to the TO phonon mode. The much stronger TO phonon mode obscures these modes and are difficult to measure.

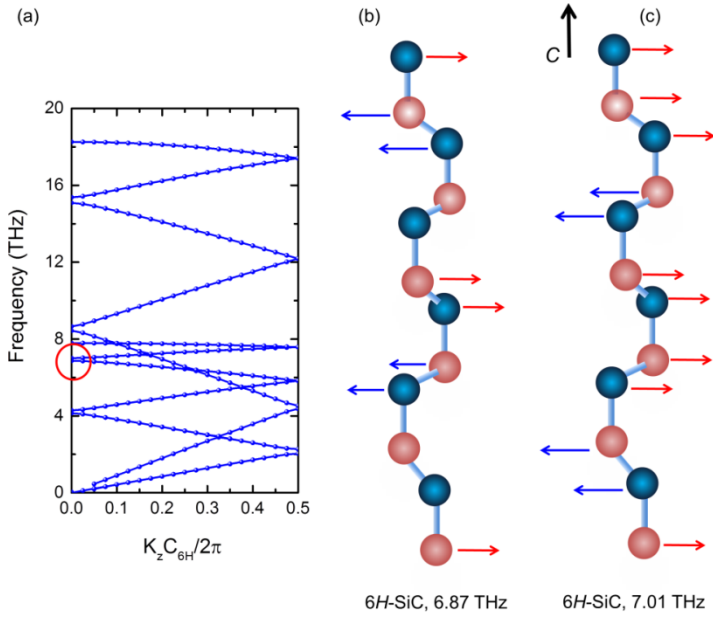


Figure 5.7. (a) Phonon dispersion curves of the 6*H*-SiC polytype. The red circle indicates the location of the resonance frequencies on the dispersion curve. The motion of silicon and carbon atoms at resonance frequencies of (b) 6.87 THz and (c) 7.01 THz. The corresponding measured resonance frequencies are 7.05 THz and 7.2 THz.

5.6 FTIR measurement results

The THz transmission measurements show that SiC is highly dispersive in the THz spectral range. The refractive indices of both 4H-SiC and 6H-SiC change approximately by 1 between 1-20 THz. This is due to the strong polar phonon modes which result in a clear Reststrahlen band. The polar phonons are so strong that it even affects the THz transmission as low as 1 THz.

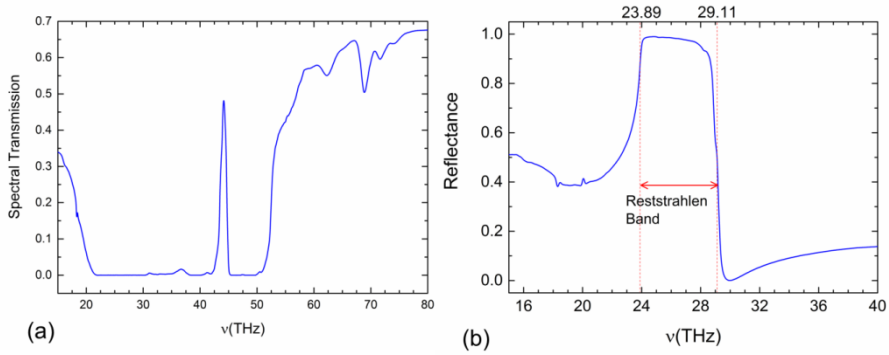


Figure 5.8. (a) Spectral transmission of a 4H-SiC sample as a function of frequency measured by FTIR. (b) Reflectance as a function of frequency. The red dot lines border the Reststrahlen band and are the location of the LO and TO phonon frequencies.

To complete the dispersion information encompassing the Reststrahlen band, FTIR measurements in transmission and reflection mode are conducted. The spectral transmittance and reflectance from the 4H-SiC sample are shown in Fig. 5.8. It is observed that a Reststrahlen band between the LO and TO phonons is formed in silicon carbide. The dielectric permittivity is negative in this band and the complex refractive index is purely imaginary. As a result the optical signals in this spectral range are completely reflected and it displays metal like behavior. In section 5.3 it is shown that the damping rate of phonons in SiC is smaller than that of metals

which meant that it results in stronger and sharper resonances in the frequency domain. These attributes foretell the prospect of SiC for high sensitivity sensing applications especially in high temperature and high power applications.

5.7 Conclusion

In this chapter optical properties and phonon modes of silicon carbide in the THz spectral range are explained. Folded zone lattice vibrations at frequencies of 7.82 and 18.2 THz for 4H, and 7.05 THz and 7.2 THz for 6H are measured and characterized with a broadband THz source and DFT simulations. It has been shown that a THz spectroscopy is a powerful tool to probe infrared-active folded zone phonon modes with the capability of phase measurement that enables complete understanding of the dispersion and decaying time properties. The folded zone phonon modes result in Si-C atomic layers to move with respect to each other within the unit cell in a pattern characteristic to the polytype. Their specificity to the polytype is an ideal tag to identify polytypes uniquely. Due to the strong TO and LO polar phonon modes, the measurements show that SiC is a very dispersive material in the THz spectral range. The strong polar phonons located at 23.9 (TO phonon) and 29.1 THz (LO phonon) form a Reststrahlen band in the frequency range bounded by them. The possibilities of strong and sharp resonances are excellent features for highly sensitive sensing applications and surface phonon polaritonics.

Chapter 6

THz-induced nonlinear transmission in silicon carbide

6.1 Introduction

Silicon is a popular material platform for many THz systems and devices due to its high transmission in the THz spectral. However, recent advances in the THz science and technology enable generation of electric fields in MV/cm with table-top systems [12]–[14], [18]. In strong THz fields, free carrier generation by impact ionization, even from intrinsic silicon, makes it no more transparent and can affect device performances [133]. We also observed a gradual degradation of optical reflectivity signal in the THz pump-optical probe experiments discussed in chapter 4 in an elongated exposure of the silicon sample by intense THz fields due to THz-induced sample damage. These call for a more robust material platform for the strong THz fields. The possibility to tailor the material platform to have a controlled nonlinear response is beneficial for novel integrated nonlinear device fabrications, thus, it broadens its functionality.

In chapter 5 it has been discussed that undoped *4H* and *6H* polytypes of silicon carbide (SiC) have high transmission in the THz spectral range, except the sharp absorption lines due to weak folded zone phonon modes and suppression of transmission at high frequencies beyond 20 THz. A wide-band gap SiC with five times higher breakdown voltage than silicon and a high radiation resistance is a promising material platform that complement silicon in the high power THz applications. We discuss in this chapter that SiC can tailored to have a THz-induced nonlinear response with sub-

picosecond switching time by adding appropriate dopants. Such ultrafast transmission modulation can be utilized for the future THz-based all-optical signal processing.

Introduction of dopants to the SiC is a crucial factor for its application in electronic devices. Selective addition of dopants is used to tune its photoluminescence wavelength in the visible spectral range. In this case, full understanding of its conductivity property such as dopant ionization and hot electron effects will help to improve the light emission efficiency. Furthermore, in its application niche in the high power electronics the material is expected to experience a strong electric field. This shows that understanding the hot carrier dynamics and its conductivity property is essential for the advancement of its utilization. These characteristics can be probed by a THz signal.

In this chapter conductivity property of nitrogen, aluminum and boron (N-Al-B) co-doped 4H-SiC sample that demonstrate a nonlinear THz transmission is discussed. In the investigations broadband THz source is used to perform linear spectroscopy of the sample. Drude-based modelling is applied to extract carrier transport parameters. After the linear THz characterization of the sample, the nonlinear carrier dynamics of the processes that give rise to the nonlinear THz transmission are discussed.

6.2 Electronic properties of silicon carbide

Silicon carbide is an indirect band gap material with a wide band gap that depends on the polytype. The common polytypes of silicon carbide, 3C, 2H, 4H, 6H and 15R have indirect bandgaps of 2.4, 3.26, 3.02, 2.80, and 2.99 eV respectively [130], [148]. The band structure of a 4H-SiC [149] that was obtained by *ab initio* study based on density functional theory (DFT) in the local-density approximation (LDA) is shown in Fig. 6.1. In the reported LDA calculation converged basis sets, which define the Bagayoko, Zhao and

Williams (BZW) procedure, are implemented to solve the prominent problem of the bandgap underestimation in many LDA calculations [150].

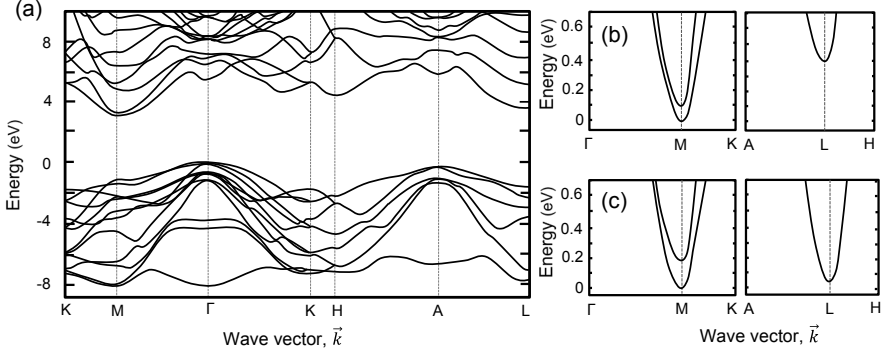


Figure 6.1. (a) Electronic band structure of 4H-SiC obtain with *ab initio* simulation using density functional theory in the local density approximation (LDA) [149]. Band structure near the lowest conduction band minima for (b) 4H-SiC, and (c) 6H-SiC.

The band structures of 4H- and 6H-SiC near the conduction band minimum which are reported by Choyke *et al.* and calculated by using full-potential linear augmented plane wave method are shown in Fig. 6(b) and (c) respectively [152]. A conduction band minimum is located at the *M*-symmetry point of the Brillouin zone for the 4H-SiC and along *LM* symmetry line for the 6H-SiC [150], [151]. The peculiar feature of the band structure near the conduction band minimum is the presence of a second conduction band minimum in close proximity to the first. The exact value of the separation between the two conduction band minima in 4H-SiC varies in different reports in the range of 0.12-0.18 eV [34], [149], [152]–[154]. Even though the conduction band structures of 4H- and 6H-SiC are quite similar [35], [151], [153], band folding in the later results in a flat conduction band minimum along *LM* symmetry line of the Brillouin zone.

Effective masses of the electrons and holes near the conduction band minimum and valence band maximum respectively play a crucial role in

determining the electronic properties of semiconductors. The carrier mobility (μ) in semiconductors is inversely proportional to the effective mass of the carriers (m^*) such that, $\mu = e\tau/m^*$, where e is the electronic charge, τ is the carrier scattering time. An isotropic effective electron masses of 4H-SiC are measured by optically detected cyclotron resonance (ODCR) technique [36], [155] and are determined along principal directions as $m_{ML}=0.33m_o$, $m_{MI}=0.58m_o$, and $m_{MK}=0.31m_o$ [156] where m_o is the electronic rest mass. The second conduction band minimum has different effective electron masses along the three principal directions with $m_{ML}=0.71m_o$, $m_{MI}=0.78m_o$, and $m_{MK}=0.16m_o$ [153]. The differences of effective masses in the two conduction band minima results in different electron transport properties.

The other electronic property relevant to this study is the dopant characteristics of the SiC. Impurities are doped in SiC crystal structure to engender free carriers and host recombination centers. Nitrogen, aluminum and boron are among the most common dopants in SiC. Nitrogen is the main donor impurity in all the polytypes and typical undoped SiC layers are n-doped due to uncontrolled nitrogen presence during growth and high solubility of nitrogen in SiC [129]. Nitrogen atoms replace carbon in the 4H-SiC lattice at both the cubic (k) and the hexagonal (h) inequivalent lattice sites in equal proportions [145]. Nitrogen has the lowest ionization energy of all the dopants where the ionization energy of nitrogen dopant state in 4H-SiC at the k -lattice is, $E_D(k) = 52.1$ meV, and at h -lattice point, $E_D(h) = 91.8$ meV as measured by IR-absorption spectroscopy [145] .

Aluminum and boron dopants act as acceptors in the 4H-SiC and replace silicon atom in the crystal lattice. The ionization energies of these acceptor dopants vary in the literature. Aluminum dopant ionization energy ranges from 191-230 meV and the ionization energy of boron 285-390 meV [129], [157]–[160]. Boron is also reported to result in an additional deeper energy level close to the center of the bandgap with a binding energy of 540-

730 meV [157]. A photoluminescence measurement by Sun, *et al* [161] indicates that there is no emission from shallower boron acceptor states which indicate that the deep dopant levels are prevalent.

6.3 Characterization of sample with low-power THz sources

The investigated sample is a 4H-SiC co-doped with nitrogen, boron and aluminum; initially designed for an efficient SiC based photoluminescence experiment in a separate group. The sample is grown by physical vapor deposition [162] and it is cut parallel to the *c*-plane. The sample thickness is measured to be 230 ± 10 μm . The uncertainty in thickness measurement is due to nonuniform thickness measured across different regions of the sample. The dopant content of the sample is measured by secondary ion mass spectrometry (SIMS) and the corresponding concentrations of the dopants are $1.1 \pm 0.2 \times 10^{19}$, $3.9 \pm 0.2 \times 10^{18}$, and $2.9 \pm 0.2 \times 10^{15}$ cm^{-3} for boron, nitrogen and aluminum respectively.

The binding energy of the nitrogen dopant is the smallest among the dopants and the free carriers from this donor states are the most accessible. The density of aluminum is three orders of magnitude less than that of nitrogen and the binding energy is approximately four times higher than the binding energy of nitrogen; as a result its contribution to free carriers and, subsequently to THz absorption is expected to be negligible. Boron has the highest dopant state ionization energy and the sample needs to be heated to a very high temperature to release the free carriers. Therefore, nitrogen is the major contributor of free carriers by either a field-induced ionization or a thermal excitation.

6.3.1 Transmission measurements with a weak THz signal

Firstly, the transmission and conductivity characteristics of the sample are investigated using a weak THz signal from T-Ray 4000 source from the Picometrix. The spectral THz transmission of the sample at 300 K is shown in Fig. 6.2. The schematic of THz-TDS measurement setting is shown as an inset. The sample has high absorption which is an indication of high density of thermally released free carriers from dopant states at the room temperature.

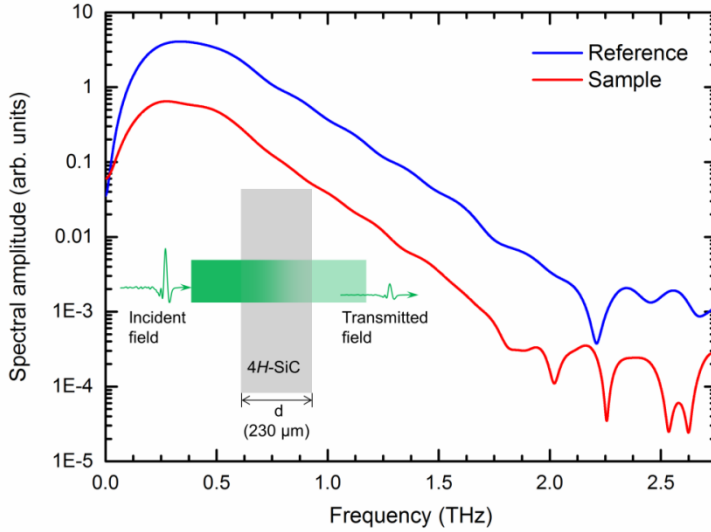


Figure 6.2. Spectral amplitude of the THz pulse transmitted through the N-Al-B co-doped 4H-SiC sample at 300 K and a reference measurement. The THz source is a T-Ray 4000 from Picometrix. The schematic of the transmission measurement setup is shown in the inset. The THz beam is focused on the sample with a 3" THz lens.

From the transmission measurements the dielectric property of the sample and its complex optical conductivity can be calculated. The relationships between transmission and dielectric constants are detailed in section 5.3. The complex conductivity as a function of frequency, $\tilde{\sigma}(\omega)$, is

obtained from real and imaginary refractive indices (n, k respectively) from the following relationship.

$$\tilde{\sigma}(\omega) = 2nk\epsilon_0\omega + i(\epsilon_\infty - n^2 + k^2)\epsilon_0\omega \quad (6.1)$$

Here, ϵ_0 is the dielectric permittivity of free space and ϵ_∞ the background dielectric constant. The linear response of frequency-dependent complex conductivity is often well described by the classical Drude model where the complex conductivity is given by,

$$\tilde{\sigma}(\omega) = \frac{\sigma_{DC}}{1 - i\omega\tau}, \quad (6.2)$$

where $\sigma_{DC} = Ne^2\tau/m^*$, τ are the DC conductivity and the scattering time respectively. N, m^* are the density and the effective mass of free carriers respectively. The real and imaginary conductivities of the sample measured at different temperatures are indicated in Fig. 6.3. It is observed that as temperature decrease, the real part of the conductivity reduces. This indicates the DC conductivity reduces which means that the density of free carriers reduces. As temperature decreases, the number of thermally excited free carriers also decreases. The details about thermal excitation of free carriers are discussed in section 6.3.5.

In a typical Drude response, the real conductivity reduces with frequency near zero frequency. On the other hand the imaginary part of conductivity increases with frequency near zero frequency before it starts decreasing in the frequency range of, $\omega > 1/\tau$. The measurements shown in Fig. 6.3 do not show these features. The real conductivities show slight increase with frequency and imaginary frequencies decrease slightly near zero frequency. These features are rather attributes of the Drude-Smith (DS) model. In fact conductivities in the spectral range covered by the T-Ray source are rather flat and reliable extraction of conductivity features is not

plausible. Thus, analysis with a broadband THz source is discussed in the following sections (6.2.3-6.2.4).

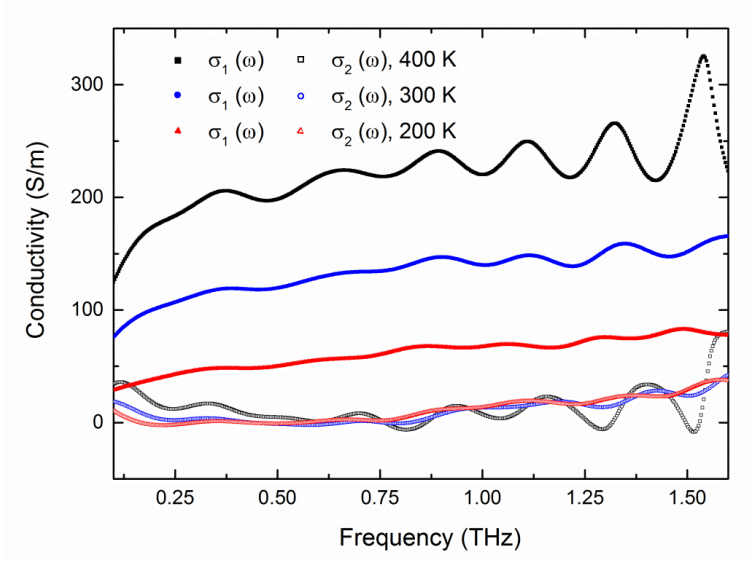


Figure 6.3. The complex conductivities of N-Al-B co-doped 4H-SiC sample as a function of frequency at temperatures of 200, 300, and 400 K. The maximum frequency in these measurements is limited by bandwidth of THz pulse from the T-Ray source.

6.3.2 Transmission measurements in the broadband THz Setup

For quantitative estimations of the scattering time and density of carriers analysis of the sample is performed with a THz-TDS with a broadband THz source. The details of the measurement setup are described in section 5.2. The sample is placed at the focus of the THz beam and THz transmission is measured. The Broadband THz transmission which is the ratio of the Fourier transform of the THz transient with and without the sample measured at the room temperature is shown in Fig. 6.4(a). The spectral amplitude of the THz signal as a function of frequency is shown in the inset. The transmission is

very low in comparison to the compensated/lightly doped SiC samples characterized in chapter 5.

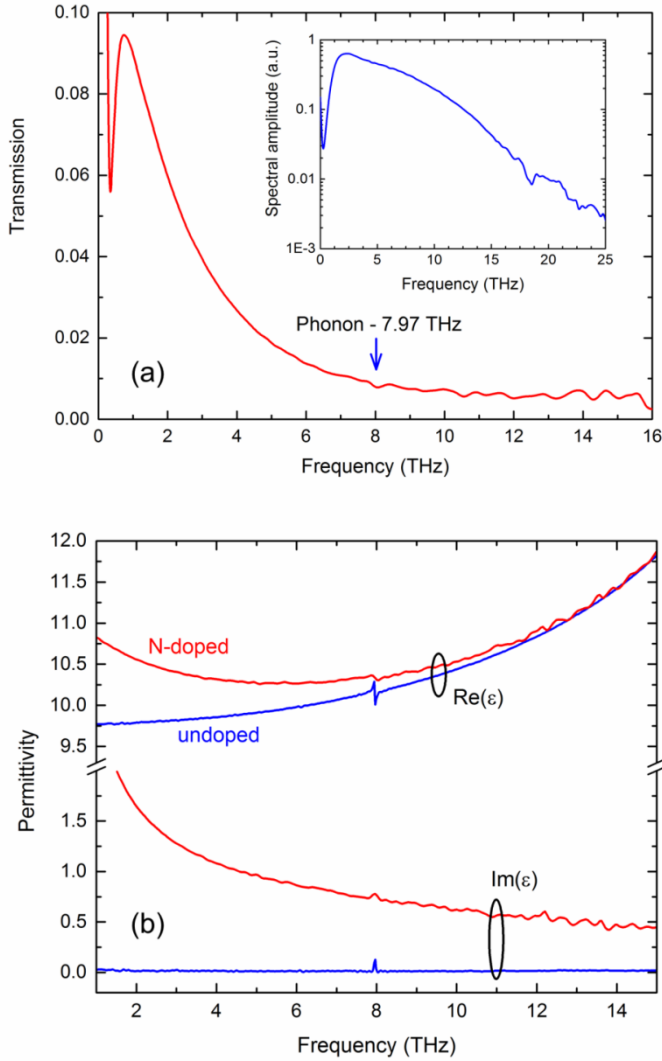


Figure 6.4. (a) Transmission of a broadband THz signal in N-B-Al co-doped 4H-SiC sample. The blue arrow indicates the location of the folded zone phonon mode (7.97 THz). The inset shows the spectral amplitude of the THz source without the sample. (b) Real and imaginary dielectric permittivity of a doped sample (red curve) and an undoped 4H-SiC sample (blue curves).

The dielectric properties of the sample are evaluated from the transmission measurement. The details of the procedure can be referred in chapter 5. Dielectric permittivity of the doped sample (red curve) and a compensated 4H-SiC sample (blue curves) are shown in Fig. 6.4(b). The dielectric permittivity of the doped sample deviates from that of an un-doped sample especially on the low frequency side due to presence of free carriers in the doped sample. Even though the transmission is rather low at high frequencies, folded zone phonon mode at 7.97 THz which is specific to the 4H polytype is noticeable.

6.3.4 Conductivity modeling with Drude-based models

To interpret the THz transmission in terms of the microscopic free carrier properties, the conductivities are calculated from the dielectric properties using Eq. 6.1. The real and imaginary conductivities are shown in Fig. 6.5. Unlike the measurements with T-Ray 4000 source, access to the high frequency in this measurement setup, reveals clear increase in real conductivity with frequencies up to approximately 10 THz. On the other hand the imaginary conductivity decreases with frequency up to approximately 4 THz with negative conductivity values. These frequency dependences are not characteristic of the classic Drude model. These features can be fitted with the Drude-Smith conductivity model which describes disordered systems such as quasi-crystals and percolated systems. Unlike Drude model where it is assumed that isotropic elastic scattering results in randomization of momentum, carriers are assumed to have back-scattering component and the memory effect is incorporated in the DS scattering model.

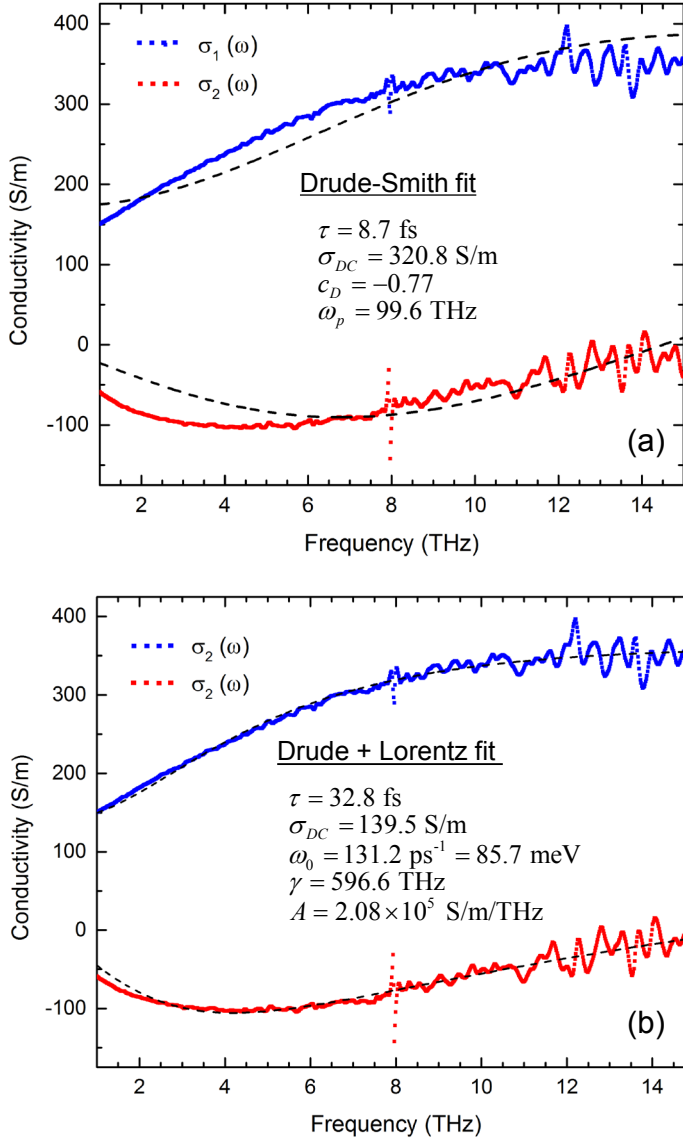


Figure 6.5. Complex conductivity of N-Al-B co-doped 4H-SiC sample calculated from the broadband THz transmission measurement with (a) Drude-Smith Fit, (b) Drude+Lorentz fit. The DS and DL fits are shown by dashed black curves. The fitting parameters of the models are included as an inset to the plots. Sample thickness of 228 μm is used in the fits.

Assuming that the memory effect is persistent for only one collision, the frequency dependence of the complex conductivity in DS model is given by [163],

$$\tilde{\sigma}(\omega) = \frac{\sigma_{DC}}{1 - i\omega\tau} \left(1 + \frac{c_D}{1 - i\omega\tau} \right). \quad (6.3)$$

Alternatively, the real and imaginary parts of conductivity can be written as,

$$\sigma_1(\omega) = \frac{\omega_p^2 \epsilon_0 \tau}{[1 + (\omega\tau)^2]^2} [1 + (\omega\tau)^2 + c_D(1 - (\omega\tau)^2)] \quad (6.4)$$

$$\sigma_2(\omega) = \frac{\omega_p^2 \epsilon_0 \tau^2 \omega}{[1 + (\omega\tau)^2]^2} [1 + (\omega\tau)^2 + 2c_D] \quad (6.5)$$

where σ_{DC} is the DC conductivity, ϵ_0 is dielectric permittivity of free space, τ is the momentum relaxation time, ω_p is the plasma frequency defined by $\omega_p = \sqrt{Ne^2/\epsilon_0 m^*}$, m^* is the effective mass of the free carrier, N is density of free carriers and c_D is the fraction of the electron's original velocity that is retained after back scattering. The DS fits to the real and imaginary conductivities have shown to be quite acceptable in terms of numerical accuracy. However, the derived parameters are not realistic. The scattering time of approximately 8 fs is much smaller than previously reported values of highly doped silicon carbide [164]. Additionally, the small value of c_D implies a significant disorder in the sample which is not likely as the supplier specified rather a uniformly grown crystal.

High absorption can also result from a resonant THz absorption which can be expected in doped silicon carbide due to the presence of low binding energy dopant states or valley-orbit splitting [164]. The complex conductivity response with resonant absorption can be described by a Lorentz-type response. In the presence of free carriers and resonant

absorption at frequency ω_0 , the complex conductivity can be written as sum of the Drude and Lorentz contributions, *i.e.*

$$\tilde{\sigma}(\omega) = \frac{\sigma_{DC}}{1 - i\omega\tau} + \frac{A\omega}{\omega\gamma + i(\omega_0^2 - \omega^2)} \quad (6.6)$$

where A is constant that determines the strength of the resonant absorption and γ is the damping rate of the resonant absorption. Fitting of the complex conductivity with Drude+Lorentz model (Eq. 6.5) shows excellent agreement between fits and measurements as shown in Fig. 6.5(b) for a sample thickness of 228 μm . The fits indicate that a resonant absorption is located at frequency of 20.9 THz or energy of 85.7 meV. This value is close to the binding energy of the nitrogen dopant state at the h -lattice point (91.8 meV [145]). This means that there is a strong, broad absorption centered at this frequency that results in generation of free carriers from the dopant states in a linear process. The scattering time obtained from the Drude + Lorentz fit is approximately 32.8 fs which is rather small but the sample is highly doped. In this condition, a small scattering time can be expected. From the DC conductivity the density of free carriers at room temperature can be obtained, $N = \sigma_{DC}m^*/e^2\tau = 6.4 \times 10^{16} \text{ cm}^{-3}$. Since the THz electric field is polarized perpendicular to the c -axis of the crystal lattice, a perpendicular effective mass of electrons ($m^* = m_{\perp} = 0.42m_e$, m_e is electronic mass) is used in the calculation of the density of free carriers.

6.3.5 Temperature dependence of the free carrier density

The density of free carriers generated by thermal excitation and its temperature dependence can be estimated from doping density with a neutrality equation that accounts the Fermi Dirac statistics. In nitrogen-doped 4H-SiC the neutrality equation that accounts the two donor levels at the h - and k -lattice points, and the valley-orbit interactions is given by,

$$\begin{aligned}
& N + Na \\
&= \frac{N_{dh}}{1 + g_h \exp[(E_{dh}/(k_B T))] + g_{voh} \exp[(E_{dh} - \Delta E_{voh})/(k_B T)]} \quad (6.7) \\
&+ \frac{N_{dk}}{1 + g_k \exp[E_{dk}/(k_B T)] + g_{vok} \exp[(E_{dk} - \Delta E_{vok})/(k_B T)]}
\end{aligned}$$

where N is the density of free electrons, N_a is the density of compensating centers, N_{dh} is the density donors at the h -site, N_{dk} is the density of donors at the k -site, $E_{dk} = 91.8$ meV, $E_{dh} = 52.1$ eV are the binding energies of the dopants states at the h - and the k -site respectively, k_B is the Boltzmann constant, T is the temperature, $\Delta E_{voh} = 7.1$ meV, $\Delta E_{vok} = 45.5$ meV are the valley-orbit splitting at h - and the k -sites respectively, $g_h = 2$, $g_{voh} = 4$, $g_k = 2$, $g_{vok} = 4$ are donor degeneracy factors of the h - and the k -sites. The values and the equation are taken from Pernot, *et al* [164]. As the temperature increases, more carriers are excited from the dopant state to the conduction band as can be inferred from the neutrality equation.

The temperature dependence of the free carrier density can also be measured with low power THz sources. T-Ray 4000 is used as the source of the THz pulses to measure the sample transmission as a function of temperature. The peak transmission of the sample in the temperature range of 10 K to 400 K is shown in Fig. 6.6 (red squares). The peak transmission is defined as the ratio of the peak of the electric field of the THz pulse transmitted through the sample and the pulse peak measured without the sample (air reference).

A theoretical THz transmission as a function of temperature is estimated from the carrier density obtained by the neutrality equation. The calculation procedure for transmission in the model is as follows: first, the complex conductivity is calculated from the free carrier density obtained from the neutrality equation. The conductivity calculation is based on the

Drude+Lorentz model with fitted conductivity parameters discussed in section 6.3.4. The complex refractive indices are then calculated using the relationship of Eq. 6.1. The absorption coefficient is calculated from imaginary refractive index which enables calculation of the transmission. The relationships between absorption/transmission in dielectric constants used in the calculations are [117],

$$\alpha(\omega) = \frac{2k\omega}{c} \quad (6.8)$$

$$T(\omega) = \frac{4n}{(n+1)^2} \exp(-\alpha d/2) \quad (6.9)$$

where T is the transmission, α is the absorption coefficient, c is the speed of light, n , k , are the real and imaginary refractive indices respectively, and d is the thickness of the sample. The transmission is calculated at frequency of 0.5 THz where the THz signal has high spectral amplitude. Calculations at several frequencies show that transmission does not change significantly within the main bandwidth of the T-Ray 4000 THz signal. Similar observations are manifested in the measured spectral transmission as function of frequency, *i.e.* the spectral transmission does not change significantly in the frequency range of 0.3 – 1 THz.

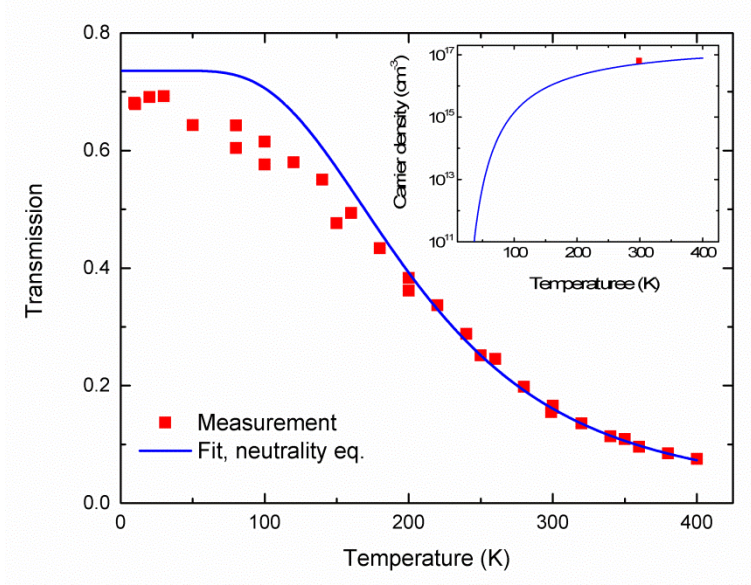


Figure 6.6. Peak transmission measured as function of temperature (red squares) and calculated by applying the neutrality equation (blue solid line). The inset shows the density of free carriers calculated from neutrality equation. The single data point in the inset (red square) is the density of free carriers obtained from analysis of the broadband THz measurement.

It is to be noted that the carrier scattering time obtained at the room temperature is used in the theoretical calculations of transmission for all temperatures. The scattering time is the cumulative effect of collisions with ionized impurities, neutral impurities, crystal lattice vibrations and defect centers. Since the sample is highly doped with boron and nitrogen, it is expected that impurity scattering is the dominant scattering mechanism [164]. In this case, the scattering time is not strongly dependent on the temperature. While this approximation is sufficient to reproduce the temperature dependent measurements and discussions in this thesis, future measurements of temperature dependence of the scattering time is advisable.

Consideration of the nitrogen dopant density measured by SIMS without compensating centers ($N_a = 0$) gives a lower theoretical THz

transmission than the measured transmission. With the dopant density as a fitting parameter, best fit between the measured and the theoretical transmission is obtained with a dopant density of, $1.6 \pm 0.1 \times 10^{18} \text{ cm}^{-3}$. The measured transmission and the theoretical fits are shown in Fig. 6.6. The lower value of the dopant density obtained in comparison to the SIMS measurement is attributed to the compensating centers depleting free electrons. Boron and aluminum atoms can act as compensating centers depleting portion of electrons which could otherwise be released [165]–[167]. It is also possible that trap states induced by the same dopant can act as compensation centers reducing the availability of active dopant states for ionization [158]. The assumption to neglect the density of compensating centers undermines the estimation of the dopant density. Moreover, not all dopant atoms are active which can release free carriers. For example, Pernot, *et al.* reported that only half of the ion-implanted aluminum atoms are active in terms of being able to release holes [158]. These measurement shows that more than half to the nitrogen dopants states are either compensated or inactive.

The density of free carriers calculated with the neutrality equation as a function of temperature is shown as an inset in Fig. 6.6. The red square shows the density of free carriers at room temperature obtained by the broadband THz-TDS measurements. As temperature decreases more electrons are bound to the dopant states and do not interact with the THz field. As a result, the transmission through the sample increases. At low temperature below 50 K, almost all carriers are bound and the THz loss is expected to be only Fresnel reflection.

The transmission measurements show a sign of saturation on the high temperature side of transmission-vs-temperature curve which is an indication that significant populations of active dopant states are ionized. The measured temperature-dependent transmission pattern and the calculations agree very

well especially at the higher temperatures. This confirms that nitrogen dopant state excitation is the primary contributor of free carriers and that the ionization energy values are acceptable. The differences of measured and theoretical transmissions at low temperatures cannot be attributed to the free carriers. The density of free carriers is very small in these temperatures and their effect on transmission is minimal. At this moment the source of the slightly lower than expected transmission in the measurement is not clear, it could possibly be additional impurities in the sample which can be confirmed by measurements on additional samples.

6.4 Nonlinear THz transmission in the 4H-SiC sample

Addition of dopants in 4H-SiC crystals results in dopants states with binding energies of approximately between 50 meV and half of the bandgap energy. In addition the conduction band minima near the *M*-symmetry point of the Brillouin zone are separated by only approximately 150 meV. In a THz electric field with moderate field strength, electrons in the conduction band can be energized beyond these energies. Inter-conduction band scattering of hot electrons or impact ionization process can provoke a nonlinear transmission in the sample. Similarly, these potential barriers can be lowered significantly triggering nonlinear process via Zener tunneling. Dynamics of the nonlinear THz field interaction in the doped 4H-SiC is discussed in this section. The time-resolved dynamics of these processes is probed by a weak probe pulse in THz-pump-THz-probe experiment which reveals ultrafast, sub-picosecond recovery time.

6.4.1 Measurement setup

Nonlinear transmission in the N-Al-B co-doped 4H-SiC sample is observed in the standard THz-TDS where an intense THz field is incident on the

sample. The optical setup used for this experiment is described in detail in chapter 2. An intense THz pulse generated by optical rectification in a lithium niobate crystal is focused on the sample. The transmitted THz signal is measured by electro-optic sampling in ZnTe and is compared with reference measurement without the sample. To measure the field-dependent THz transmission property, measurements are performed for several incident field strengths. The incident power is varied by relocating attenuating high resistivity silicon wafers before and after the sample in the collimated THz beam path. For low power THz transmission measurements, six silicon wafers are inserted in the collimated before the sample.

To learn more about the microscopic dynamics of the non-equilibrium nonlinear process, temperature dependent transmission measurements are conducted by using closed cycle helium cryostat. The sample placed in the cryogenic chamber and the temperature is varied in a controlled sample heating.

6.4.2 Results and discussion

The transmitted THz pulses in the N-Al-B co-doped 4H-SiC sample with six attenuating silicon wafers in the THz beam path before the sample (attenuated incident THz field, 33 kV/cm) and after (280 kV/cm) are shown in Fig. 6.7(a). A strong incident THz pulse transmission reduces by approximately 20% as compared to an attenuated THz field transmission. The THz transmission a function of the incident field strength is shown in Fig. 6.7(b). As incident THz field decreases, the transmission increases and saturates with further reduction in the field strength. The nonlinear transmission is not observed in an undoped 4H-SiC sample where there is no significant density of free carriers. Therefore the nonlinear signal is attributed to the nonlinear interaction of the THz field with the dopant states and the free charge carriers. The large bandgap energy of silicon carbide

means that free carrier generation by interband transition with field used in these experiments (sub-MV/cm) is not possible.

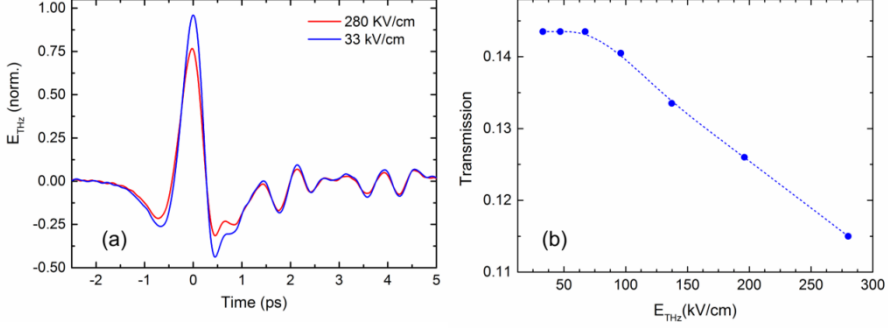


Figure 6.7. (a) Nonlinear transmission of an intense THz pulse with full THz illumination, E_{THz} and an attenuated incident field $0.12 \times E_{THz}$. (b) Peak transmission (ratio between peak of the THz pulse measured with sample and air reference) as a function of incident electric field. The blue dashed line curve is spline fit to guide the eye.

In thermal equilibrium thermally ionized free electrons populate the lowest conduction band minimum. Strong electric field accelerates electrons and when electron energy is higher than the energy difference between the two nearby conduction band minima, electrons can scatter to the second conduction band minima via inter-conduction band scattering as shown in Fig. 6.8(a). The two conduction bands have different effective electron masses and subsequently, different carrier mobility. The difference in mobility translates into the differential transmission in the measurements between the strong and the attenuated THz pulses. The sample is *c*-cut which meant that a THz field incident on the sample at the normal incidence has a polarization direction transverse to the *c*-axis of the crystal lattice. Differences in the transverse conduction band masses of electrons in the two conduction band minima result in differences in THz absorption by electrons

in the two bands. The transvers mass in the first conduction band ($\sqrt{m_{MR}m_{MK}}$) is higher than that of the second conduction band. As a result scattering of electrons to the second conduction band gives rise to an increase in absorption, *i.e.* lower transmission as observed in the measurements of strong THz fields.

In a hypothetical situation where a conduction band electron is in ballistic acceleration without scattering in an electric field of 100 kV/cm, it takes an electron in the conducting band of 4H-SiC only 83 fs to reach energy of 0.15 eV. Even though this is simplified estimation, it shows that the electrons can easily reach energy higher than the difference between the two conduction band minima with the THz field available in the setup.

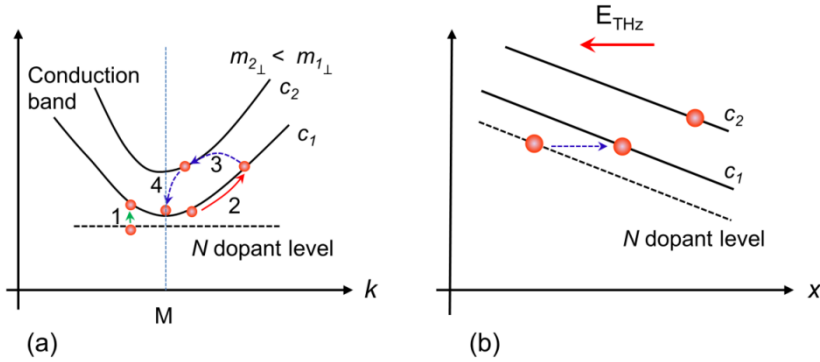


Figure 6.8. (a) Schematic diagram of THz-induced inter-conduction band scattering between the two lowest conduction bands. (b) THz-induced dopant state ionization by Zener tunneling.

Alternative, the reduction in transmission of strong fields can result from is the dynamic generation of free carriers through Zener tunneling. The THz electric field can lower the potential barrier within few atomic distances such that bound electrons at the dopant state can tunnel to the conduction band as shown in Fig. 6.8(b). The electric field needed to ionize the nitrogen dopant states can be estimated by $\mathcal{E}_i/\alpha^*e \approx 43$ kV/cm where \mathcal{E}_i is the

binding energy of the dopant state, e is electronic charge, and $\alpha^* \approx 12$ nm, is the donor Bohr radius [117], [168]. This shows that the THz electric field is sufficient to release dopant state electrons into the conduction band. The generated electrons in the conduction band results in an increased absorption.

At the same time high energy electrons in the conduction band with sufficient energy can collide with bound electrons in the dopant states liberating electrons to the conduction band in an impact ionization process. It is to be noted that while electrons need to be energized beyond separation energy of conduction band minima for intervalley scattering (>120 meV), impact ionization requires hot electrons with an energy higher than the binding energy of dopant states (appx. 52 meV for lowest N dopant state). This signifies the importance of impact ionization in the nonlinear dynamics.

The sample transmission as a function of temperature in the high power and attenuated incident THz pulses are depicted in Fig. 6.9(a). The transmission is calculated as the ratio of the peak of transmitted THz pulse and the reference pulse. The dashed lines are theoretical fits. It shows that the nonlinear transmission spans the entire temperature range of the measurement (10 - 350 K). At low temperature below 50 K, the extent of thermal ionization of dopant states is not high enough to affect low power THz transmission. In this case, the nonlinear reduction of transmission of a high power THz field can be attributed mainly to the THz-induced dopant ionization. Due to ultrashort THz pulse combined with continuous operation of the cryogenic cooling during measurements, it is expected that the THz-induced temperature rise, and subsequent thermal ionization at low temperature, is not significant. Once the free electrons are generated by the THz field, the dynamically generated free carriers are also involved in the inter-conduction band scattering or impact ionization, resulting in further reduction of transmission. On the high temperature side, significant densities

of free carriers are generated by thermal excitation and the reduction in transmission results from both dopant state ionization and inter-conduction band scattering.

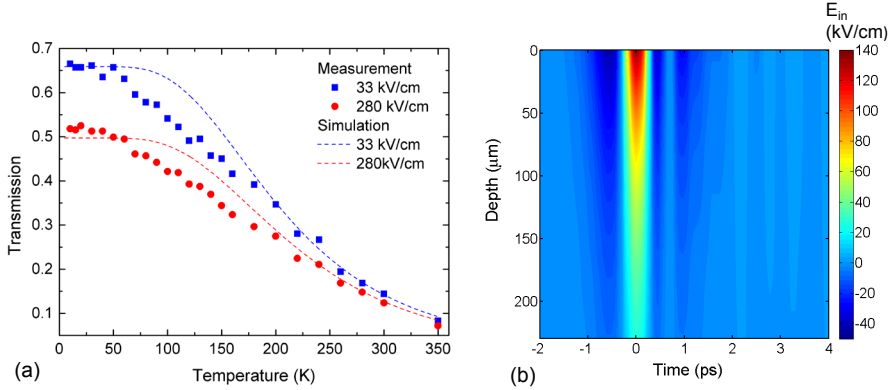


Figure 6.9. Temperature dependence of measured transmission of a weak (incident field strength = 33 kV/cm) and a strong THz fields (280 kV/cm). The dashed lines are simulation fits. (b) Simulated electric field profile inside the sample as a function of sample depth (y-axis) and delay time at room temperature. The sample is divided into 200 layers of 1.15 μm thick each and the electric field in each layer is calculated based on absorption of the previous layers and Fresnel reflection at air-sample interface of the first layer.

To understand the nonlinear processes in more detail a simplified rate equation model that incorporates only THz-induced Zener tunneling and dopant state ionization is implemented. As discussed earlier 4H-SiC has two conduction band minima separated by energy of 0.12-0.18 eV. In a strong electric field electrons in the lower conduction band are accelerated by the applied field (Eq. 6.10). Acceleration of the electron beyond the energy difference between the two conduction bands leads to scattering of electrons to the second conduction band. Consequently, the second conduction band is populated. Electrons in the second conduction also scatter back to the lower conduction band, ultimately depopulating the second conduction band

completely after the THz pulse (Eq. 6.11). At the same time electrons at dopant state can be ionized by either Zener tunneling or impact ionization. Here only Zener tunneling is considered by Eq. 6.12. These processes can be represented by a set of rate equations shown below,

$$\frac{dv_i}{dt} = \frac{eE_{in}}{m_i^*} - \frac{v_i}{\tau_i}, \quad i = 1, 2 \quad (6.10)$$

$$\frac{dN_1}{dt} = -\frac{N_1}{\tau_{12}} + \frac{N_2}{\tau_{21}} \quad (6.11)$$

$$N = N_1 + N_2 = N_0 - N_b \quad (6.12)$$

$$\frac{dN_b}{dt} = -\frac{N_b}{\tau_{zn}} \quad (6.13)$$

Where v_1 and v_2 are velocities of electrons in the first (lowest), and second conduction bands respectively. τ_i is the momentum relaxation time, N , N_1 , N_2 are densities of total free electrons, electrons in the first conduction band, second conduction band respectively. N_0 , N_b are the total dopant density and densities of bound electrons respectively. τ_{12} , τ_{21} is the inter-conduction band scattering rate from the first to the second conduction band, and from the second to the first band respectively. E_{in} is the electric field strength inside the sample. m_i^* is the effective electron masses in the i^{th} conduction band.

In a highly absorbing sample, the THz field decays significantly as it propagates in the sample. The nonlinear process depends strongly on the electric field strength. Thus, for more precise representation of the electric field inside the sample, it is modeled as many thin layers and the electric field in each layer is adjusted by accounting the absorption history of the previous layers and the Fresnel reflection at the air-sample interface. The spatial and temporal profile of the electric field inside the sample at room

temperature is shown in Fig. 6.9(b). Near the top surface the electric field is strong and high nonlinearity is expected there.

The total density of thermally excited free carriers before the arrival of the THz pulses is determined as a function of temperature using the neutrality equation (Eq. 6.6). The density of carriers is updated dynamically based a field-dependent Zener tunneling as the THz propagates in the sample. The tunneling and impact ionization rates of dopant states of 4H-SiC are unknown to the best of my knowledge. For the sake of simplicity only tunneling is considered. The tunneling rate of electrons from the dopant state to the conduction band is incorporated into the rate equation through Eq. 6.10 where the tunneling rate (τ_{zn}^{-1}) is given by [168]–[170],

$$\tau_{zn}^{-1} = \beta \left(-\frac{6\alpha}{E_{in}} \right)^{2n_l^*-1} \exp \left(-\frac{\beta}{E_{in}} \right) \quad (6.14)$$

Where α and β the tunneling parameters that depend on the ionization energy and their value is not known for silicon carbide and are used as fitting parameters in the theoretical calculations. Parameter, n_l^* is defined as $n_l^* = e^2(4\pi\epsilon_0\epsilon_r\hbar)^{-1}m^*/2\mathcal{E}_i)^{0.5}$. Here m^* is mass of electron in the direction of the electric field, \mathcal{E}_i is ionization energy of the dopant state, ϵ_r is the relative dielectric permittivity.

Once the temporal and spatial population of the free electrons is solved from the differential equations, the THz transmission, T is calculated from the sum of absorptions in all the layers,

$$T = \frac{4n_{NL}}{(n_1 + 1)(n_{NL} + 1)} \exp \left[\sum_1^{NL} (\alpha_{N,1i} + \alpha_{N,2i}) dz \right], \quad (6.15)$$

where NL is the total number of layers, n_1 is the real refractive index of the first layer, n_{NL} is the refractive index of the last layer, $dz = d/NL$ is the thickness of a single layer and $\alpha_{N,1i}$, $\alpha_{N,2i}$ are absorption coefficients in the

first and second conduction band minima respectively. Conductivity parameters obtained from the broadband THz measurements are used to calculate the absorption.

Theoretical fits of temperature dependence transmissions are shown in Fig. 6.9(a) (dashed lines). The reasonable agreement between simulation and measurement shows that the dopant ionization and inter-conduction band scattering causes the nonlinear transmission. The values of fitting parameters of the Zener tunneling rate are, $\alpha = 46$ kV/cm and $\beta = 2.3 \times 10^9 \text{ s}^{-1}$. The value of α is in good agreement with dopant tunneling field of the nitrogen dopant ($\mathcal{E}_i/\alpha^*e \approx 43$ kV/cm). However, this values need to be takes with caution because impact ionization and carrier recombination effects are not considered. These data are not known to the best of my knowledge. The carrier recombination process in the presence of many dopants further complicates the problem. Further measurements with more controlled dopants and dopant densities are needed to fully understand the dynamics of the physical mechanism of the nonlinear process.

6.4.3 Time-resolved dynamics of the THz-induced nonlinear transmission

A THz pump-THz probe experiment is performed to elucidate the time-resolved dynamics of the nonlinear process. Similar to other pump-probe measurements presented in chapter 4, a strong THz pump pulse is used to trigger the nonlinear transmission and a variably delayed weak probe pulse is used to inquire the time-resolved dynamics. The probe pule in this measurement is approximately 3% of the pump field strength and it does not induce a measurable nonlinear transmission. Comparisons between the probe transmissions in a strong pump and an attenuated pump are made in an attenuation scheme that isolates nonlinear signal in the sample (See Fig. 6.10(a)).

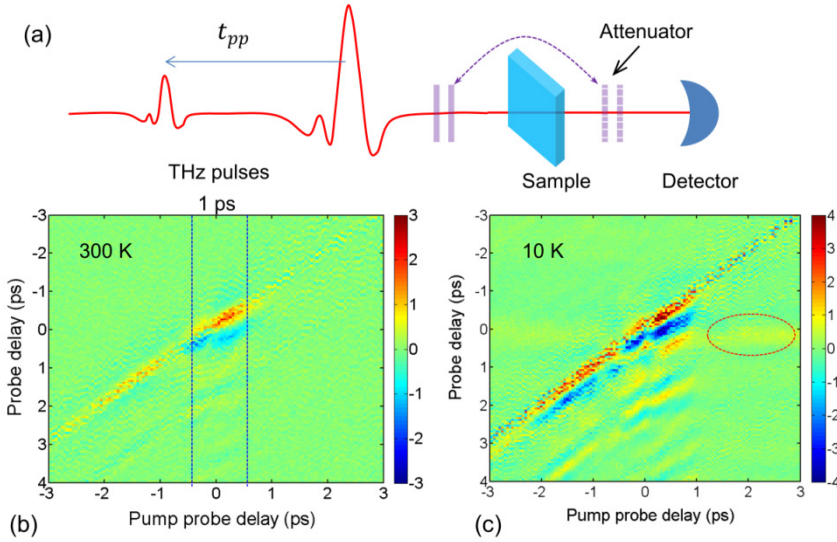


Figure 6.10. (a) Simplified THz pump-THz probe setup for the investigation of the time-resolved nonlinear dynamics. t_{pp} indicates the pump-probe delay time. Difference between probe pulse transmitted through the sample in the presence of a strong pump and weak pump pulses, (b) at room temperature, (c) at 10 K. Attenuation of the pump pulse is achieved by placing 4 silicon wafers on the collimated beam THz beam size.

Figure 6.10 (b,c) shows the amplitude difference between the transmitted probe pulses in a strong THz pump (340 kV/cm) and an attenuated THz pump (82 kV/cm) at room temperature and 10 K as a function of pump-probe delay time. The strong red and blue regions in the 2D map indicate nonlinear transmissions induced by the THz pump. In the room temperature scan, it is observed that the differential transmission is limited within a pump-probe delay time of only 1.5 ps which shows that the process has extremely fast recovery time. In the lower temperature scan once can see the weak differential transmission for several ps (See the red circled region in Fig. 6.10 (c)). The strong ringing signal at low temperature is

another indication that there is a nonlinear transmission with recovery time longer than the pump-probe delay range presented here.

To look into the time-resolved dynamics in a more intuitive perspective, the peak of the probe pulse is monitored as a function of pump probe delay time. The ratios of the probe peak scans in high power THz pump and attenuated pump as a function of pump probe delay time are shown in Fig. 6.11. For visual aid of relative location of the probe peak relative to the pump peak, the THz pump profile is indicated on the upper panel. The incident THz electric field has field strength of 340 kV/cm. The peak scan of the 300 K measurement shows that the recovery time is less than a picosecond.

In the case of low temperature peak scan it is observed that after 5 ps the peak transmission is approximately 10% lower than that of transmission before the THz pump pulse. At this pump-probe delay time there is no temporal overlap between the pump pulse and the probe pulse. For the room temperature measurement, the transmission drop recovers almost completely. These observations indicate that free carriers exist in the conduction band several picoseconds after the pump peak. Estimation of the free carriers based on the total absorption at pump-probe delay time of 5 ps indicates the presence of more than $3 \times 10^{15} \text{ cm}^{-3}$ free electrons.

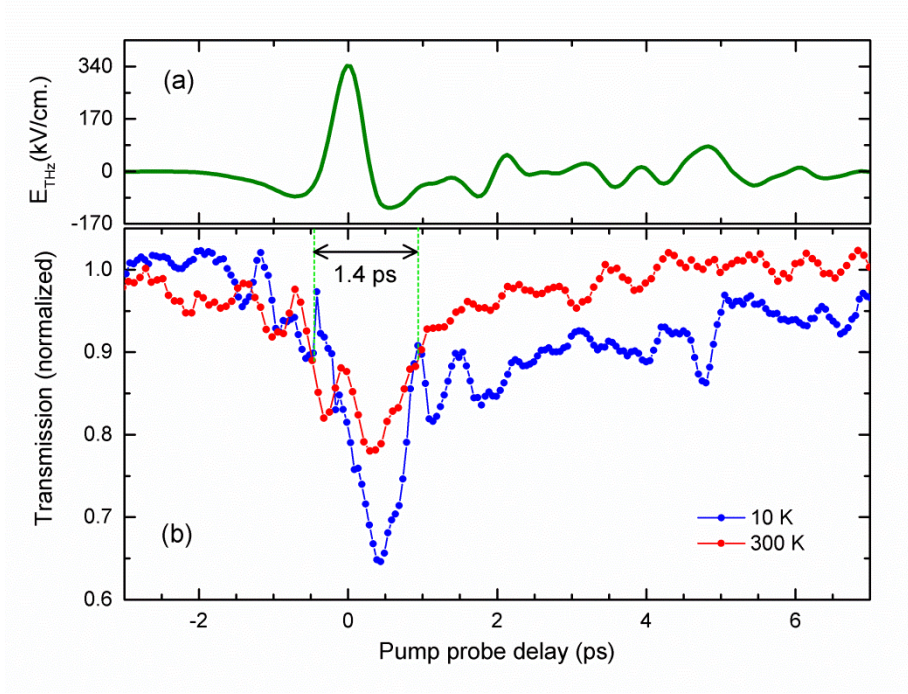


Figure 6.11. (a) Full power incident THz pulse. (b) Normalized transmission of the probe peak as a function of pump-probe delay at temperatures of 10 and 300 K. The probe peak transmission in a strong pump is normalized to the probe transmission in an attenuated pump.

THz-induced nonlinear transmissions have been investigated in many other semiconductor materials. For example intervalley and intravalley scattering processes in the conduction band have been demonstrated to show THz absorption bleaching in GaAs, Si, Ge, InGaAs among others [7], [8], [10], [71], [171], [172]. A THz-induced increase in absorption that we show here fulfils the technological applications that require transmission bleaching rather than absorption bleaching. Moreover while extremely fast modulation of transmission can be achieved by free carrier generation through ultrafast impact ionization and tunneling processes [20], [26], [133], the recovery time of the modulation process is slow and requires additional relaxation

mechanism to operate in THz modulation speeds. It is demonstrated that SiC can be used to make extremely fast modulation with sub-picosecond recovery time which can be applicable in ultrafast all-optical nonlinear signal processing at THz frequencies.

6.5 Conclusion

Extremely strong THz electric field is required to induce nonlinearity in undoped silicon carbide which is one of the most radiation resistant materials. In this chapter it is shown that SiC can be tailored to have extremely fast THz-induced nonlinear behavior in moderate THz fields by addition of appropriate dopants. This is demonstrated by investigating a highly doped 4H-SiC sample which contains high concentrations of nitrogen and boron dopants. The sample conductivity properties are analyzed with broadband THz pulses. Due to high level of doping, a low scattering time of approximately 33 fs is obtained. Investigation with the broadband THz source shows that optical complex conductivity is described by a Drude+Lorentz model where the Drude model accounts for free carriers and the Lorentz model accounts for resonant absorption by dopant states.

The doped 4H-SiC sample shows a nonlinear THz transmission attributed to THz-induced dopant ionization and scattering of hot electrons to the lower-mass conduction band minima. The nonlinear process has ultrafast sub-picosecond recovery time measured with THz pump-THz probe experiment. This shows that the nonlinear response of doped SiC demonstrates among the fastest nonlinear modulation schemes for THz signals that can be applicable over a wide range of operating temperatures.

Chapter 7

Conclusions and future perspectives

In the last few decades terahertz (THz) technology has advanced significantly. As a result the THz gap label is no more applicable. These advancements in the THz technology revealed intriguing semiconductor physical properties and field-matters interactions. In this thesis it is demonstrated that a powerful THz electric field drives nonlinear THz-matter interactions in two semiconductor materials: silicon (Si) and silicon carbide (SiC).

In the first part of the thesis intense THz pulse generation by optical rectification in lithium niobate (LiNbO_3) crystal is used to investigate THz-induced impact ionization dynamics in silicon. Field enhancement by metallic dipole antenna arrays has been used to generate strong electric fields of several MV/cm in the hot spots near the antenna tips. Previous investigations of field-induced impact ionization in silicon have been limited to sub-MV/cm due to avalanche breakdown and sample damage. The fact that THz pulses are short electric field pulses reduces the heating effect and allows investigations in a new field regime.

The antenna arrays play a dual functionality of enhancing THz electric field and probing the dynamics of generation of free carriers. In the presence of an intense THz field the resonance frequency of the metal antenna array redshifts. This is attributed to a change in the refractive index of the substrate due to the generation of substantial amount of free carriers. Experimental results and simulations show that this extremely nonlinear THz-matter interaction increases carrier density in silicon by over seven orders of magnitude. The resonance shift of the antenna arrays is measured by THz illuminations from the substrate side and the antenna side of the

sample. Enhancement of the nonlinear resonance frequency shift for the back illumination in comparison to the front illumination is demonstrated and explained theoretically. This simple observation shows that the orientation of the sample can be highly beneficial for wide ranges of nonlinear phenomena at interfaces between dielectrics.

Pump-probe measurements are implemented to understand the time-resolved dynamics of impact ionization in silicon. Firstly, the evolution of the density of free carriers is measured directly by monitoring the change of near infrared probe reflectivity in a THz plus optical pump-optical probe experiment. A 400 nm optical pump sets the initial density of free carriers. This allows investigation of impact ionization over a wide range of initial densities of carriers. An optical probe which is tightly focused to approximately 2 μm gives access to the local carrier dynamics near the antenna tips. Experiments in this setup together with Monte Carlo simulations clarify that carrier multiplication dynamics depends strongly on the initial densities of carriers. In the limit of low initial carrier density ($1.5 \times 10^{10} \text{ cm}^{-3}$) the impact ionization coefficient is an order of magnitude larger than previous reports, and approaches the fundamental Okuto limit imposed by energy conservation. In this limit, with only a single electron initially present within the experimental volume, multiplication to more than 10^8 electrons within a few hundred femtoseconds is demonstrated. At high initial densities of carriers, impact ionization rate reduces due to Auger recombination, field screening and electron-hole scattering effects. By varying the incident electric field, it is verified that the Chynoweth impact ionization model is valid in the MV/cm regime which is not analyzed before because it exceeds the damage threshold for DC fields. Additionally, the optical plus THz pump-optical probe setup demonstrates capability of quantitative evaluation of local field

profile of an antenna fabricated on silicon which can be optimized to be a non-destructive testing tool to characterize antennas and metamaterials fabricated on semiconductors.

It has also been shown that impact ionization dynamics can be resolved in time by THz pump-THz probe measurements by examining antenna resonance frequency shift of the probe pulse as a function of pump-probe delay time. The change of dielectric constant at THz frequencies is much larger than the corresponding NIR frequency for a given change of density of carriers. Under full power THz illumination the change of refractive index of silicon increases significantly reaching more than four times the refractive index of undoped silicon (with intrinsic carrier density) at THz frequencies. That means that THz probing is more sensitive than the NIR probing allowing measurement of lower changes in carrier densities. THz pump-THz probe measurements show that the resonance frequency of the metallic dipole antenna is modulated by 20% within few picoseconds due to carrier multiplication by impact ionization.

The resonant frequency of a dipole antenna is uniquely defined by its physical length and the effective refractive index of its surrounding media. While the physical length of an antenna is difficult to change rapidly, it is shown that the refractive index of the surrounding medium can be modified significantly on an ultrafast time scale by generation of free charge carriers. This substantial modulation of the resonance frequency can be made reversible on the picosecond time scale by using a substrate with ultrashort carrier lifetime or fabricating PIN diode next to impact ionization region or by ion-implantation. The possibility to modulate the resonance frequency dynamically on picosecond time scales will have important implications for the future THz wireless communication systems. Ultrafast modulation of the dielectric property of silicon using THz in a noncontact manner could also be applicable for phase modulation in all-optical signal processing even in

the telecom wavelengths. Moreover, a single electron exists near the antenna tip in high resistivity silicon which is amplified to result in more than 100 million electrons. By controlling the presence of that single electron the complete carrier multiplication process can be switched on and off. This paves the path to a new interface between single electron nano-electronics and macro-scale electronics operating at ultrahigh speeds.

Even though nonlinear process induced in strong THz fields in silicon can be beneficial, in some situations it could be undesirable. For example, if it is to be used as a material platform for fabrication of high power THz devices, undesired nonlinear effect can arise from the substrate. Thus, a more robust material that stays linear in electric fields in MV/cm characterized, namely SiC. A linear spectroscopy with broadband THz source reveals very sharp and strong resonant absorption lines due to the folded zone lattice vibrations at frequencies of 7.82 and 18.2 THz for $4H$ and 7.05 THz and 7.2 THz for $6H$ polytypes of SiC. Further investigations with the help of DFT simulations manifest the physical motion of the Si-C atomic layers for each phonon mode. It has been shown that a THz spectroscopy is a powerful tool to probe infrared-active folded zone phonon modes with the phase information that enables understanding of the optical dispersion in THz spectral region and decay time properties of phonon modes. Excitation of the folded zone phonon modes drives the Si-C atomic layers to move with respect to each other within the unit cell in a pattern characteristic to the polytypes which counts to more than 200. Their specificity to the polytype is an ideal tag to identify polytypes uniquely. Due to the strong TO (23.9 THz) and LO (29.1 THz) polar phonon modes, the measurements show that SiC is a very dispersive material in the THz spectral range.

It is expected that extremely high THz electric field is required to induce nonlinearity in undoped SiC which is one of the most radiation-resistant materials. However, it is shown for the first time that SiC can be

tailored to have extremely fast THz-induced nonlinear behavior in moderate electric fields by addition of appropriate dopants. This is demonstrated by investigating a highly doped 4H-SiC sample which contains high concentrations of nitrogen and boron dopants. The sample conductivity properties are analyzed with broadband THz pulses. Due to high level of doping, a low scattering time of approximately 33 fs is obtained for the sample. The complex optical conductivity obtained from broadband spectroscopy is described by Drude plus Lorentz model where the Drude model accounts for free carriers and the Lorentz model accounts for resonant absorption by dopant states. The doped 4H-SiC sample shows a nonlinear THz transmission attributed to THz-induced dopant state ionization and scattering of hot electrons to a lower-mass conduction band. As THz field increases, transmission decreases nonlinearly for electric fields higher than approximately 60 kV/cm. The nonlinear process has ultrafast sub-picosecond recovery time measured by THz pump-THz probe experiments. Thus, we demonstrate that SiC shows one of the fastest nonlinear modulation schemes for THz signals that can be applicable over a wide range of operating temperatures.

It has been shown that THz pump-THz probe measurements enable time-resolved understanding of the dynamics of the THz-induced nonlinear processes. Generation and detection of two THz pulses in the same crystal induces nonlinear probe signal near the temporal overlap. This might obscure the nonlinear signal induced in the sample. Particularly, the nonlinear interaction in the generation crystal is shown to be very strong in our experiments and it is advisable to use a separate crystal for generation and detection of the pump and probe THz signals in the future.

It has been demonstrated that an intense THz field has the potential to provoke interesting nonlinear interactions. Several applications of the nonlinear interactions have been proposed such as THz-induced phase

modulators, THz nearfield analyzer based on optical/THz pump-optical probe setup. It is expected that these novel functionalities will be implemented in the future.

During this PhD, a model that reproduces some features of the experimentally observed nonlinear dynamics in the doped SiC has been formulated. The nonlinear process involves several mechanisms such as free carrier generation from dopant states through impact ionization, Zener tunneling, intervalley scattering and recombination. Thus, additional measurements and simulations are needed to completely understand the physical mechanism of the nonlinear interaction. The sample that demonstrates THz-induced nonlinear effect contains several dopants that further complicate the analysis of the field-matter interaction pathways. Pump-probe measurements with more controlled sample doping will reveal more detailed understanding of the nonlinear process and help to decouple the contributions of each physical process involved in the interaction.

PhD publications

Peer reviewed journals

1. A.T. Tarekegne, K. Iwaszczuk, M. Zalkovskij, A. C. Strikwerda, and P.U. Jepsen, “Impact ionization in high resistivity silicon induced by an intense terahertz field enhanced by an antenna array,” *New J. Phys.* 17(4), 043002 (2015).
2. P. Klarskov, A.T. Tarekegne, K. Iwaszczuk, X. -C. Zhang, and P.U. Jepsen, “Amplification of resonant field enhancement by plasmonic lattice coupling in metallic slit arrays,” *Sci. Rep.* 6, 37738 (2016).
3. A.T. Tarekegne, H. Hirori, K. Tanaka, K. Iwaszczuk, and P.U. Jepsen, “Ultrafast THz-induced impact ionization dynamics in silicon in the MV/cm regime,” *New J. Phys.* 19, 123018 (2017).
4. A.T. Tarekegne, Korbinian Kaltenecker, Binbin Zhou, Krzysztof Iwaszczuk, Weifang Lu, Haiyan Ou, Stewart Clark, and Peter Uhd Jepsen, “Folded-zone phonons in 4H and 6H silicon carbide polytypes,” (to be submitted).
5. A.T. Tarekegne, K. Iwaszczuk, W. Lu, H. Ou, and P.U. Jepsen, “Ultrafast THz transmission modulator in 4H silicon carbide,” (to be submitted).

Conference contributions

6. A.T. Tarekegne, K. Iwaszczuk, W. Lu, H. Ou, and P.U. Jepsen, “Sub-picosecond nonlinear THz transmission modulation with ultrafast recovery time in silicon carbide,” **oral presentation** at Optical Terahertz Science and Technology, London, United Kingdom (2017).

7. A.T. Tarekegne, K. Kaltenecker, K. Iwaszczuk, and P.U. Jepsen, “Weak THz-frequency phonon modes in 4H and 6H silicon carbide.” **oral presentation** at Optical Terahertz Science and Technology, London, United Kingdom (2017).
8. A.T. Tarekegne, H. Hirori, K. Iwaszczuk, K. Tanaka, P. U. Jepsen, “High impact ionization rate in silicon by sub-picosecond THz electric field pulses, ” **oral presentation** at SPIE photonics west 2017, San Francisco, USA (2017).
9. A.T. Tarekegne, K. Iwaszczuk, and P.U. Jepsen, “Experimental comparison of models for ultrafast impact ionization in silicon,” **poster presentation** at CLEO-2016, San Jose, California (2016).
10. A.T. Tarekegne, H. Hirori, K. Iwaszczuk, K. Tanaka, and P.U. Jepsen, “THz-induced ultrafast modulation of NIR refractive index of silicon,” **oral presentation** at 41st international conference on infrared, millimeter and THz waves, Copenhagen, Denmark (2016).
11. J. Zhu, K. Iwaszczuk, A.T. Tarekegne, Y. Ma, and P.U. Jepsen, “Robustness of various metals against high THz field induced damage,” **oral presentation** at 41st international conference on infrared, millimeter and THz waves, Copenhagen, Denmark (2016).
12. P. Klarskov, A. Tarekegne, K. Iwaszczuk, and P. U. Jepsen, “Field enhancing coupling between microslits and lattice modes resonant at terahertz frequencies” **oral presentation** at International Workshop on Terahertz Science and Technology 2015 (OTST2015), San Diego, USA.
13. A.T. Tarekegne, K. Iwaszczuk, M. Zalkovskij, A. C. Strikwerda, and P.U. Jepsen, “Impact ionization in high resistivity silicon induced by an intense terahertz field enhanced by an antenna array,” presented at

Optical Terahertz Science and Technology, San Diego, USA (2015)
(poster).

14. A.T. Tarekegne, P. Klarskov, K. Iwaszczuk, and P.U. Jepsen, “High power terahertz induced carrier multiplication in silicon,” **oral presentation** at 40th international conference on infrared, millimeter and THz waves, Hong Kong, China (2015).
15. A.T. Tarekegne, K. Iwaszczuk, M. Zalkovskij, A. C. Strikwerda, and P.U. Jepsen, “Impact ionization in high resistivity silicon induced by an intense terahertz field enhanced by an antenna array,” **oral presentation** at the annual meeting of Danish Optical Society, Roskilde, Denmark (2014).

References

- [1] P. U. Jepsen, D. G. Cooke, and M. Koch, “Terahertz spectroscopy and imaging - Modern techniques and applications,” *Laser Photonics Rev.*, vol. 5, no. 1, pp. 124–166, 2011.
- [2] T. Kampfrath, K. Tanaka, and K. a. Nelson, “Resonant and nonresonant control over matter and light by intense terahertz transients,” *Nat. Photonics*, vol. 7, no. 9, pp. 680–690, 2013.
- [3] L. Bocklage, “Model of THz Magnetization Dynamics,” *Sci. Rep.*, vol. 6, no. March, p. 22767, 2016.
- [4] H. J. Joyce, J. L. Boland, C. L. Davies, S. Baig, and M. B. Johnston, “Electrical properties of semiconductor nanowires: Insights gained from terahertz conductivity spectroscopy,” *Semicond. Sci. Technol.*, vol. 31, no. 10, pp. 1–21, 2016.
- [5] R. Ulbricht, E. Hendry, J. Shan, T. F. Heinz, and M. Bonn, “Carrier dynamics in semiconductors studied with time-resolved terahertz spectroscopy,” *Rev. Mod. Phys.*, vol. 83, no. 2, pp. 543–586, 2011.
- [6] M. Hoffmann, J. Hebling, H. Hwang, K.-L. Yeh, and K. Nelson, “Impact ionization in InSb probed by terahertz pump—terahertz probe spectroscopy,” *Phys. Rev. B*, vol. 79, no. 161201(R), pp. 161201–1, Apr. 2009.
- [7] J. Hebling, M. C. Hoffmann, H. Y. Hwang, K. Lo Yeh, and K. A. Nelson, “Observation of nonequilibrium carrier distribution in Ge, Si, and GaAs by terahertz pump-terahertz probe measurements,” *Phys. Rev. B*, vol. 81, no. 3, pp. 1–5, 2010.
- [8] D. Turchinovich, J. M. Hvam, and M. C. Hoffmann, “Self-phase modulation of a single-cycle terahertz pulse by nonlinear free-carrier response in a semiconductor,” *Phys. Rev. B*, vol. 85, no. 20, pp. 1–5, 2012.
- [9] M. C. Hoffmann and D. Turchinovich, “Semiconductor saturable absorbers for ultrafast terahertz signals,” *Appl. Phys. Lett.*, vol. 96, no. 15, pp. 22–25, 2010.

- [10] F. Blanchard, D. Golde, F. H. Su, L. Razzari, G. Sharma, R. Morandotti, T. Ozaki, M. Reid, M. Kira, S. W. Koch, and F. A. Hegmann, "Effective mass anisotropy of hot electrons in nonparabolic conduction bands of n-doped InGaAs films using ultrafast Terahertz pump-probe techniques," *Phys. Rev. Lett.*, vol. 107, no. 10, pp. 1–4, 2011.
- [11] L. Razzari, F. H. Su, G. Sharma, F. Blanchard, A. Ayeshehshim, H. C. Bandulet, R. Morandotti, J. C. Kieffer, T. Ozaki, M. Reid, and F. A. Hegmann, "Nonlinear ultrafast modulation of the optical absorption of intense few-cycle terahertz pulses in n -doped semiconductors," *Phys. Rev. B*, vol. 79, no. 19, pp. 3–6, 2009.
- [12] H. Hirori, A. Doi, F. Blanchard, and K. Tanaka, "Single-cycle THz pulses with amplitudes exceeding 1 MV / cm generated by optical rectification in LiNbO₃," *Appl. Phys. Lett.*, vol. 98, no. 91106, p. 91106, 2011.
- [13] C. P. Hauri, C. Ruchert, C. Vicario, and F. Ardana, "Strong-field single-cycle THz pulses generated in an organic crystal," *Appl. Phys. Lett.*, vol. 99, no. 2011, pp. 2013–2016, 2011.
- [14] C. Vicario, B. Monoszlai, and C. P. Hauri, "GV/ m single-cycle terahertz fields from a laser-driven large-size partitioned organic crystal," *Phys. Rev. Lett.*, vol. 112, no. May, pp. 1–5, 2014.
- [15] M. Shalaby and C. P. Hauri, "Demonstration of a low-frequency three-dimensional terahertz bullet with extreme brightness," *Nat. Commun.*, vol. 6, pp. 1–8, 2015.
- [16] T. I. Oh, Y. J. Yoo, Y. S. You, and K. Y. Kim, "Generation of strong terahertz fields exceeding 8 MV/cm at 1kHz and real-time beam profiling," *Appl. Phys. Lett.*, vol. 105, no. 4, pp. 1–5, 2014.
- [17] K. Fan, H. Y. Hwang, M. Liu, A. C. Strikwerda, A. Sternbach, J. Zhang, X. Zhao, X. Zhang, K. A. Nelson, and R. D. Averitt, "Nonlinear terahertz metamaterials via field-enhanced carrier dynamics in GaAs," *Phys. Rev. Lett.*, vol. 110, no. 21, pp. 4–5, 2013.
- [18] K. Iwaszczuk, A. Andryieuski, A. Lavrinenko, X. Zhang, and P. U. Jepsen, "Terahertz field enhancement to the MV/cm regime in a tapered parallel plate waveguide," *Opt. Express*, vol. 20, no. 8, pp. 1289–1295, 2012.
- [19] J. Zhang, X. Zhao, K. Fan, X. Wang, G. F. Zhang, K. Geng, X.

- Zhang, and R. D. Averitt, "Terahertz radiation-induced sub-cycle field electron emission across a split-gap dipole antenna," *Appl. Phys. Lett.*, vol. 107, no. 23, pp. 1–5, 2015.
- [20] C. Lange, T. Maag, M. Hohenleutner, S. Baierl, O. Schubert, E. R. J. Edwards, D. Bougeard, G. Woltersdorf, and R. Huber, "Extremely nonperturbative nonlinearities in GaAs driven by atomically strong terahertz fields in gold metamaterials," *Phys. Rev. Lett.*, vol. 113, no. 227401, pp. 1–7, 2014.
 - [21] O. Schubert, M. Hohenleutner, F. Langer, B. Urbanek, C. Lange, U. Huttner, D. Golde, T. Meier, M. Kira, S. W. Koch, and R. Huber, "Sub-cycle control of terahertz high-harmonic generation by dynamical Bloch oscillations," *Nat. Photonics*, vol. 8, no. 2, p. 2, 2014.
 - [22] K. E. Echternkamp, G. Herink, S. V. Yalunin, K. Rademann, S. Sch??fer, and C. Ropers, "Strong-field photoemission in nanotip near-fields: from quiver to sub-cycle electron dynamics," *Appl. Phys. B*, vol. 122, no. 4, pp. 1–10, 2016.
 - [23] K. Iwaszczuk, M. Zalkovskij, A. C. Strikwerda, and P. U. Jepsen, "Nitrogen plasma formation through terahertz-induced ultrafast electron field emission," *Optica*, vol. 2, no. 2, p. 2, 2015.
 - [24] A. C. Strikwerda, M. Zalkovskij, K. Iwaszczuk, D. L. Lorenzen, and P. U. Jepsen, "Permanently reconfigured metamaterials due to terahertz induced mass transfer of gold.," *Opt. Express*, vol. 23, no. 9, pp. 11586–99, 2015.
 - [25] M. Liu, H. Y. Hwang, H. Tao, A. C. Strikwerda, K. Fan, G. R. Keiser, A. J. Sternbach, K. G. West, S. Kittiwatanakul, J. Lu, S. a Wolf, F. G. Omenetto, X. Zhang, K. a Nelson, and R. D. Averitt, "Terahertz-field-induced insulator-to-metal transition in vanadium dioxide metamaterial.," *Nature*, vol. 487, no. 7407, pp. 345–8, Jul. 2012.
 - [26] H. Hirori, K. Shinokita, M. Shirai, S. Tani, Y. Kadoya, and K. Tanaka, "Extraordinary carrier multiplication gated by a picosecond electric field pulse," *Nat. Commun.*, vol. 2, no. 594, pp. 1–6, Jan. 2011.
 - [27] Y. G. Jeong, M. J. Paul, S. H. Kim, K. J. Yee, D. S. Kim, and Y. S. Lee, "Large enhancement of nonlinear terahertz absorption in intrinsic GaAs by plasmonic nano antennas," *Appl. Phys. Lett.*, vol.

103, no. 17, pp. 28–31, 2013.

- [28] K. Fan, H. Y. Hwang, M. Liu, A. C. Strikwerda, A. Sternbach, J. Zhang, X. Zhao, X. Zhang, K. A. Nelson, and R. D. Averitt, “Nonlinear Terahertz Metamaterials via Field-Enhanced Carrier Dynamics in GaAs,” *Phys. Rev. Lett.*, vol. 110, no. 217404, p. 217404, May 2013.
- [29] C. Vicario, M. Shalaby, and C. P. Hauri, “Subcycle Extreme Nonlinearities in GaP Induced by an Ultrastrong Terahertz Field,” *Phys. Rev. Lett.*, vol. 118, no. 83901, pp. 1–5, 2017.
- [30] F.-L. Yang, D.-H. Lee, H.-Y. Chen, C.-Y. Chang, S.-D. Liu, C.-C. Huang, T.-X. Chung, H.-W. Chen, C. C. Wu, and Y.-H. Liu, “5nm-gate nanowire FinFET,” *VLSI Technol. 2004 Dig. Tech. Pap. 2004 Symp.*, pp. 196–197, 2004.
- [31] S. B. Desai, S. R. Madhvapathy, A. B. Sachid, J. P. Llinas, Q. Wang, G. H. Ahn, G. Pitner, M. J. Kim, J. Bokor, C. Hu, and A. Javey, “MoS₂ transistors with 1-nanometer gate lengths,” vol. 354, no. 6308, pp. 2–6, 2016.
- [32] X. Mei, W. Yoshida, M. Lange, J. Lee, J. Zhou, P.-H. Liu, K. Leong, A. Zamora, J. Padilla, S. Sarkozy, R. Lai, and W. R. Deal, “First Demonstration of Amplification at 1 THz Using 25-nm InP High Electron Mobility Transistor Process,” *IEEE Electron Device Lett.*, vol. 36, no. 4, p. 4, 2015.
- [33] H. Tamaso, K. Sawada, K. Fujikawa, S. Harada, J. Shinkai, H. Tokuda, T. Masuda, M. Honaga, S. Itoh, and T. Tsuno, “Development of Fast-Switching SiC Transistor,” no. 66, pp. 43–49, 2008.
- [34] J. H. Zhao, V. Gruzinskis, Y. Luo, M. Weiner, M. Pan, P. Shiktorov, and E. Starikov, “Monte Carlo simulation of 4H-SiC IMPATT diodes,” *Semicond. Sci. Technol.*, vol. 15, pp. 1093–1100, 2000.
- [35] C. H. Park, B. Cheong, K. Lee, and K. J. Chang, “Structural and electronic properties of cubic, 2H, 4H and 6H SiC,” *Phys. Rev. B*, vol. 49, no. 7, 1994.
- [36] N. T. Son, O. Kordina, A. O. Konstantinov, W. M. Chen, E. Sörman, B. Monemar, and E. Janzén, “Electron effective masses and mobilities in high-purity 6H-SiC chemical vapor deposition layers,” *Appl. Phys. Lett.*, vol. 65, no. 25, pp. 3209–3211, 1994.

- [37] M. Naftaly, J. F. Molloy, B. Magnusson, Y. M. Andreev, and G. V. Lanski, "Silicon carbide—a high-transparency nonlinear material for THz applications," *Opt. Express*, vol. 24, no. 3, p. 2590, 2016.
- [38] J. Dai, J. Liu, and X. Zhang, "Terahertz Wave Air Photonics : Terahertz Wave Generation and Detection With Laser-Induced Gas Plasma," pp. 1–8, 2010.
- [39] J. Hebling, A. G. Stepanov, G. Almasi, B. Bartal, and J. Kuhl, "Tunable THz pulse generation by optical rectification of ultrashort laser pulses with tilted pulse fronts," *Appl. Phys. B Lasers Opt.*, vol. 78, no. 5, pp. 593–599, Mar. 2004.
- [40] K. Yeh, M. C. Hoffmann, and K. A. Nelson, "High-Power THz Generation , THz Nonlinear Optics ," vol. 14, no. 2, pp. 345–353, 2008.
- [41] D. H. Auston, K. P. Cheung, and P. R. Smith, "Picosecond photoconducting Hertzian dipoles," *Appl. Phys. Lett.*, vol. 45, no. 3, pp. 284–286, 1984.
- [42] X. Ropagnol, R. Morandotti, T. Ozaki, and M. Reid, "Toward high-power terahertz emitters using large aperture ZnSe photoconductive antennas," *IEEE Photonics J.*, vol. 3, no. 2, pp. 174–186, 2011.
- [43] M. Beck, H. Schäfer, G. Klatt, J. Demsar, S. Winnerl, M. Helm, and T. Dekorsy, "Impulsive terahertz radiation with high electric fields from an amplifier-driven large-area photoconductive antenna.," *Opt. Express*, vol. 18, no. 9, pp. 9251–9257, 2010.
- [44] R. J. B. Dietz, B. Globisch, H. Roehle, D. Stanze, T. Göbel, and M. Schell, "Influence and adjustment of carrier lifetimes in InGaAs/InAlAs photoconductive pulsed terahertz detectors : 6 THz bandwidth and 90dB dynamic range," *Opt. Lett.*, vol. 22, no. 16, pp. 615–623, 2014.
- [45] S. S. Dhillon, *et al.*, "The 2017 terahertz science and technology roadmap," *J. Phys. D. Appl. Phys.*, vol. 50, no. 4, p. 43001, 2017.
- [46] H. Hamster, A. Sullivan, S. Gordon, W. White, and R. W. Falcone, "Subpicosecond, electromagnetic pulses from intense laser-plasma interaction," *Phys. Rev. Lett.*, vol. 71, no. 17, pp. 2725–2728, 1993.
- [47] D. J. Cook and R. M. R. M. Hochstrasser, "Intense terahertz pulses by four-wave rectification in air," *Opt. Lett.*, vol. 25, no. 16, pp. 1210–1212, 2000.

- [48] X. Xie, J. Dai, and X. C. Zhang, "Coherent control of THz wave generation in ambient air," *Phys. Rev. Lett.*, vol. 96, no. 7, pp. 1–4, 2006.
- [49] J. Dai, X. Xie, and X. C. Zhang, "Detection of broadband terahertz waves with a laser-induced plasma in gases," *Phys. Rev. Lett.*, vol. 97, no. 10, pp. 8–11, 2006.
- [50] N. Karpowicz, J. Dai, X. Lu, Y. Chen, M. Yamaguchi, H. Zhao, X. C. Zhang, L. Zhang, C. Zhang, M. Price-Gallagher, C. Fletcher, O. Mamer, A. Lesimple, and K. Johnson, "Coherent heterodyne time-domain spectrometry covering the entire 'terahertz gap,'" *Appl. Phys. Lett.*, vol. 92, no. 1, 2008.
- [51] J. Hebling, G. Almási, I. Kozma, and J. Kuhl, "Velocity matching by pulse front tilting for large area THz-pulse generation.," *Opt. Express*, vol. 10, no. 21, pp. 1161–6, Oct. 2002.
- [52] J. a Fülöp, L. Pálfalvi, G. Almási, and J. Hebling, "Design of high-energy terahertz sources based on optical rectification.," *Opt. Express*, vol. 18, no. 12, pp. 12311–27, Jun. 2010.
- [53] B. E. A. Saleh and M. C. Teich, *Fundamentals of photonics*, vol. 24, no. 3. John Wiley & Sons, Inc., 1992.
- [54] P. U. Jepsen, C. Winnewisser, M. Schall, V. Schyja, S. R. Keiding, and M. Helm, "in Lithium Tantalate," *Phys. Rev. E*, vol. 53, no. 4, 1996.
- [55] Q. Wu, M. Litz, and X.-C. Zhang, "Broadband detection capability of ZnTe electro-optic field detectors," *Appl. Phys. Lett.*, vol. 68, no. 21, p. 2924, 1996.
- [56] Winnewisser, P. U. Jepsen, M. Schall, V. Schyja, and H. Helm, "apl_70 eo sampling znte peter.pdf," *Appl. Phys. Lett.*, vol. 70, no. 23, 1997.
- [57] Q. Wu and X.-C. Zhang, "7 terahertz broadband GaP electro-optic sensor," *Appl. Phys. Lett.*, vol. 70, no. 14, p. 1784, 1997.
- [58] P. C. M. Planken, H.-K. Nienhuys, H. J. Bakker, and T. Wenckebach, "Measurement and calculation of the orientation dependence of terahertz pulse detection in ZnTe," *J. Opt. Soc. Am. B*, vol. 18, no. 3, p. 313, 2001.
- [59] N. J. Karl, R. W. Mckinney, Y. Monnai, R. Mendis, and D. M.

- Mittleman, "Frequency-division multiplexing in the terahertz range using a leaky-wave antenna," no. September, 2015.
- [60] H.-J. Song, K. Ajito, Y. Muramoto, a. Wakatsuki, T. Nagatsuma, and N. Kukutsu, "24 Gbit/s data transmission in 300 GHz band for future terahertz communications," *Electron. Lett.*, vol. 48, no. 15, p. 953, 2012.
 - [61] T. Kleine-Ostmann and T. Nagatsuma, "A Review on Terahertz Communications Research," *J. Infrared, Millimeter, Terahertz Waves*, vol. 32, no. 2, pp. 143–171, 2011.
 - [62] S. Koenig, D. Lopez-Diaz, J. Antes, F. Boes, R. Henneberger, a. Leuther, a. Tessmann, R. Schmogrow, D. Hillerkuss, R. Palmer, T. Zwick, C. Koos, W. Freude, O. Ambacher, J. Leuthold, and I. Kallfass, "Wireless sub-THz communication system with high data rate," *Nat. Photonics*, vol. 7, no. 12, pp. 977–981, 2013.
 - [63] K. B. Crozier, a. Sundaramurthy, G. S. Kino, and C. F. Quate, "Optical antennas: Resonators for local field enhancement," *J. Appl. Phys.*, vol. 94, no. 7, p. 4632, 2003.
 - [64] C. A. Werley, K. Fan, A. C. Strikwerda, S. M. Teo, X. Zhang, R. D. Averitt, and K. A. Nelson, "Time-resolved imaging of near-fields in THz antennas and direct quantitative measurement of field enhancements.," *Opt. Express*, vol. 20, no. 8, pp. 8551–67, Apr. 2012.
 - [65] L. Razzari, A. Toma, M. Shalaby, M. Clerici, R. P. Zaccaria, C. Liberale, S. Marras, I. a. I. Al-Naib, G. Das, F. De Angelis, M. Peccianti, A. Falqui, T. Ozaki, R. Morandotti, and E. Di Fabrizio, "Extremely large extinction efficiency and field enhancement in terahertz resonant dipole nanoantennas," *Opt. Express*, vol. 19, no. 27, p. 26088, 2011.
 - [66] P. Klarskov, A. T. Tarekegne, K. Iwaszczuk, X.-C. Zhang, and P. U. Jepsen, "Amplification of resonant field enhancement by plasmonic lattice coupling in metallic slit arrays," *Sci. Rep.*, vol. 6, no. 37738, p. 37738, 2016.
 - [67] J. Dai, J. Zhang, W. Zhang, and D. Grischkowsky, "Terahertz time-domain spectroscopy characterization of the far-infrared absorption and index of refraction of high-resistivity, float-zone silicon," *J. Opt. Soc. Am. B*, vol. 21, no. 7, p. 1379, 2004.

- [68] S. A. Ku, C. M. Tu, W. Chu, C. W. Luo, K. H. Wu, A. Yabushita, C. C. Chi, and T. Kobayashi, "Saturation of the free carrier absorption in ZnTe crystals," *Opt. Express*, vol. 21, no. 12, pp. 13930–13937, 2013.
- [69] Z. Tian, C. Wang, Q. Xing, J. Gu, Y. Li, M. He, L. Chai, Q. Wang, and W. Zhang, "Quantitative analysis of Kerr nonlinearity and Kerr-like nonlinearity induced via terahertz generation in ZnTe," *Appl. Phys. Lett.*, vol. 92, no. 4, p. 41106, 2008.
- [70] I. Al-Naib, G. Sharma, M. M. Dignam, H. Hafez, A. Ibrahim, D. G. Cooke, T. Ozaki, and R. Morandotti, "Effect of local field enhancement on the nonlinear terahertz response of a silicon-based metamaterial," *Phys. Rev. B - Condens. Matter Mater. Phys.*, vol. 88, no. 19, pp. 1–8, 2013.
- [71] S. Li, G. Kumar, and T. E. Murphy, "Terahertz nonlinear conduction and absorption saturation in silicon waveguides," *Optica*, vol. 2, no. 6, p. 553, 2015.
- [72] S. M. Sze, *Semiconductor Devices: Physics and Technology*. 2006.
- [73] C. Zener, "A theory of the electrical breakdown of solid dielectrics," *Proc. Roy. Soc. A*, vol. 145, no. 855, pp. 523–529, 1934.
- [74] E. O. Kane, "Zener tunneling in semiconductors," *J. Phys. Chem. Solids*, vol. 12, no. 2, pp. 181–188, 1960.
- [75] J. R. Chelikowsky and M. L. Cohen, "Electronic structure of silicon," *Phys. Rev. B*, vol. 10, no. 12, p. 5095, 1974.
- [76] E. Cartier, M. V. Fischetti, E. a. Eklund, and F. R. McFeely, "Impact ionization in silicon," *Appl. Phys. Lett.*, vol. 62, no. 25, pp. 3339–3341, 1993.
- [77] J. Y. Tang and K. Hess, "Impact ionization of electrons in silicon (steady state)," *J. Appl. Phys.*, vol. 54, no. 9, pp. 5139–5144, 1983.
- [78] N. Sano and A. Yoshii, "Impact-ionization theory consistent with a realistic band structure of silicon," *Phys. Rev. B*, vol. 45, no. 8, p. 4171, 1992.
- [79] A. Pacelli, A. S. Spinelli, and A. L. Lacaita, "Impact ionization in silicon: A microscopic view," *J. Appl. Phys.*, vol. 83, no. 9, pp. 4760–4764, 1998.

- [80] W. N. Grant, "Electron and hole ionization rates epitaxial silicon at high electric fields," *Solid. State. Electron.*, vol. 16, no. 1, pp. 1189–1203, 1973.
- [81] R. Van Overstraeten and H. De Man, "Measurement of the ionization rates in diffused silicon p-n junctions," *Solid. State. Electron.*, vol. 13, no. 5, p. 5, 1970.
- [82] H. Wen, M. Wiczer, and A. M. Lindenberg, "Ultrafast electron cascades in semiconductors driven by intense femtosecond terahertz pulses," *Phys. Rev. B*, vol. 78, no. 125203, p. 1, 2008.
- [83] M. C. Hoffmann, J. Hebling, H. Y. Hwang, K. Lo Yeh, and K. A. Nelson, "Impact ionization in InSb probed by terahertz pump-terahertz probe spectroscopy," *Phys. Rev. B*, vol. 79, no. 16, pp. 3–6, 2009.
- [84] K. Fan, H. Y. Hwang, M. Liu, A. C. Strikwerda, A. Sternbach, J. Zhang, X. Zhao, X. Zhang, K. A. Nelson, and R. D. Averitt, "Nonlinear terahertz metamaterials via field-enhanced carrier dynamics in GaAs," *Phys. Rev. Lett.*, vol. 110, no. 217404, p. 217404, 2013.
- [85] I. C. Ho and X. C. Zhang, "Driving intervalley scattering and impact ionization in InAs with intense terahertz pulses," *Appl. Phys. Lett.*, vol. 98, no. 24, pp. 1–4, 2011.
- [86] K. Iwaszczuk, M. Salkovskij, A. C. Strikwerda, and P. U. Jepsen, "Nitrogen plasma formation through terahertz induced ultrafast electron field emission." .
- [87] K. Yoshioka, Y. Minami, K.-I. Shudo, T. D. Dao, T. Nagao, M. Kitajima, J. Takeda, and I. Katayama, "Terahertz-field-induced Nonlinear Electron Delocalization in Au Nanostructures.," *Nano Lett.*, Jan. 2015.
- [88] K. J. Willis, S. C. Hagness, and I. Knezevic, "A generalized Drude model for doped silicon at terahertz frequencies derived from microscopic transport simulation," *Appl. Phys. Lett.*, vol. 102, no. 12, p. 122113, 2013.
- [89] J. D. Jackson, *Classical electrodynamics*, Third Edit. Wiley, 1999.
- [90] C. Lange, T. Maag, M. Hohenleutner, S. Baierl, O. Schubert, E. R. J. Edwards, D. Bougeard, G. Woltersdorf, and R. Huber, "Extremely nonperturbative nonlinearities in GaAs driven by atomically strong

- terahertz fields in gold metamaterials,” *Phys. Rev. Lett.*, vol. 113, no. 22, pp. 2–7, 2014.
- [91] A. Schenk, “Rigorous theory and simplified model of the band-to-band tunneling in silicon,” *Solid. State. Electron.*, vol. 36, no. 1, p. 1, 1993.
 - [92] W. Bludau, a. Onton, and W. Heinke, “Temperature dependence of the band gap of silicon,” *J. Appl. Phys.*, vol. 45, no. 4, p. 1846, 1974.
 - [93] M. Ershov and V. Ryzhii, “Temperature dependence of the electron impact ionization coefficient in silicon,” *Semicond. Sci. Technol*, vol. 10, pp. 138–142, 1995.
 - [94] R. D. Schaller and V. I. Klimov, “High efficiency carrier multiplication in PbSe nanocrystals: Implications for solar energy conversion,” *Phys. Rev. Lett.*, vol. 92, no. 18, p. 18, 2004.
 - [95] J. J. H. Pijpers, R. Ulbricht, K. J. Tielrooij, A. Osherov, Y. Golan, C. Delerue, G. Allan, and M. Bonn, “Assessment of carrier-multiplication efficiency in bulk PbSe and PbS,” *Nat. Phys.*, vol. 5, no. 11, p. 811, 2009.
 - [96] K. Sawada, N. Matsumura, and T. Ando, “Photosensitive field emitters including a-si:h p-i-n photodetection region,” *IEEE Trans. Electron Devices*, vol. 45, no. 1, p. 321, 1998.
 - [97] R. H. Hadfield, “Single-photon detectors for optical quantum information applications,” *Nat. Photonics*, vol. 3, no. 12, p. 696, 2009.
 - [98] A. Kaiser, B. Rethfeld, M. Vicanek, and G. Simon, “Microscopic processes in dielectrics under irradiation by subpicosecond laser pulses,” *Phys. Rev. B*, vol. 61, no. 17, pp. 11437–11450, 2000.
 - [99] E. G. Gamaly, A. V. Rode, B. Luther-Davies, and V. T. Tikhonchuk, “Ablation of solids by femtosecond lasers: Ablation mechanism and ablation thresholds for metals and dielectrics,” *Phys. Plasmas*, vol. 9, no. 3, p. 949, 2002.
 - [100] M. Lenzner, J. Krüger, S. Sartania, Z. Cheng, C. Spielmann, G. Mourou, W. Kautek, and F. Krausz, “Femtosecond Optical Breakdown in Dielectrics,” *Phys. Rev. Lett.*, vol. 80, no. 18, p. 18, 1998.
 - [101] S. Ghimire, A. D. DiChiara, E. Sistrunk, P. Agostini, L. F. DiMauro,

- and D. A. Reis, “Observation of high-order harmonic generation in a bulk crystal,” *Nat. Phys.*, vol. 7, no. 2, p. 138, 2011.
- [102] B. Zaks, R. B. Liu, and M. S. Sherwin, “Experimental observation of electron–hole recollisions,” *Nature*, vol. 483, no. 7391, p. 7391, 2012.
 - [103] Y. Hu, J. Xiang, G. Liang, H. Yan, and C. M. Lieber, “Sub-100 nanometer channel length Ge/Si nanowire transistors with potential for 2 THz switching speed,” *Nano Lett.*, vol. 8, no. 3, p. 3, 2008.
 - [104] N. Kinsey, C. DeVault, J. Kim, M. Ferrera, V. M. ShalaeV, and A. Boltasseva, “Epsilon-near-zero Al-doped ZnO for ultrafast switching at telecom wavelengths,” *Optica*, vol. 2, no. 7, p. 7, 2015.
 - [105] A. G. Chynoweth, “Ionization rates for electrons and holes in silicon,” *Phys. Rev.*, vol. 109, no. 5, pp. 1537–1540, 1958.
 - [106] T. Ichibayashi, S. Tanaka, J. Kanasaki, K. Tanimura, and T. Fauster, “Ultrafast relaxation of highly excited hot electrons in Si: Roles of the L-X intervalley scattering,” *Phys. Rev. B*, vol. 84, no. 235210, p. 235210, 2011.
 - [107] J. R. Goldman and J. A. Prybyla, “Ultrafast dynamics of laser-excited electron distributions in silicon,” *Phys. Rev. Lett.*, vol. 72, no. 9, p. 1364, 1994.
 - [108] A. Sabbah and D. Riffe, “Femtosecond pump-probe reflectivity study of silicon carrier dynamics,” *Phys. Rev. B*, vol. 66, no. 165217, pp. 1–11, 2002.
 - [109] T. Tanaka, A. Harata, and T. Sawada, “Subpicosecond surface-restricted carrier and thermal dynamics by transient reflectivity measurements,” *J. Appl. Phys.*, vol. 82, no. 4033, p. 4033, 1997.
 - [110] S. Tamura, J. A. Shields, and J. P. Wolfe, “Lattice Dynamics and elastic phonon scattering,” *Phys. Rev. B*, vol. 44, no. 7, p. 7, 1991.
 - [111] F. Meng, M. D. Thomson, B. E. Sernelius, M. Jorger, and H. G. Roskos, “Ultrafast dynamic conductivity and scattering rate saturation of photoexcited charge carriers in silicon investigated with a midinfrared continuum probe,” *Phys. Rev. B*, vol. 91, no. 75201, p. 75201, 2015.
 - [112] R. A. Soref and B. R. Bennett, “Electrooptical effects in silicon,” *IEEE J. Quantum Electron.*, vol. 23, no. 1, p. 1, 1987.

- [113] N. Sano, T. Aoki, M. Tomizawa, and A. Yoshii, "Electron transport and impact ionization in silicon," *Phys. Rev. B*, vol. 41, no. 17, p. 12123, 1990.
- [114] M. C. Downer and C. V. Shank, "Ultrafast heating of silicon on sapphire by femtosecond optical pulses," *Phys. Rev. Lett.*, vol. 56, no. 7, p. 7, 1986.
- [115] Y. Okuto and C. R. Crowell, "Energy-conservation considerations in the characterization of impact ionization in semiconductors," *Phys. Rev. B*, vol. 6, no. 8, pp. 3076–3081, 1972.
- [116] D. B. Laks, G. F. Neumark, and S. T. Pantelides, "Accurate interband-Auger-recombination rates in silicon," *Phys. Rev. B*, vol. 42, no. 8, p. 8, 1990.
- [117] P. Yu and M. Cardona, *Fundamentals of semiconductors*. 2010.
- [118] a J. L. Adam, J. M. Brok, M. a Seo, K. J. Ahn, D. S. Kim, J. H. Kang, Q. H. Park, M. Nagel, and P. C. M. Planken, "Advanced terahertz electric near-field measurements at sub-wavelength diameter metallic apertures.," *Opt. Express*, vol. 16, no. 10, pp. 7407–7417, 2008.
- [119] K. B. Crozier, a. Sundaramurthy, G. S. Kino, and C. F. Quate, "Optical antennas: Resonators for local field enhancement," *J. Appl. Phys.*, vol. 94, no. 7, pp. 4632–4642, 2003.
- [120] E. O. Kane, "Electron scattering by pair production in silicon," *Phys. Rev.*, vol. 159, pp. 624–631, 1967.
- [121] W. Maes, K. De Meyer, and R. Van Overstraeten, "Impact ionization in silicon: a review and update," *Solid. State. Electron.*, vol. 33, no. 6, pp. 705–718, Jun. 1990.
- [122] A. C. Turner-Foster, M. a Foster, J. S. Levy, C. B. Poitras, R. Salem, A. L. Gaeta, and M. Lipson, "Ultrashort free-carrier lifetime in low-loss silicon nanowaveguides.," *Opt. Express*, vol. 18, no. 4, pp. 3582–3591, 2010.
- [123] F. E. Doany, D. Grischkowsky, and C. C. Chi, "Carrier lifetime versus ion-implantation dose in silicon on sapphire," *Appl. Phys. Lett.*, vol. 50, no. 8, pp. 460–462, 1987.
- [124] H. J. Round, "A note on carborundum," *Electr. World*, vol. 19, no. 309, 1907.

- [125] O. V. Losev, *Telegr. ya i Telef. bez Provodov*, vol. 44, no. 485, 1927.
- [126] J. B. Casady and R. W. Johnson, "Status of silicon carbide (SiC) as a wide-bandgap semiconductor for high-temperature applications: A review," *Solid. State. Electron.*, vol. 39, no. 10, pp. 1409–1422, 1996.
- [127] M. R. Werner and W. R. Fahrner, "Review on materials, microsensors, systems, and devices for high-temperature and harsh-environment applications," *IEEE Trans. Ind. Electron.*, vol. 48, no. 2, pp. 249–257, 2001.
- [128] M. B. . Wijesundara and R. G. Azevedo, *Series Editors : Senturia, Stephen D. Howe, Roger T. Ricco, Antonio J.*, vol. 2. London: Springer, 2011.
- [129] A. A. Lebedev, "Deep level centers in silicon carbide: A review," *Semiconductors*, vol. 33, no. 2, pp. 107–130, 1999.
- [130] J. Fan and P. K. Chu, *Silicon Carbide Nanostructures Fabrication, Structure, and Properties*. Springer, 2014.
- [131] Y. Ou, V. Jokubavicius, S. Kamiyama, C. Liu, R. W. Berg, M. Linnarsson, R. Yakimova, and M. Syv, "Donor-acceptor-pair emission characterization in N-B doped fluorescent SiC Abstract," *Opt. Mater. (Amst)*., vol. 1, no. 8, pp. 1439–1446, 2011.
- [132] S. Kamiyama, T. Maeda, Y. Nakamura, M. Iwaya, H. Amano, I. Akasaki, H. Kinoshita, T. Furusho, M. Yoshimoto, T. Kimoto, J. Suda, A. Henry, I. G. Ivanov, J. P. Bergman, B. Monemar, T. Onuma, and S. F. Chichibu, "Extremely high quantum efficiency of donor-acceptor-pair emission in N-and-B-doped 6H-SiC," *J. Appl. Phys.*, vol. 99, no. 9, 2006.
- [133] A. T. Tarekegne, K. Iwaszczuk, M. Zalkovskij, A. C. Strikwerda, and P. U. Jepsen, "Impact ionization in high resistivity silicon induced by an intense terahertz field enhanced by an antenna array," *New J. Phys.*, vol. 17, no. 43002, p. 1, 2015.
- [134] N. T. Son, W. M. Chen, O. Kordina, A. O. Konstantinov, B. Monemar, E. Janzen, D. M. Hofman, D. Volm, M. Drechsler, and B. K. Meyer, "Electron effective masses in 4H SiC," *Appl. Phys. Lett.*, vol. 66, no. 9, pp. 1074–1076, 1995.
- [135] J. D. Caldwell, L. Lindsay, V. Giannini, I. Vurgaftman, T. L. Reinecke, S. A. Maier, and O. J. Glembocki, "Low-loss, infrared and terahertz nanophotonics using surface phonon polaritons,"

Nanophotonics, vol. 4, no. 1, pp. 44–68, 2015.

- [136] R. Hillenbrand, T. Taubner, and F. Keilmann, “Phonon-enhanced light matter interaction at the nanometre scale,” *Nature*, vol. 418, no. 6894, pp. 159–162, 2002.
- [137] T. Tiwald, J. Woollam, S. Zollner, J. Christiansen, R. Gregory, T. Wetteroth, S. Wilson, and A. Powell, “Carrier concentration and lattice absorption in bulk and epitaxial silicon carbide determined using infrared ellipsometry,” *Phys. Rev. B*, vol. 60, no. 16, pp. 11464–11474, 1999.
- [138] S. Nakashima, H. Katahama, Y. Nakakura, and A. Mitsuishi, “Relative Raman intensities of the folded modes in SiC polytypes,” *Phys. Rev. B*, vol. 33, no. 8, pp. 5721–5729, 1986.
- [139] H. Okumura, E. Sakuma, J. H. Lee, H. Mukaida, S. Misawa, K. Endo, and S. Yoshida, “Raman scattering of SiC: Application to the identification of heteroepitaxy of SiC polytypes,” *J. Appl. Phys.*, vol. 61, no. 3, pp. 1134–1136, 1987.
- [140] D. W. Feldman, J. H. Parker, W. J. Choyke, and L. Patrick, “Raman Scattering in 6H SiC,” *Phys. Rev.*, vol. 170, no. 3, pp. 698–704, 1968.
- [141] D. W. Feldman, J. H. Parker, W. J. Choyke, and L. Patrick, “Phonon Dispersion Curves by Raman Scattering in SiC, Polytypes 3C, 4H, 6H, and 21R,” *Phys. Rev.*, vol. 173, no. 3, pp. 787–793, 1968.
- [142] T. Tomita, S. Saito, M. Baba, M. Hundhausen, T. Suemoto, and S. Nakashima, “Selective resonance effect of the folded longitudinal phonon modes in the Raman spectra of SiC,” *Phys. Rev. B - Condens. Matter Mater. Phys.*, vol. 62, no. 19, pp. 12896–12901, 2000.
- [143] S. Nakashima and H. Harima, “Raman Investigation of SiC Polytypes,” *Phys. Status Solidi A*, vol. 162, pp. 39–64, 1997.
- [144] K.-Y. Kim, J. H. Glowina, A. J. Taylor, and G. Rodriguez, “Terahertz emission from ultrafast ionizing air in symmetry-broken laser fields,” *Opt. Express*, vol. 15, no. 8, p. 4577, 2007.
- [145] W. Götz, A. Schöner, G. Pensl, W. Suttrop, W. J. Choyke, R. Stein, and S. Leibenzeder, “Nitrogen donors in 4H-silicon carbide,” *J. Appl. Phys.*, vol. 73, no. 7, pp. 3332–3338, 1993.
- [146] W. Suttrop, G. Pensl, W. J. Choyke, R. Stein, S. Leibenzeder, and W.- Erlangen, “Hall effect and infrared absorption measurements on

- nitrogen donors in 6H silicon carbide Hall effect and infrared in 6H-silicon carbide,” vol. 3708, no. 1992, pp. 129–135, 2011.
- [147] S. J. Clark, M. D. Segall, C. J. Pickard, P. J. Hasnip, M. I. J. Probert, K. Refson, and M. C. Payne, “First principles methods using CASTEP,” *Zeitschrift für Krist.*, vol. 220, no. 5-6-2005, pp. 567–570, 2005.
 - [148] L. Patrick, D. R. Hamilton, and W. J. Choyke, “Optical properties of Cubic SiC: Luminescence of nitrogen-exciton complexes, and interband absorption,” *Phys. Rev.*, vol. 132, no. 5, pp. 2023–2031, 1963.
 - [149] G. L. Zhao and D. Bagayoko, “Electronic structure and charge transfer in 3C- and 4H-SiC,” *New J. Phys.*, vol. 16, 2000.
 - [150] P. Kaeckell, B. Wenzien, and F. Bechstedt, “Electronic properties of cubic and hexagonal SiC polytypes from ab initio calculations,” *Phys. Rev. B*, vol. 50, no. 15, pp. 10761–10768, 1994.
 - [151] B. Wenzien, P. Kackell, and F. Bechstedt, “Quasiparticle band structure of silicon carbide polytypes,” *Phys. Rev. B*, vol. 52, no. 15, pp. 10897–10905, 1995.
 - [152] B. Kaczer, H.-J. Im, J. Pelz, J. Chen, and W. Choyke, “Direct observation of conduction-band structure of 4H- and 6H-SiC using ballistic electron emission microscopy,” *Phys. Rev. B*, vol. 57, no. 7, pp. 4027–4032, 1998.
 - [153] C. Persson and U. Lindefelt, “Relativistic band structure calculation of cubic and hexagonal SiC polytypes,” *J. Appl. Phys.*, vol. 82, no. 11, pp. 5496–5508, 1997.
 - [154] G. Pennington and N. Goldsman, “Self-consistent calculations for n-type hexagonal SiC inversion layers,” *J. Appl. Phys.*, vol. 95, no. 8, pp. 4223–4234, 2004.
 - [155] G. Dresselhaus, A. F. Kip, and C. Kittel, “Cyclotron resonance of electrons and holes in silicon and germanium crystals,” *Phys. Rev.*, vol. 98, no. 2, pp. 368–384, 1955.
 - [156] D. Volm, B. K. Meyer, D. M. Hofmann, W. M. Chen, N. T. Son, C. Persson, U. Lindefelt, O. Kordina, E. Sorman, A. O. Konstantinov, B. Monemar, and E. Janzen, “Determination of the electron effective-mass tensor in 4H SiC,” *Phys. Rev. B*, vol. 53, no. 23, pp. 15409–15412, 1996.

- [157] T. Troffer, M. Schadt, T. Frank, H. Itoh, G. Pensl, J. Heindl, H. P. Strunk, and M. Maier, "Doping of SiC by Implantation of Boron and Aluminum," *Phys. Status Solidi*, vol. 162, no. 1, pp. 277–298, 1997.
- [158] J. Pernot, S. Contreras, and J. Camassel, "Electrical transport properties of aluminum-implanted 4H-SiC," *J. Appl. Phys.*, vol. 98, no. 2, 2005.
- [159] M. Ikeda, H. Matsunami, and T. Tanaka, "Site effect on the impurity levels in 4H, 6H, and 15R SiC," *Phys. Rev. B*, vol. 22, no. 6, pp. 2842–2854, 1980.
- [160] N. I. Kuznetsov and A. S. Zubrilov, "Deep centers and electroluminescence in 4H-SiC diodes with a p-type base region," *Mater. Sci. Eng. B*, vol. 29, no. 1–3, pp. 181–184, 1995.
- [161] J. W. Sun, S. Kamiyama, V. Jokubavicius, H. Peyre, R. Yakimova, S. Juillaguet, and M. Syväjärvi, "Fluorescent silicon carbide as an ultraviolet-to-visible light converter by control of donor to acceptor recombinations," *J. Phys. D: Appl. Phys.*, vol. 45, p. 235107, 2012.
- [162] X. Liu, S.-Y. Zhuo, P. Gao, W. Huang, C.-F. Yan, and E.-W. Shi, "Donor-acceptor-pair emission in fluorescent 4H-SiC grown by PVT method," *AIP Adv.*, vol. 5, no. 4, p. 47133, 2015.
- [163] N. Smith, "Classical generalization of the Drude formula for the optical conductivity," *Phys. Rev. B*, vol. 64, no. 15, pp. 1–6, 2001.
- [164] J. Pernot, W. Zawadzki, S. Contreras, J. L. Robert, E. Neyret, and L. Di Cioccio, "Electrical transport in n-type 4H silicon carbide," *J. Appl. Phys.*, vol. 90, no. 4, pp. 1869–1878, 2001.
- [165] J. R. Jenny, M. Skowronski, W. C. Mitchel, H. M. Hobgood, R. C. Glass, G. Augustine, and R. H. Hopkins, "On the compensation mechanism in high-resistivity 6H-SiC doped with vanadium," *J. Appl. Phys.*, vol. 78, no. 6, pp. 3839–3842, 1995.
- [166] G. Liaugaudas, P. Ščajev, and K. Jarašiūnas, "Carrier dynamics and photoelectrical parameters in highly compensated sublimation grown 3C-SiC layers studied by time-resolved nonlinear optical techniques," *Semicond. Sci. Technol.*, vol. 29, no. 1, p. 15004, 2014.
- [167] W. C. Mitchel, W. D. Mitchell, H. E. Smith, G. Landis, S. R. Smith, and E. R. Glaser, "Compensation mechanism in high purity semi-insulating 4H-SiC," *J. Appl. Phys.*, vol. 101, no. 5, pp. 1–7, 2007.

- [168] Y. Mukai, H. Hirori, and K. Tanaka, “Electric field ionization of gallium acceptors in germanium induced by single-cycle terahertz pulses,” *Phys. Rev. B - Condens. Matter Mater. Phys.*, vol. 87, no. 20, pp. 1–16, 2013.
- [169] H. Q. Nie and D. D. Coon, “Tunneling of holes from acceptor levels in an applied field,” *Solid State Electron.*, vol. 27, no. 1, pp. 53–58, 1984.
- [170] A. Dargys and S. Zurauskas, “Tunnel ionization of shallow acceptors and donors in GaAs,” *J. Phys. Condens. Matter*, vol. 7, no. 10, pp. 2133–2146, 1995.
- [171] G. Sharma, I. Al-Naib, H. Hafez, R. Morandotti, D. G. Cooke, and T. Ozaki, “Carrier density dependence of the nonlinear absorption of intense THz radiation in GaAs,” *Opt. Express*, vol. 20, no. 16, p. 18016, 2012.
- [172] T. Terashige, H. Yada, Y. Matsui, T. Miyamoto, N. Kida, and H. Okamoto, “Temperature and carrier-density dependence of electron-hole scattering in silicon investigated by optical-pump terahertz-probe spectroscopy,” *Phys. Rev. B*, vol. 91, no. 24, pp. 1–5, 2015.